UNIVERSITY OF LIVERPOOL

School of Engineering

PhD Thesis

Advanced laser beam shaping using spatial light modulators for material surface processing

Thesis submitted in accordance with the requirements of

University of Liverpool for the degree of Doctor of Philosophy

By

Jiangning Li

January 2018

School of Engineering

The University of Liverpool

Brownlow hill

L69 3GH

UK

Declaration

I hereby declare that all of work contained within this dissertation has not been submitted for any other qualification.

Signed:

Date:

Abstract

Beam shaping is the process of redistributing the irradiance and phase of a beam of optical radiation. The beam shape is defined by the irradiance distribution. In recent years, laser beam shaping has been employed in many fields of scientific, engineering and industrial R&D for many applications, such as material processing, medical applications, lithography, optical data storage and laboratory research.

In this thesis, a novel beam shaping technique is presented. Different from geometrical optics and diffractive methods, an imaging-based beam shaping system was built and tested. A laser beam was shaped using geometric masks applied on a spatial light modulator (SLM) at objective plane of a lens system and reconstructed at imaging plane. Geometric masks generated based on real beam profile can modulate both the outline profile and intensity distribution of the input laser. Laser parallel processing technique was also employed in this research to increase the beam shaping efficiency.

The results obtained in this thesis demonstrate high accuracy and flexibility of this beam shaping technique, showing many potential applications.

List of Publication to Date by Author

Peer-Reviewed Journal Publication

1. **Li, J**., Kuang, Z., Edwardson, S., Perrie, W., Liu, D., & Dearden, G. (2016). Imaging-based amplitude laser beam shaping for material processing by 2D reflectivity tuning of a spatial light modulator. Applied Optics, 55(5), 1095-1100.

2. Kuang, Z., **Li, J**., Edwardson. S., W., Perrie, W., Liu, D., & Dearden, G. (2015). Ultrafast laser beam shaping for material processing at imaging plane by geometric masks using a spatial light modulator. Optics and Lasers in Engineering, 70, 1-5.

Conference Publications

1. **Li. J**., Kuang, Z., Vilar. G.J., Dearden. G., Perrie, W., & Edwardson, S. (2016) Dynamic ultrafast laser beam shaping for material processing at the imaging plane using a spatial light modulator. 9th International Conference on Photonic Technologies – LANE 2016

Acknowledgment

First of all, I hereby sincerely acknowledge my supervisors, Dr. Stuart Edwardson and Prof. Geoff Dearden, who always give me encouragement, help and advice during ups and downs of my research. I would like to thank Dr. Zheng Kuang, for his kindly guidance for experimental skills and optics knowledge. I would also like to thank Dr. Walter Perrie for his advice in the last year of my PhD. Without their dedication, this work would not have been possible.

I am very grateful to everyone from the Laser Group of the University of Liverpool who helped in my research, in particular, Mr. Andy Snaylam and Dr. Eamonn Fearon. I also appreciate the help from my fellow student Yue Tang and the friendship from all my fellow students: Hui Gao, Guangyu Zhu, Tong Zhou, Jing Liu and Qiangliang Li.

Last but not least, I would like to thank my parents. They have been supporting me unconditionally throughout my study in UK and shown me the right way to go when I lost direction.

Contents

List of figures

List of table

List of symbols

Symbol	Unit	Description
A	V/m	Amplitude of electric field
D	W/(m^2·K)	Heat diffusion coefficient
E	V/m	Electric field
H	n/a	Transfer function in frequency spectrum
I	W	Laser power intensity
J	n/a	Jones matrix
M	n/a	Magnification factor
P	n/a	Pupil function of a lens
R	n/a	Reflectivity
U	n/a	Complex amplitude
$\mathcal{F}$	n/a	Fourier transform
GL	n/a	Gray level
f	mm	Focal length
k	n/a	Wave vector
n	n/a	Refraction index
t	n/a	Transmittance function of a CGH
u	mm	Objective distance
θ	degree	Phase of a laser beam
v	mm	Imaging distance
d_f	mm	Beam diameter at focal plane
φ	degree	Phase of a laser beam
Δv	nm	Spectrum bandwidth
η	n/a	Shaping efficiency
τ_p	ns	Pulse duration

List of abbreviations

AOM	Acousto-Optic Modulator
AP	Azimuthal Polarization
CCD	Charge-Coupled Device
CGH	Computer Generated Hologram
CPA	Chirped Pulse Amplification
DVI	Digital Visual Interface
GAA	Generalised Adaptive Additive
GL	Gratings and Lenses
GS	Gerchberg-Saxton
GSW	Weighted Gerchberg-Saxton
LC	Liquid Crystal
LCOS	Liquid-Crystal on Silicon
LIPSS	Laser Induced Periodic Surface Structures
MPFL	Multiplexed Phase Fresnel Lenses
MRAF	Mixed-Region Amplitude Freedom
ND	Neutral Density
OAM	Oribital Angular Momentum
ORA	Optimal Rotation Angle
RP	Radial Polarization
SESAM	Semiconductor Saturable Absorber Mirror
XGA	Extended graphic array

Chapter 1 Introduction

1.1 Background and motivation

A laser is a device that emits light through a process of optical modification based on the stimulated emission of electromagnetic radiation. The theoretical foundation of laser was established by Albert Einstein in 1917 [1]. The first functioning laser was operated by Theodore H. Maiman at Hughes Research Laboratories, California in 1960 [2]. After that, laser techniques have been widely used in many scientific, engineering and industrial fields [3] [4]. During the last decade, ultrashort pulse laser has been employed for high precision surface micro-structuring of materials such as metals, semi-conductors and dielectrics, due to the ultra-high intensity of focused pulses, well defined ablation threshold and little thermal damage to materials.

This work is primarily concerned with laser beam shaping for the improvement of flexibility and accuracy. Beam shaping is the process of redistributing the irradiance and phase of a beam of optical radiation [3]. The beam shape is defined by the irradiance distribution. The phase and intensity are two major factors in determining the properties of beam profile. Both coherent and incoherent beams can be shaped into required distributions. In recent years, laser beam shaping has been employed in many fields of scientific, engineering and industrial R&D for many applications, such as materials processing, medical applications [4], lithography [5], optical data storage [6] and laboratory research [7]. This is due to the unique properties of ultra-high

intensity, monochromatic coherent of radiation.

Early theoretical research about beam shaping was published by Frieden [8] and Kreuzer [9] during the 1960s. They pointed out that a by using two plano-aspheric lenses or a pair of selectively aberrated lens, a plane wave with uniform irradiance can be obtained from a TEM(0,0) which is a perfect Gaussian structure. Although the research about beam shaping started just after the first laser was invented in 1960, there are only a few papers that appeared before 1980. The publications about beam shaping have increased significantly since 1995. So far, there have been thousands of papers about beam shaping using all methods.

Among all the kinds of shapes and irradiance distributions, there has been more interest in a uniform irradiance with steep sides or flat-top beam because of the uniform intensity distribution over the illuminated area. Flat-top beams also have applications in laser printing and thin film processing.

However, non-conventional beam shapes have the advantage that they can be explicitly designed to meet the requirement of a given material configuration or application that could not be feasible with either Gaussian or flat-top beam. For instance, a focused laser beam with minimized side lobes to eliminate cross talk was used in laser disk technology [3].

Different techniques have been attempted to shape laser beams in many applications [10, 11, 12]. Various laser beam splitting gratings have been developed based on Fourier transform. An arbitrary periodic grating can split an incoming beam into a large number of outgoing beam to increase the efficiency and throughput of laser processing. For some applications, it is desirable to put separate energy into certain spots, while keeping the energy in all of these spots at a certain amount. In recent years, due to the development of spatial light modulator (SLM) technology and improvement in algorithms, it has become much easier to generate all kinds of holograms automatically. Spatial light modulator is a powerful device based on liquid-crystal technology for modulation of both phase and polarization of an incident laser beam. However, this method still has limitations in intensity distribution control and shaping design when splitting a laser beam. Although the generation of hologram has become much faster and more user friendly, it still needs complex calculations using specially designed program that are not sufficiently flexible to reach industrial requirements.

Another method to shape a laser beam is using geometrical optics to solve the optical design of components required to shape the irradiance and phase of a beam. In the last decades, laser beam have been shaped using many geometrical optics such as an aperture, apodization, or integrator optical components [13]. For instance, a Powell lens can generate a straight, uniform laser line by fanning out a collimated beam in

one dimension and a Fresnel lens can be used to eliminate the zero order in parallel processing. Although numerous geometrical optics are designed for laser beam shaping in both shape and phase for many applications, their flexibility is not sufficient for some complex requirements, since one device is normally designed just for one application.

These two beam shaping techniques above enhance laser processing efficiency but have disadvantages in accuracy and flexibility. Therefore, a more flexible and accurate method for beam shaping is ideal for a research study. In this research, a novel beam shaping method for both outline and intensity distribution is demonstrated and analyzed, the beam shaping accuracy and flexibility have been taken to a new level.

1.2 Aim and Objectives

The aim of this work is to highlight the capabilities of novel outline and intensity distribution laser beam shaping using a spatial light modulator (SLM) and processing at the imaging plane. The main objectives of this thesis are:

- To investigate the capabilities of beam shaping at the objective plane and processing at the image plane using a Liquid crystal on silicon (LCOS) SLM.
- To demonstrate beam outline shaping using a binary mask technique applied on a SLM.

- To demonstrate beam intensity distribution shaping using a gray level mask applied on a SLM.

- To demonstrate parallel processing with shaped laser beams and multiple SLMs.

- To identify the optimized processing parameters for shaped beams and parallel processing in various applications.

Presented in this thesis is a novel method of beam shaping and material processing at the imaging plane using geometric masks applied on a SLM and a long beam path setup.

1.3 Overview of this thesis

Chapter 2 provides an overview of relevant background information on ultrafast laser micro-processing and polarization and wavefront control of laser beams. Also included is a literature review on laser beam shaping and ultrafast laser surface processing and their applications.

Chapter 3 provides a description of the experimental equipment, setup and methodology used to implement and analyze the experiments described in this thesis.

Chapter 4 presents the difference between processing at focal plane and imaging plan. This chapter includes an original ultrafast laser beam shaping technique for material processing using a spatial light modulator. Complex and time-consuming diffraction

far-field phase hologram based on Fourier transformation are avoided, while simple and direct geometric masks are used to shape the incident beam at diffraction near-field.

Chapter 5 presents the method to modulate the intensity distribution of a shaped laser beam. In chapter 4, various beam shapes were obtained and reconstructed at imaging plane. However, the binary mask can only change the outline of a laser beam, the intensity distribution was still consistent with the original Gaussian distribution. In this chapter, gray level masks will be generated based on the original beam profile and applied on SLM.

Chapter 6 presents an imaging based beam shaping combined with parallel processing. As in chapter 5, binary and intensity masks will be applied on a SLM to shape the input laser beam in both outline profile and intensity distribution. A second SLM with computer generated hologram (CGH) will be used to split the beam.

Chapter 7 summarizes the results achieved in this research project and maps out potential future industrial applications and provides suggestion for future work.

Chapter 2 Literature Review

2.1 Introduction to lasers and ultrafast laser technology

2.1.1 Introduction to lasers

"Laser" is an acronym for light amplification by stimulated emission of radiation. A laser is a device can emit amplified light by stimulated emission of electromagnetic radiation. An active medium must be contained in a laser which can be solid, liquid, gas or plasma. In the laser generating process, the medium is excited by a pumping source to the amplifying state. Flash lamps, lasers, electrons chemical reactions, ion beams and X-ray sources are commonly used to be the pumping sources [14]. In the amplifying state, some electrons can be generated to a higher energy state. There is a unique energy level for each orbit in an atom. When an electron transit to a lower level, a photon with the frequency ofv_{12} will be generated, in which $E1$ is the grounded level, $E2$ is the excited level, the energy of an incident photon is $hv_{12}= |E1 - E2|$ and h is Planck's constant. Figure2.1 shows the stimulated emission process.

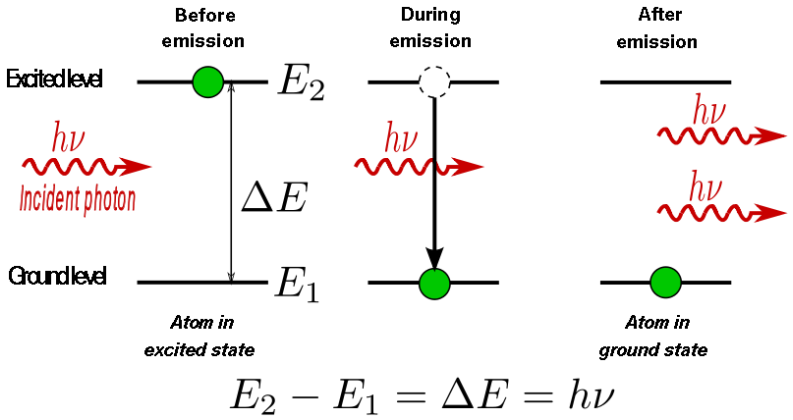

Figure 2.1 Stimulated Emission principle [15]

An atom on the ground level absorbs the emission energy and converts to the excited level, which leads to a series of stimulated emission. The atom gives up the excess energy as a photon, *hv*, and converts to a lower level. The generated photon has the same phase, same frequency, same state of polarization and same propagates in the same direction as the previous photon.

Two mirrors are set parallel to each other to form an optical oscillator. The light generated by the active medium is adjusted to be parallel to its axis and be reflected back and forth by the resonator. When the amount of gained light equals the losses in each pass, the combination of the amplifier and the resonator will be at the threshold for lasing. One of the two mirrors is partially transparent to allow the operating beam to come out of the chamber. The other mirror is totally reflecting, which can be achieved to be 99.999%. This mirror is usually designed to be curved to minimize the losses of oscillating power and make it easy to align both mirrors without undue difficulty.

2.1.2 Introduction to Ultrafast lasers

Ultrafast laser refers to a laser that generates light pulses with temporal duration shorter than a few tens of picoseconds ($1ps=10^{-12}s$). In order to produce such short and intensive pulses, special technology such as modelocking and chirped pulse amplification (CPA) are required [16].

2.1.3 Mode locking

Mode locking is a technique in optics to obtain ultrashort laser pulses on the order of picoseconds (10^{-12}s) or femtoseconds (10^{-15}s). This was first proposed by Lamb [17]and observed experimentally by Hargrove et al [18]. In the steady state, the pulse parameter keeps unchanged after each completed round trip due to the accumulation of each standing wave. Each time the pulses hit the output of the oscillator, a usable pulse with a short pulse duration (typically between 30fs and 30ps) is emitted and the pulse repetition period correspond to the length of the resonator (typically several nanoseconds), so that the peak power of a mode-locked laser can be orders of magnitude higher than the average power.

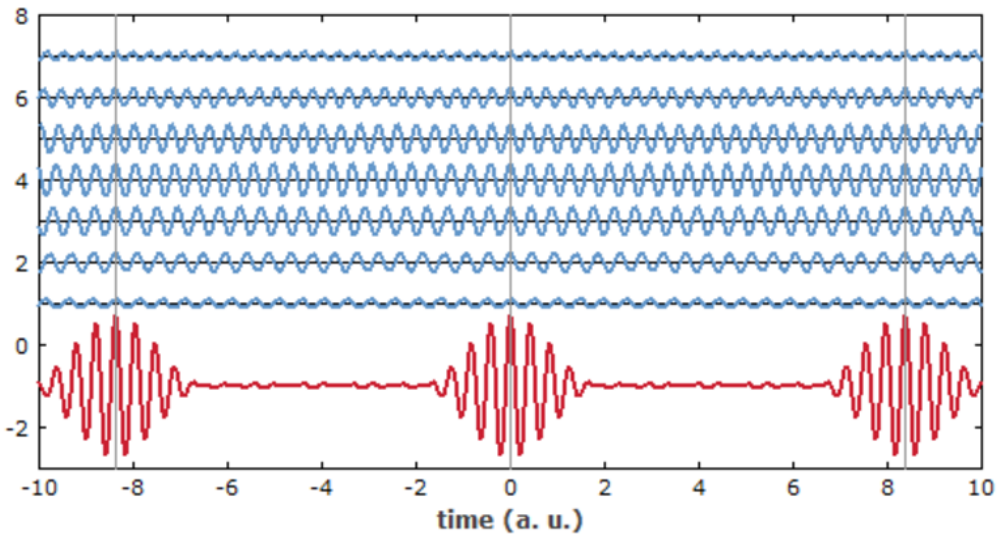

Figure 2.2 Synthesis of a periodic pulse train (red curve) by adding seven oscillation with slight different frequencies (blue curves). The vertical lines indicating points in time where all oscillation add up in phase [19].

As shown in Figure 2.2, there is a wide spectrum bandwidth for each laser beam, causing a series of oscillation frequencies or longitudinal modes. By inducing a fix phase relationship between the longitudinal modes, an amplified mode can be obtained. The relationship between the spectrum bandwidth Δv and the generated output pulse of duration τ_p can be expressed as: $\tau_p \cdot \Delta v = constant$ [20, 21]. For example, a titanium-doped sapphire has a lasing spectrum range of approximately 300nm centered near 800nm, i.e. a gain of bandwidth Δv of 130THz, and hence can support a temporal pulse-length $\tau_p = \frac{1}{\Delta v} = 8\text{fs}$.

Mode locking methods are classified as active and passive mode locking [22]. Active mode locking uses an intracavity dynamic optical modulator, typically an acousto-optic or a semiconductor electro absorption modulator. Ultrashort pulses can be generated if the modulation is synchronized with the resonator round trips. The light bouncing between the mirrors of cavity is either attenuated when the device is “off” or transmitted through when it is “on”. The modulator is “switched on” periodically each time the pulse has completed a cavity round trip.

On the other hand, passive mode locking uses nonlinear materials, such as a saturable absorber or artificial saturable absorber (Kerr lens) inside the resonator. Passive mode locking does not need an external signal since a saturable resonator is employed to modulate the losses by the cavity itself. A common saturable absorber is a

semiconductor saturable absorber mirror (SESAM) which has a lower reflectivity for low intensity and higher reflectivity for ultrashort high intensity pulse. Compared with active mode locking, passive mode locking typically generates shorter pulses [22].

2.1.4 Chirped Pulse Amplification (CPA)

Chirped pulse amplification (CPA) is a technique to amplify an ultrashort laser pulse to high intensities while avoiding excessive nonlinear pulse distortions or optical damage [23].

With mode locking techniques, ultrashort pulse laser oscillator can operate at a high pulse repetition rate (typically>30MHz) and generate low pulse energy typically in nanojoule (nJ) level. However, for many applications such as mirco-machining, this energy level is insufficient and needs to be amplified. Direct amplification of ultrashort pulses would lead to nonlinear effects at ultrahigh peak intensity and damage the optical components inside the amplifier. Thus, CPA is required for amplification [24].

As shown in Figure 2.3, a broad-bandwidth seed pulse is generated and then reaches a pulse stretcher between the oscillator and amplifier, increasing the pulse duration by a factor of ten thousand or more, passes through amplifiers where it grow in energy by 10^{12} and compress it back into a short pulse of extremely high intensity [25].

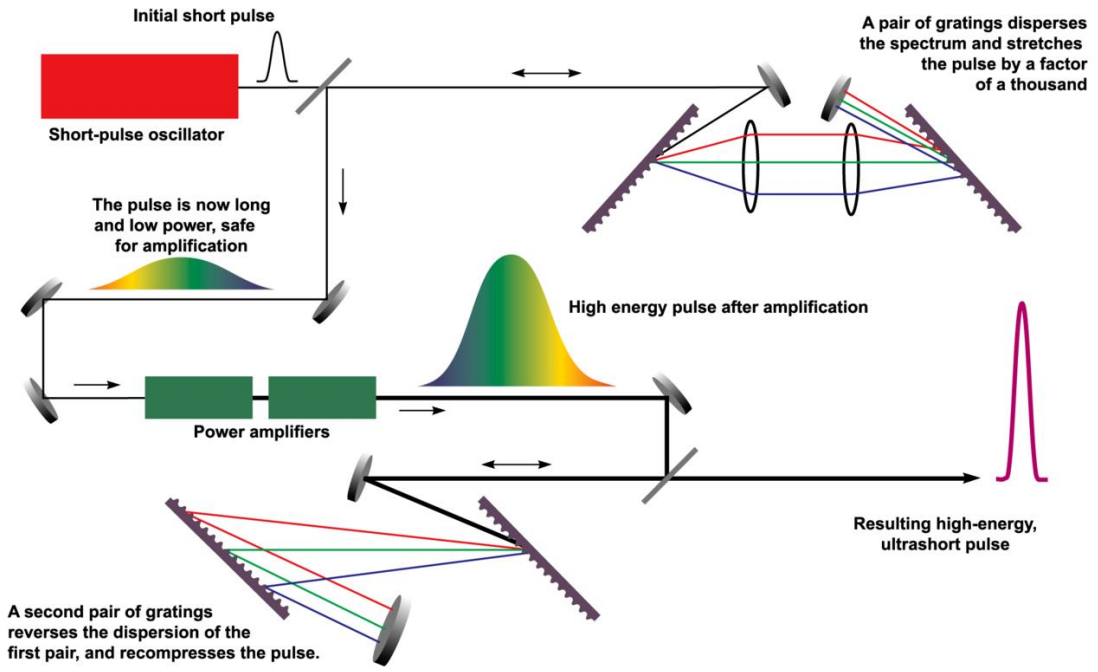

Figure 2.3 Diagrammatic scheme of chirped pulse amplification [25]

The pulse stretcher and compressor are normally made of a pair of optical gratings [26]. Figure 2.4 (a) demonstrates one implementation of the grating stretcher [25, 27]. The dispersive properties of the gratings are exploited to change the pulse duration of an ultrashort pulse having broad frequency spectral bandwidth, Δv, and the pulse is stretched while travelling between the pair of optical gratings. Different frequency components in the pulse are dispersed into different directions each time reflected on the gratings; hence they have different optical path lengths. Consequently, the frequency component that has a shorter optical path length will come out earlier than the frequency component that travels a longer path, hence the pulse is stretched. The amount of stretching is determined by the distance, $L_s = 4f - L_g^s$, where L_g^s is the

separation of the stretcher grating-pair.

Figure 2.4(b) demonstrate the compressor, which is also made of a pair of grating, but the dispersion is arranged in the opposite way as the stretcher. The amount of compression is simply determined by the separation of the grating-pair, $L_c = L_g^c$. To obtain the shortest compressed pulse, the compressor and the stretcher must match so that $L_c = L_s$. Pulse duration other than the shortest can be easily obtained by simply misaligning the compressor to the stretcher by varying the grating separation.

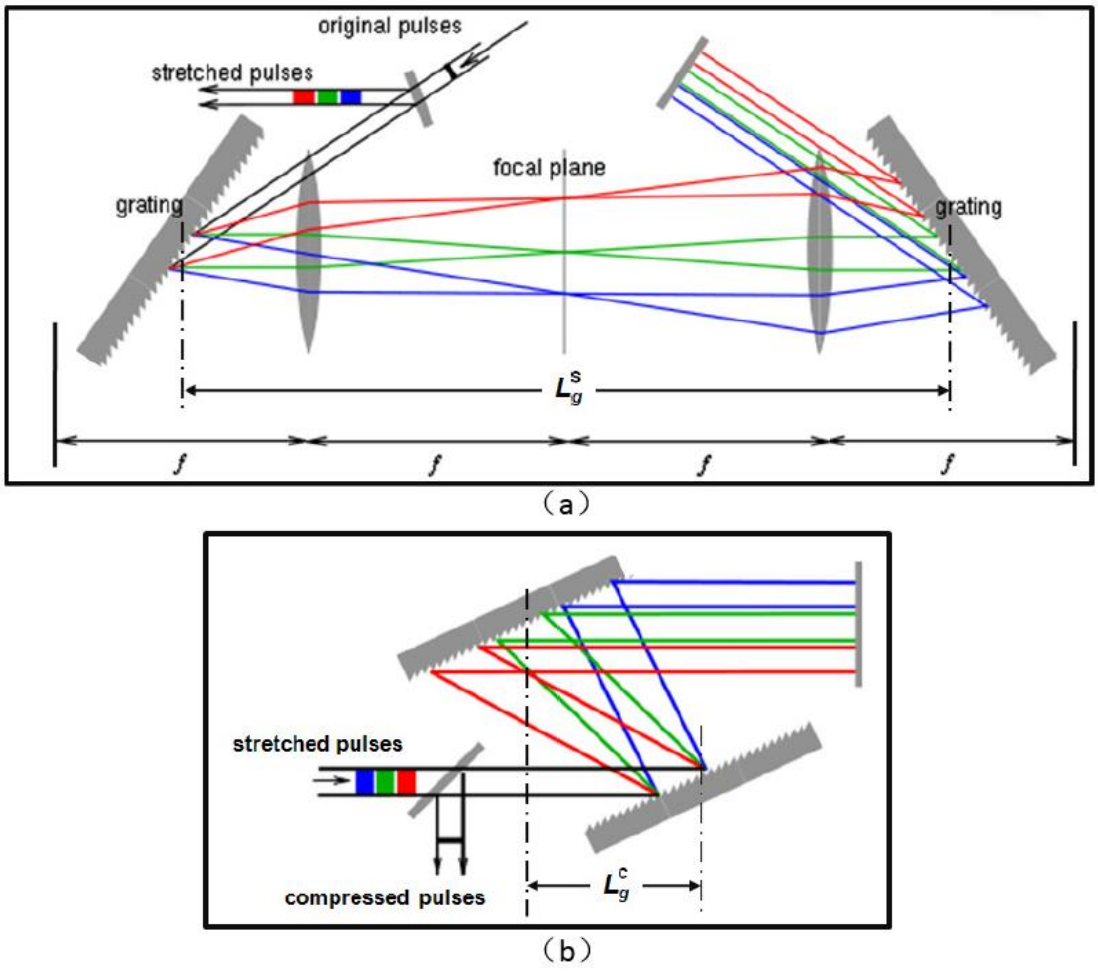

Figure 2.4 Diagrammatic scheme of grating-pair pulse stretcher (a) and compressor (b) [25]

2.2 Ultrafast laser material interaction

In micromachining with lasers, material removal takes place through the ablation process where the target material under laser irradiation absorbs energy and transforms into either a liquid or a vapour. The melted liquid is expelled from the interaction region by the recoil action. The recoil action is created by the vapour with high pressure that pushes the melted liquid away, while the vapour removes itself directly from the focus. Additionally, other processes such as heat conduction, radiation and plasma expansion are associated with the laser material interactions.

When the laser energy is deposited in a surface layer, the thickness of the layer is given by the optical penetration skin depth:

$$I_s = \frac{1}{\alpha} \tag{2-1}$$

where α is the absorption coefficient. Another characteristic length called the heat diffusion length during the laser pulse gives the heat penetration depth due to the thermal conduction. This diffusion length is given by:

$$I_d = \sqrt{D\tau_p} \tag{2-2}$$

where *D* is the heat diffusion coefficient and τ_p is the laser pulse duration. For long pulses, $I_d > I_s$, materials are heated the by the laser pulse and the temperature is determined by the heat diffusion length during the laser pulse. On the other hand, for

a short pulse laser, $I_d < I_s$, the skin depth determines the heated volume during the laser pulse, not the heat penetration depth [28, 29].

2.2.1 Long pulse regime

As shown in Figure 2.5, for long pulses laser interaction with material, the processing can be very unstable due to the complicated fluid dynamics of the fluid phase. The ablation and material removal is accomplished by melting expulsion driven by the vapour pressure [30, 31]. The heat diffusion is sometimes associated with the formation of surface shock waves. These shock waves can damage nearby device structures and lead to irregular shapes of crater during solidification, which cause different mechanical properties from the original material. It is generally true that the more energy is deposited in the micromachining process, the stronger the associated shock waves. Additionally, the solidification can lead to irregular shape of the crater, causing change of the properties from the original material.

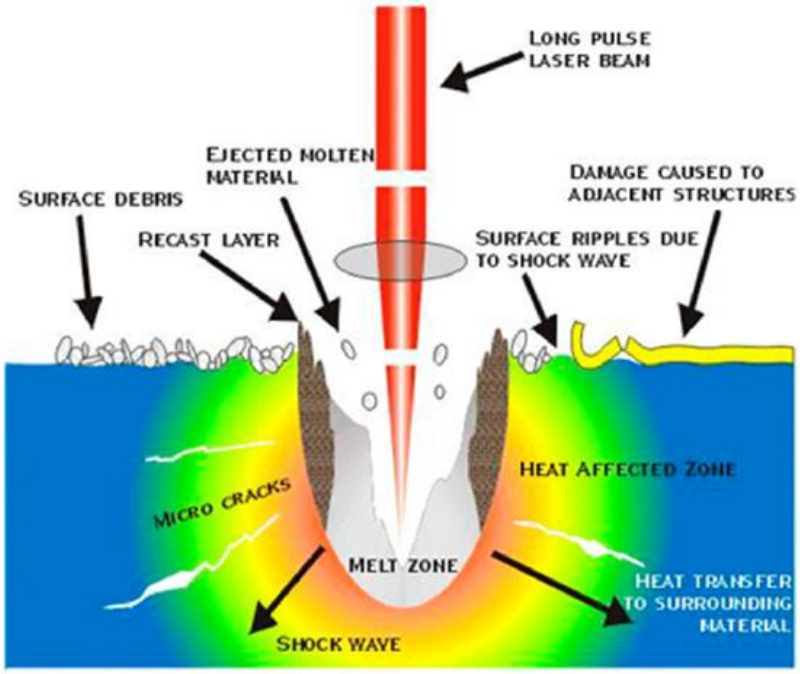

Figure 2.5 Schematic of long pulse induced laser material ablation [31]

When processing using long pulse laser, a balance between efficiency and quality should be considered. Large pulse energy usually leads to a higher efficiency and more recast material on the sidewall while small pulse energy gives better process quality and lower efficiency.

2.2.2 Ultrashort pulse regime

When a laser beam is illuminated on the surface of material, the energy absorption process can be described by three stages, i.e. light absorption, electron thermal diffusion and electron-lattice relaxation [32, 33, 34]. For metallic material, the absorbed energy is transferred to the outer electrons first and causes vibration. This

electron-photon coupling processing usually takes 1 to 100 picoseconds. Then the energy is transferred to the lattice and causes rise in temperature. For ultrashort pulse laser, the pulse duration ($< 10\text{ps}$) is comparable to or shorter than the electron-photon coupling time, thus the heating for lattice is very small. Therefore, the heat effects caused by ultrashort pulses is much smaller then it caused by long pulses. In some semiconductors or dielectric materials, the electron thermal diffusion is so strong that cause their separation from the bulk material, leaving behind ions which repel each other and leave the bulk substrate material. The process is referred to as a Coulomb explosion [35].

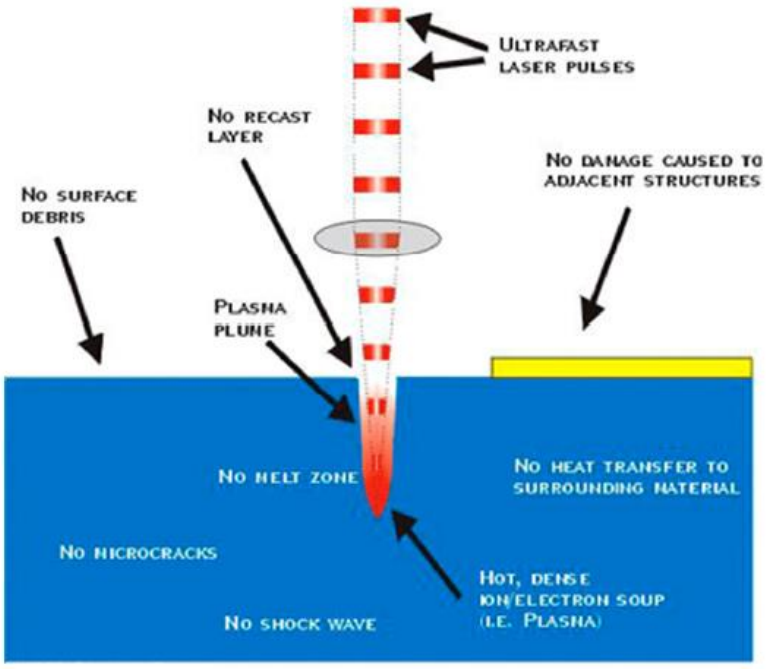

Figure 2.6 Schematic of short pulse induced laser material ablation [31].

As shown in Figure 2.6, for ultrashort pulses, laser energy absorption takes place on an ultrafast timescale so that heat diffusion is negligible on this timescale. The localized energy heats the material very quickly past the liquid phase to the vapour phase with high kinetic energy. The material removal is by direct vaporization away from the surface into vacuum or air [36, 37]. Most of this is accomplished after the laser pulse irradiation is finished and there is rapid cooling due to the steep temperature gradient. Compared to long pulses lasers, the ablation and material removal become highly precise with nearly no heat affect zone (HAZ).

2.3 Phase and polarization

2.3.1 Phase

Beam emitted from laser cavity is a form of self-propagating coherent transverse oscillating electromagnetic wave. In electromagnetic waves, phase can be defined as the position of a point in time on the wave, or the position of a point on the wave where it has a specified amplitude value. Phase front or wavefront is defined as a surface of constant phase of a coherent propagating electromagnetic wave. When there is no phase difference among a group of coherent waves propagating in the same direction, the waves can be called in-phase, the wavefront is a plane.

2.3.2 Polarization

Polarization is one important property of light. By definition, it is described by specifying the orientation of the wave's electric field at a point in space, over one period of oscillation of the wave [38]. In the case of a linear polarization, the electric field of the electromagnetic wave is oscillating alternately up and down in a plane perpendicular to the direction of propagation. With elliptical polarization, the strength and the direction of the electric field of a wave are both varying during the propagation. Circular polarization is a particular case of elliptical polarization, in which the strength of the electric field keeps the same but the direction of the electric field changes in a rotary manner during the propagation. Figure 2.7 shows a schematic diagram of these different polarizations. Linear, elliptical and circular polarizations are termed spatially homogeneous, so that the state of these polarizations do not depend on the spatial location in the beam cross section.

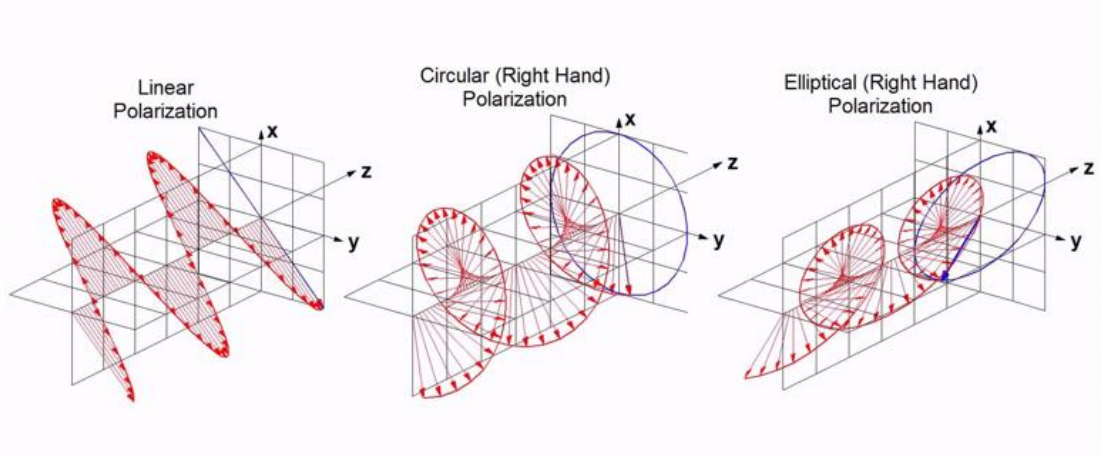

Figure 2.7 Schematic diagram of different polarizations [39]

2.3.2.1 Introduction to Jones calculus

A polarized light can be descried using the Jones calculus, discovered by R.C.Jones. Polarized light is represented by a Jones vector, and linear optical elements are represented by Jones matrices [40]. When light crosses an optical element, the result of polarization is found by taking the product of the Jones matrix of the optical element and the Jones vector of the incident light. The derivation process of a Jones vector is presented as below.

The electric field of a transverse wave can be regarded as the real part of the complex vector. The Maxwell column can be expressed as:

$$\begin{bmatrix} E_x \\ E_y \end{bmatrix} = \begin{bmatrix} H\exp i\{\omega(t-\alpha)+\phi_x\} \\ K\exp i\{\omega(t-\alpha)+\phi_y\} \end{bmatrix} \quad (2\text{-}1)$$

Where E_x and E_y are complex vectors in horizontal and vertical direction, H and K are their amplitude and ω, t, α, ϕ together represent their phase states. Notes that the time-dependence and the z-dependence of the beam are transferred outside the column as a scalar multiplier, so we have

$$\begin{bmatrix} E_x \\ E_y \end{bmatrix} = \begin{bmatrix} H\exp(i\phi_x) \\ K\exp(i\phi_y) \end{bmatrix} \exp i\{\omega(t-\alpha)\} \quad (2\text{-}2)$$

Premultiplying the Maxwell column by the complex conjugate of its transpose, the intensity can be obtained as:

$$\mathrm{I} = [E_x^* \quad E_y^*]\begin{bmatrix}E_x\\E_y\end{bmatrix} = (H^2 + K^2) \tag{2-3}$$

And if we predict that E_1 represents the Maxwell column of the beam entering some kind of polarizing device.

$$E_1 = \begin{bmatrix}H_1 e^{i\phi_1}\\K_1 e^{i\psi_1}\end{bmatrix} \tag{2-4}$$

Then the Maxwell column for the beam leaving that device can be represented as E_2.

$$E_2 = \begin{bmatrix}H_2 e^{i\phi_2}\\K_2 e^{i\psi_2}\end{bmatrix} \quad \text{and} \quad \begin{matrix}H_2 e^{i\phi_1} = J_{11}H_1 e^{i\phi_1} + J_{12}K_1 e^{i\psi_1}\\K_2 e^{i\psi_2} = J_{21}H_1 e^{i\phi_1} + J_{22}K_1 e^{i\psi_1}\end{matrix} \tag{2-5}$$

or, in matrix form,

$$E_2 = \begin{bmatrix}H_2 e^{i\phi_2}\\K_2 e^{i\psi_2}\end{bmatrix} = \begin{bmatrix}J_{11} & J_{12}\\J_{21} & J_{22}\end{bmatrix} * E_1 \tag{2-6}$$

Jones calculus can be derived from equation 2-6. The matrix consisting of the four J_s is called the Jones matrix *J* of the device, E_1 and E_2 is called the Jones vector of a polarized light. The matrix equation can finally be written in the form,

$$E_2 = JE_1 \tag{2-7}$$

If a polarized beam passes through two devices in series with Jones matrix J_1 and J_2. The Jones vector of the original beam is E_1, the beam between the devices is E_2 and that after the second device is E_3. It can be derived that:

$$E_2 = J_1E_1 \text{ and } E_3 = J_2E_2 \tag{2-8}$$

Substituting from the first equation in to the second:

$$E_3 = (J_2 J_1) E_1 \tag{2-9}$$

Thus, the effect of a number of devices in series on a beam of light can be obtained by multiplying together their Jones matrices.

2.3.2.1 Jones matrices for optical components

A number of optical elements influence the orientation of the polarization, and they can be generally classified into two catalogs: polarizers and wave plates. A linear polarizer transmits light polarized along the transmission axis and cut off waves of the orthogonal linear polarization. On the other hand, a wave plate alters the polarization state of a light wave travelling through it. The effects of such elements on a light wave can be described using Jones matrices. The Jones matrices for several optical elements are represented in Table 2.1.

Table 2.1 Jone Matrices for some linear optical elements [40]

Optical element	$\theta = 0$	$\theta = \frac{\pi}{2}$
Linear polarizer at angle θ	$\begin{bmatrix} 1 & 0 \\ 0 & 0 \end{bmatrix}$	$\begin{bmatrix} 0 & 0 \\ 0 & 1 \end{bmatrix}$
Quarter-wave plate with fast axis at angle θ	$\begin{bmatrix} 1 & 0 \\ 0 & -i \end{bmatrix}$	$\begin{bmatrix} -i & 0 \\ 0 & 1 \end{bmatrix}$
Half-wave plate with fast axis at angle θ	$\begin{bmatrix} 1 & 0 \\ 0 & -1 \end{bmatrix}$	$\begin{bmatrix} -1 & 0 \\ 0 & 1 \end{bmatrix}$
Linear retarder with retardation σ and with fast axis at angle θ	$\begin{bmatrix} 1 & 0 \\ 0 & e^{-i\sigma} \end{bmatrix}$	$\begin{bmatrix} e^{-i\sigma} & 0 \\ 0 & 1 \end{bmatrix}$

In this thesis, some of the above elements are employed to change the polarization of a laser beam.

2.4 Introduction to spatial light modulator (SLM)

Spatial light modulator (SLM) is a powerful device based on liquid-crystal technology for modulation of both phase and polarization of an incident laser beam. Since they have been firstly employed in optical computing in 1980s [41], they have become popular in many research areas, such as spatial beam shaping [42, 43, 44], wavefront correction [45, 46] and laser parallel processing [47, 48, 49].

2.4.1 Structure and working principle of SLMs

SLMs can be mainly classified into two families: electrically addressed SLM and optically addressed SLM. For an optically addressed SLM, the image is created and changed by shining light encoded with an image on its front or back surface. A photosensor allows the SLM to sense the brightness of each pixel and replicated the imaging using liquid crystal. They are often used as the second stage of a very-high-resolution display.

On the other hand, the image on an electrically addressed SLM is created and changed electronically. It can be divided into reflective SLM and transmissive SLM. In this experimental work of thesis, two reflective Liquid-Crystal On silicon (LCOS) SLMs have been employed (see Figure 2.8).

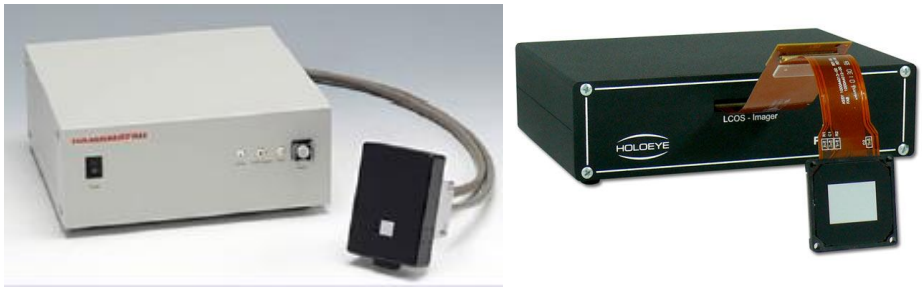

(a) Hamamastu X10648 [50] (b) Holoeye LC-R2500 [51]

Figure 2.8 Pictures of SLMs employed in this work

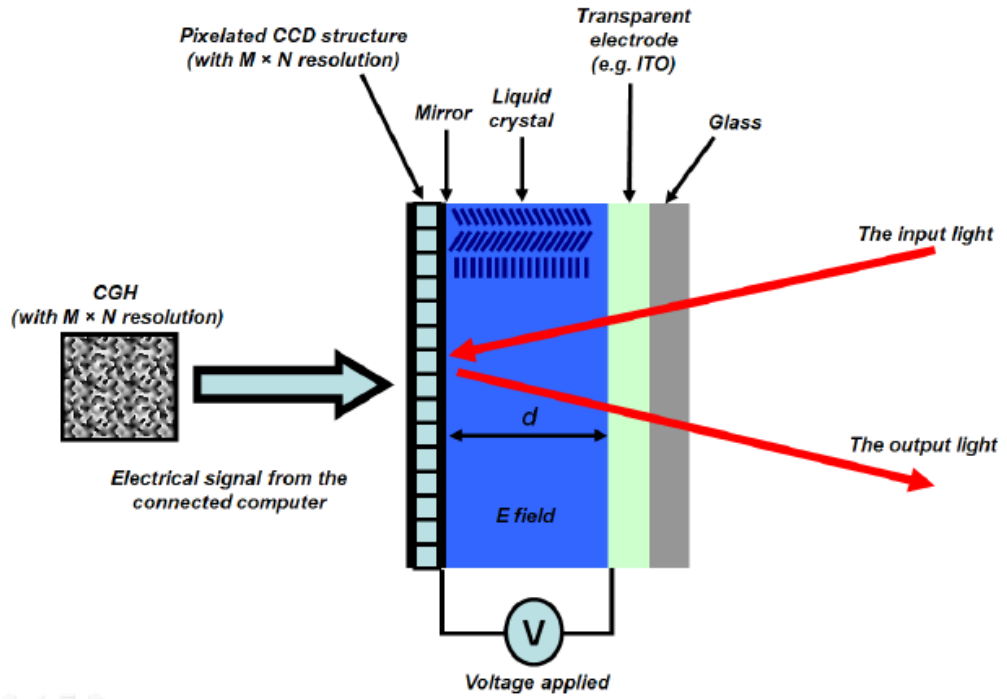

Figure 2.9 The basic structure of a SLM [52]

For most reflected electrically addressed SLMs, a layer of nematic liquid crystal display (LCD) is applied and attached to a reflecting silicon substrate (see Figure 2.9). The silicon substrate is a Charge-Coupled Device (CCD) chip, having a two dimensional array structure which can electrically load data from the images applied on SLMs. Each pixel is independently driven by an accurate voltage controlled by the grey level of images. Under the each voltage, the liquid crystal molecules makes a rotation at a specific angle, resulting in a refractive index change. Consequently, the phase and polarization state of the incoming light is modulated after reflection.

The liquid crystal SLMs can be further divided into two categories, twisted nematic

liquid crystal devices and parallel aligned nematic liquid crystal devices. In a reflective twisted nematic SLM, there is a certain angle difference between two director plates at the bottom and the top of the liquid crystal layer. Polarized beam passing through these cells follows the helical molecule axes, leading to a change in polarization direction. However, in a parallel aligned nematic device, the liquid crystal molecules comprise two parallel director plates. Therefore, it can modulate the phase of the incident beam along the molecular axis and leaving the perpendicular direction completely unaffected.

2.4.2 Algorithms for calculating computer generated hologram (CGHs)

According to Fourier optics, for a laser beam passing through a hologram and a focusing lens, there is a Fourier transform relationship between the complex amplitude of the holograms on SLMs (t) and the complex amplitude at the focal plane (U_f) [53].

$$U_f \propto \mathcal{F}(t) \tag{2-10}$$

Where the $\mathcal{F}$ represents Fourier transformation. Additionally, if the distance between the hologram and the lens is 0, the diffractive pattern at focal plane becomes the exact Fourier transformation of the hologram.

The image space field can therefore be regarded as a scaled version of the far-field

diffraction pattern that would be produced by the beam leaving the SLM. Theoretically, if one of the t or U_f is known, it should be straightforward to calculate the other unknown field by taking the forward or inverse Fourier transform of the known field. However, for a normal SLM, it modulates only the phase of the incident beam but leave the intensity unchanged, thus the hologram is insufficient to present all the factors of a complex amplitude. Therefore, algorithms for calculating the phase holograms have been developed to optimize the accuracy for far-field intensity patterns.

The CGHs for producing multiple beams can be calculated by several algorithms, including Gerchberg-Saxton (GS) [54], Gratings and Lenses (GL) [55], Weighted GS (GSW) [56], Generalised Adaptive Additive (GAA) [10] , optimal rotation angle (ORA) [12], Multiplexed Phase Fresnel Lenses (MPFL) [57] and Mixed-Region Amplitude Freedom (MRAF) [58]. Among these algorithms, the GS algorithm is most widely used for micro-processing due to its good accuracy and fast calculation speed.

The GS algorithm is an iterative algorithm for retrieving the phase of two light distributions related via the Fourier transform. Figure 2.10 illustrates the flow chart of the generation of a phase hologram with the GS algorithm.

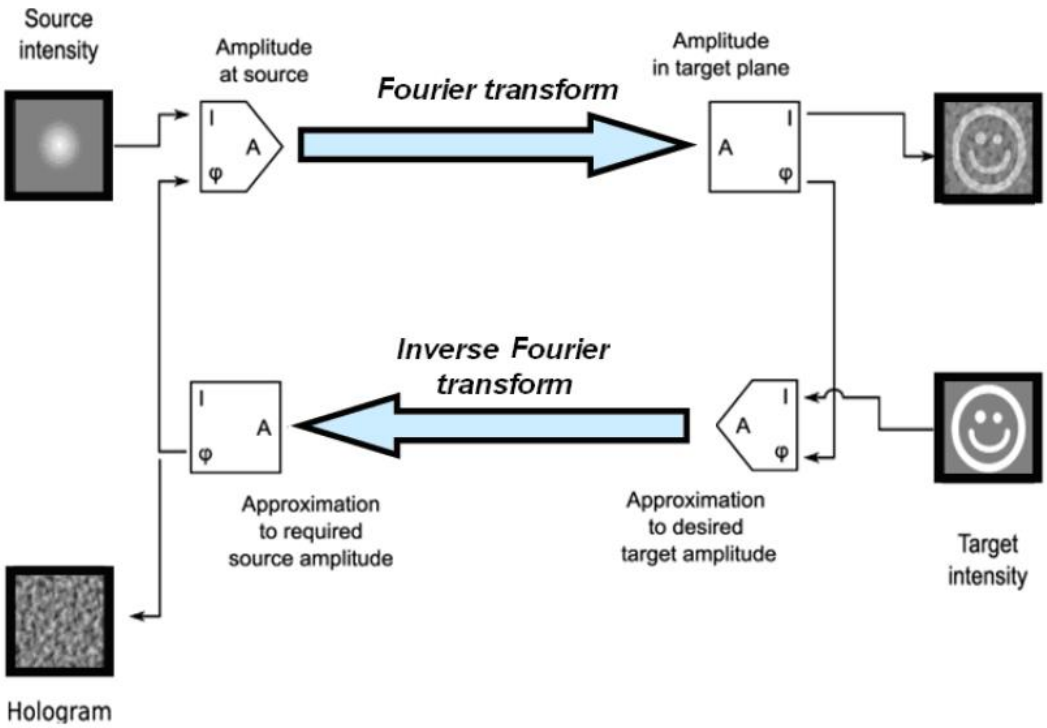

Figure 2.10 The diagram graphically shows how to generate a phase hologram with the GS Algorithm [59]

The target laser intensity distribution or the diffractive pattern on the focal plane is defined as $I_f = U_f(x_f, y_f)^2$, and the aim is to find a phase distribution on SLM $\varphi_0(x_0, y_0)$ that $\mathcal{F}(\{\exp(i\varphi_0)\})^2 = I_f$. To find the desired phase φ_0, the algorithm starts at the hologram plane with a random φ_r and constant unit amplitude. Therefore, the initiate phase distribution of the CGH is:

$$t_1 = \exp(i\varphi_r) \tag{2-11}$$

For the first and subsequent iteration, the light field is propagated to the image space by taking its Fourier transform, i.e. for the *k*th iteration:

$$U_{f,k} = \mathcal{F}(t_k) \tag{2-12}$$

Then, the light field in the image space is modified by keeping the phase but replacing the intensity with the target intensity I_f:

$$\varphi_k = \arg(U_{f,k}) \tag{2-13}$$

$$U_{f,k}{}' = \sqrt{I_f}\exp(i\varphi_k) \tag{2-14}$$

The resulting light field is then propagated back to the hologram plane by taking its inverse Fourier transform:

$$t_{k+1} = \mathcal{F}^{-1}\{U_{f,k}{}'\} \tag{2-15}$$

The iteration is finally completed by again keeping the phase but replacing the intensity with uniform constant intensity:

$$\varphi_{k+1} = \arg(U_{f,k+1}) \tag{2-16}$$

$$U_{f,k+1}{}' = \exp(i\varphi_{k+1}) \tag{2-17}$$

With a few interaction, the algorithm converges such that the argument of light field at hologram plane is the phase required to produce the target field in image space. The GS algorithm has also been applied for two-dimensional intensity distributions and modulating intensity distribution in several planes simultaneously [57]. Later, Sinclair et al. [60] have successfully applied this technique in optic tweezers,

simultaneously trapping several objects in individually controllable arbitrary three-dimensional positions.

2.5 Introduction to laser beam shaping

2.5.1 Typical intensity distributions of laser beams

Beam shaping is the process of redistributing the irradiance and phase of a beam of optical radiation.

Most lasers operate in the fundamental transverse electromagnetic mode of the cavity (TEM_{00}) or Gaussian structure. Notably, the Fourier transform of a Gaussian beam remains a Gaussian and thus preserves is shape as it passes through an optical system consisting of simple lenses [61]. This is especially important in laser processing, where multiple optical elements are typically employed to guide the laser radiation to the workpiece. The Gaussian beam of given diameter also has the lowest divergence, which allows for a small focused spot, which makes Gaussian beams ideal for mirco-fabrication applications.

Top-hat beams are also widely used for many applications such as laser printing [62] , thin film processing [63], material annealing [64], material deposition [65] and laser welding with improved weld quality and repeatability [66]. This due to the fact that the same interaction is accomplished over the illuminated area. Top-hat beams with

varying degree of uniformity can be generally produced by excimer lasers. Some optical elements are also used as beam shapers to transfer the Gaussian mode to Top-hat mode. However, unlike with Gaussians, a Top-hat beams does not maintain its shape during propagation, and the focused beam waist is larger due to a much higher M^2, which is known as the beam quality factor, represents the degree of variation of a beam from an ideal Gaussian beam. The beam diameter at the focus can be expressed as equation 2.18 [67]:

$$d_f \approx \frac{4\lambda f}{\pi}\frac{M^2}{\mathrm{D}} \tag{2-18}$$

Where λ is the wavelength of the laser, f is the focal length and D is the diameter of the entrance pupil. Top-hat beams have an M^2 value much higher than 10, however, M^2 for a perfect Gaussian is 1. Thus, it can be deduced that the minimum beam spot for Top-hat laser will not be as small as with Gaussian beam, and the depth of field will not be as long.

Furthermore, there are several non-conventional intensity distributions which give advantages over Gaussian or Top-hat in some specific applications. Bessel beams [68] and Airy beams [69] are used in optical manipulation, which allowed the simultaneous trapping of several particles at the same time of the transport of 60μm microspheres over a distance of half a meter. Bessel beam is defined as a beam whose electric field is explicitly described by a zeroth-order Bessel function of the first kind (J_0) [61]:

$$E(r, \varphi, z) = A_0 \exp(ik_z z) J_0(k_r r) \quad (2\text{-}19)$$

Where r and φ are transverse and polar coordinates, z is the coordinate in the propagation direction, and k_z and k_r are the longitudinal and radial wavectors. Since the beam intensity is proportional to the square of the electric field for a Bessel beam, this beam appear as a series of concentric rings rather than a single spot, as shown in Figure 2.11 (c). A region of self-interference develops in which the Bessel pattern emerges due to cylindrical symmetry.

When the Bessel beam is in the far field, as the separation between the wave vectors increases, the beam intensity in the central axis decreases and eventually attain a null value. In this case, this beam changes to an annular beam, which is also known as a doughnut-shaped beam, as shown in Figure 2.11 (d). An annular beam has applications in laser drilling [70] and micromachining [71, 72, 73].

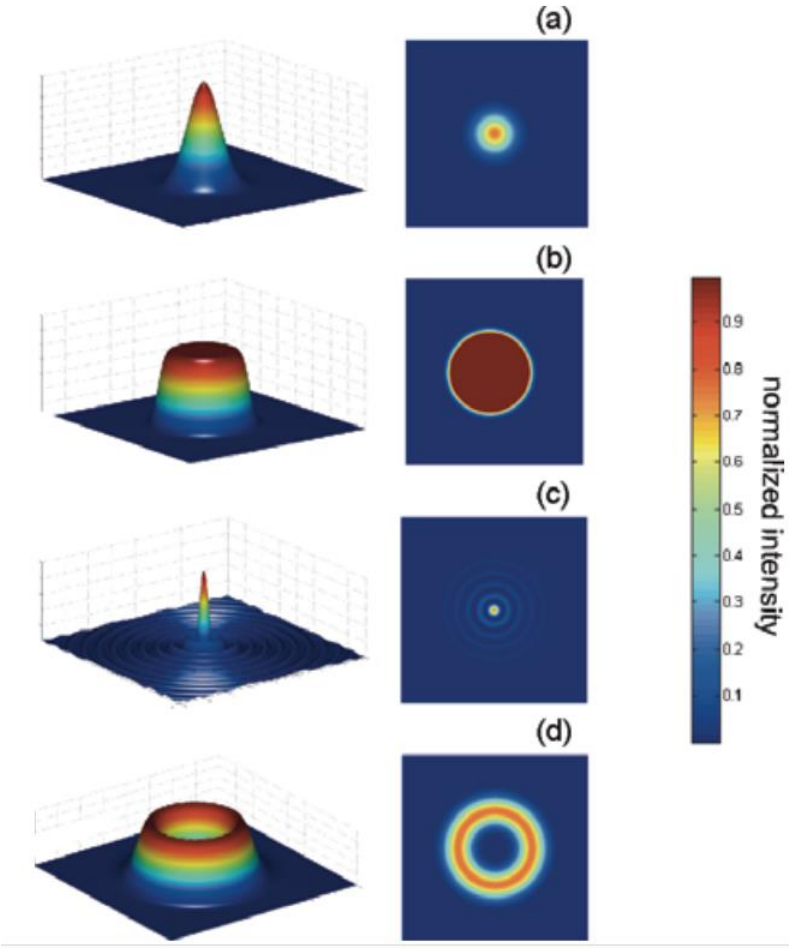

Figure 2.11 2D and 3D intensity distribution of (a) Gaussian beam; (b) Top-hat beam; (c) Bessel beam; (d) annular beam [61].

2.5.2 Laser beam shaping using geometrical optics

When diffraction effects are not important, geometrical optics can be used to design laser beam shaper by solving beam shaping equations or by optimizing a beam shaping merit function for the configurations [74]. Geometrical optics has been widely used

for design of laser beam shaping system since 1960s [75]. In early works, geometrical optics was used to determine the configuration of a two-element optical system that would transform a Gaussian input into an output with uniform irradiance or a flattop distribution. Frieden showed that the phase of output plane might have a phase distortion about 20λ from the incident beam after the optics, unless a second optical element corrects this distortion [8]. Krezuer presented that design of constant optical path length condition for all rays passing through the beam shaping optics to control phase variation of the output beam [76]. After that, a two-element afocal beam shaper with a concave aspheric lens and a convex aspheric lens was designed based on beam shaping equations [77]. The designed beam shaper was then fabricated, tested and used for beam shaping within a holographic projection system [78, 79]. Shafer [80] designed beam shapers using afocal doublet lenses with spherical optics and successfully transform a Gaussian beam into a flattop distribution with a diffraction-limited output wavefront. For refractive systems, two shapers were designed for shaping a circular symmetric input Gaussian laser beam into a circular symmetric uniform output beam, and an annular Gaussian beam into a circularly symmetric uniform output beam [81, 82]. Yamamota [83] developed an anamorphic lens for transforming an elliptical beam into a circular symmetric beam with two different surfaces, where the first surface had a rotationally symmetric optic power with respect to the optical axis, and the second surface is toric surface with different optical powers

along perpendicular direction. For reflective beam shaping applications. Conservation of energy within a bundle of rays was used to design rotationally symmetric systems for illuminating a receiver surface in a prescribed manner using a non-uniform input beam profile [84]. Optical design of beam shapers can be achieved using either physical or geometrical optics.

An optical field can be expressed using Maxwell's equation or the scalar wave equation [85]

$$u(\mathrm{r}) = u_0(\mathrm{r})\exp[ik_0 S(\mathrm{r})] \tag{2-20}$$

where k_0 is the wave number in free space; and $u_0(\mathrm{r})$ and $S(\mathrm{r})$ are unknown functions of r. Requiring that $u_0(\mathrm{r})$ from equation (2-20) satisfy the scalar wave equation leads to the following conditions:

$$(\nabla \mathrm{S})^2 = n^2 \tag{2-21}$$

$$2u_0 \nabla \mathrm{S} \cdot \nabla u_0 + {u_0}^2 \nabla \mathrm{S} = \nabla \cdot ({u_0}^2 \nabla \mathrm{S}) = \nabla \cdot ({u_0}^2 n\mathrm{a}) = \nabla \cdot (I\mathrm{a}) = 0 \tag{2-22}$$

where n is the index of refraction, and *I* is the energy density of the field times the speed of propagation within the medium. Equation (2-21) is known as the Eikonal equation and is the basic equation of geometrical optics. The surfaces S=const are constrant phase front of the optical field, have a constant optical path length (OPL) from the source or reference surface, and are known as the geometrical wavefront.

Equation (2-22) expresses conservation of radiant energy with a bundle of rays and is known as the geometrical optics intensity law for propagation energy. The ray paths are evaluated throughout the optical system with ray tracing [86]. Then, the phase of the optical field is calculated based on the optical path length of the rays passing through the system. The optical field can be computed from the density of ray at any point within the system by monitoring the irradiance variations along each ray [87, 88, 89].

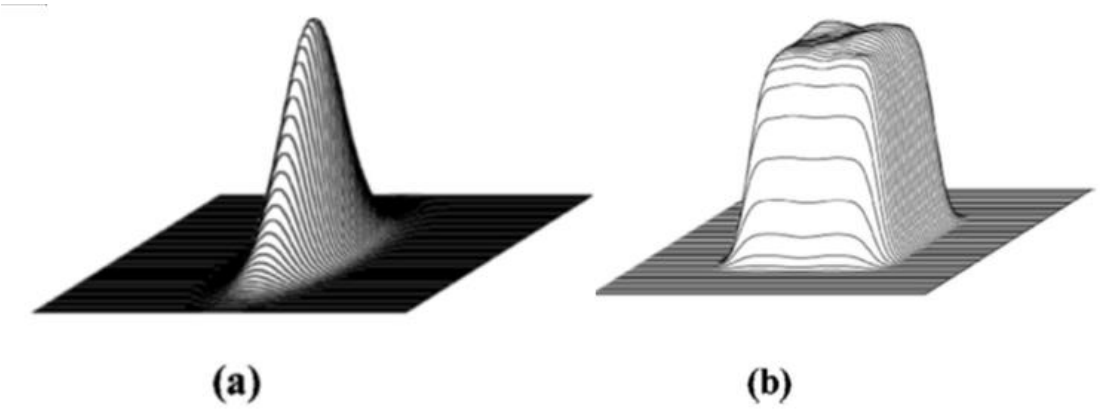

Figure 2.12 Beam shaping using Cornwell's recipe (a) Elliptical Gaussian input beam profile with (b) output Fermi-Dirac beam profile and simulated by ZEMAX [74]

A method for designing two-element beam shapers to obtain a flattop beam profile was introduced by Cornwell [90]. By comparing the power expression for intensity distributions over the input and output planes, a set of calculations were made based on real parameters to obtain a beam shaper with specific shaping properties (see Figure 2.12).

2.5.3 Optimizations for laser beam shaping

2.5.3.1 Uniformity control for parallel processing

For parallel processing, the uniformity control of diffractive patterns is a significant parameter, since many industrial applications would require that all the diffractive beams have a good identity to ensure consistent processing. The uniformity of the diffractive pattern is not only affected by the algorithm used to calculate the CGH, but also the geometric design of the diffractive pattern [91]. A slight spatial disordering of periodic and symmetric patterns can significantly reduce intensity variations among each of the desired diffractive peak. A better uniformity of diffractive pattern has been demonstrated by improving the CGH calculation algorithm, e.g. adding iterative calculation to minimize the uniformity error of the computationally diffractive peak [92, 93] or taking into account of the intensity distribution of the irradiated laser pulse and the spatial frequency response the SLM [93, 94, 95]. The uniformity of diffractive patterns can also be changed by varying the geometric pattern design [11, 91]. As shown in Figure 2.13, a pico-second laser (wavelength: λ=1064nm, repetition: f=10kHz and pulse energy: E_p=3.8μJ) has been employed for parallel processing on Indium tin oxide(ITO) samples. Due to the degeneration caused by overlap of unwanted diffraction peaks, the desired diffracted multiple beams cannot be perfectly identical. Energy variation among the diffracted beam is unavoidable [96]. However, by avoiding

periodic and symmetrical geometry design, the diffractive multi-beams shows much higher uniformity [47].

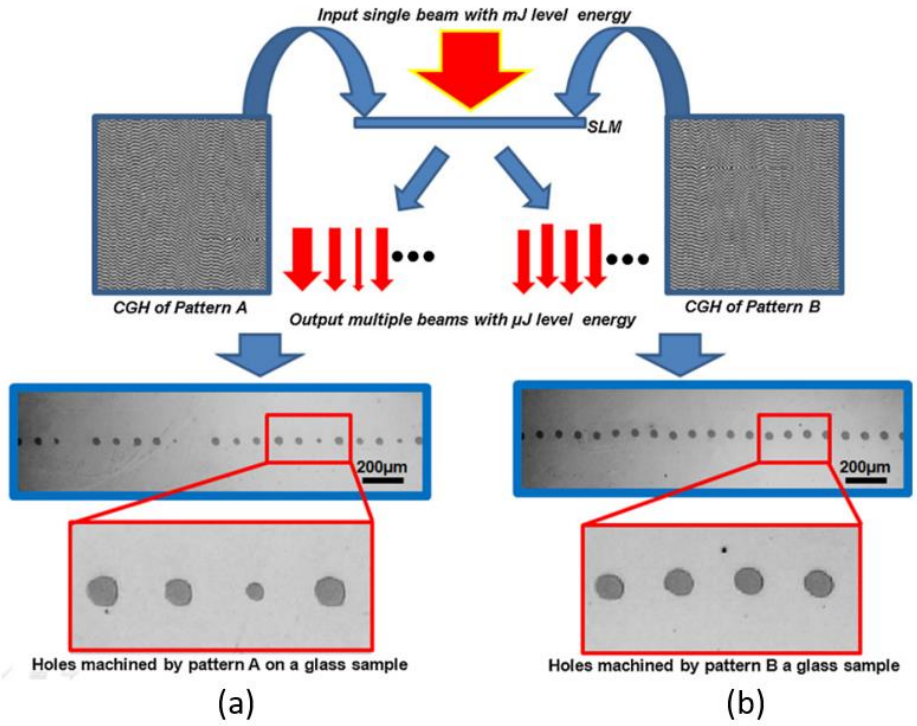

Figure 2.13 Holes machined by parallel laser beams with (a) periodic pattern and (b) disordered pattern [47]

As shown in Figure 2.13 (a), there has been a significant variation of the hole size when machining with the highly periodic pattern. However, the holes machined with disordered pattern have shown a much higher uniformity as in Figure 2.13 (b). This is due to the fact that disordering significantly decreases the probability of overlap of diffracted 'ghosts' [91].

2.5.3.2 Phase and intensity modulation

Precise control over the amplitude and phase of light has allowed significant advances in micro processing [72] and optical trapping [97, 98]. A variety of method have been developed which allow the arbitrary control over the both. Two cascaded phase-diffractive elements displayed on a SLM have been employed to control both phase and amplitude for optical trapping (see Figure 2.14).

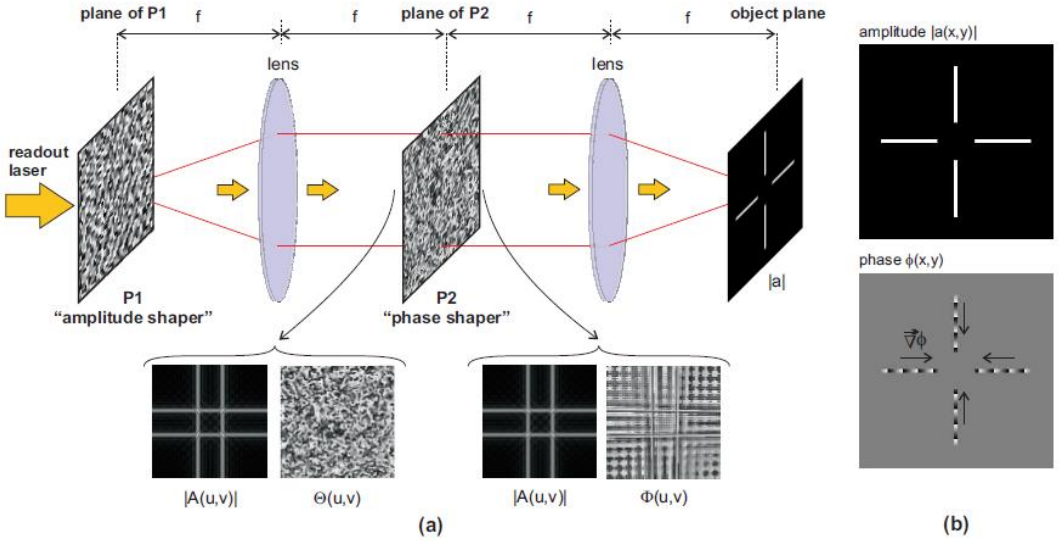

Figure 2.14 (a) The reticle in the object plane are created by two phase masks P1 and P2. (b) Schematic of a trapping light field [99].

Amplitude and phase of the light field are shaped in two steps by two phase diffractive elements (P1 and P2). Both elements are arranged in a 2-f setup. P1 creates the modulus in the plane of P2, where P2 shapes the desired phase. This method permits independent control over amplitude and phase of a light field with a theoretical high

efficiency of 100%.

Holograms calculated using conjugate gradient minimization technique have also been applied for controlling both phase and amplitude [100]. Conjugate gradient minimization is a numerical method to optimize high dimensional function [101]. By tailoring the output-plane amplitude of phase-only holograms, new holograms are generated and applied on SLMs (see Figure 2.15).

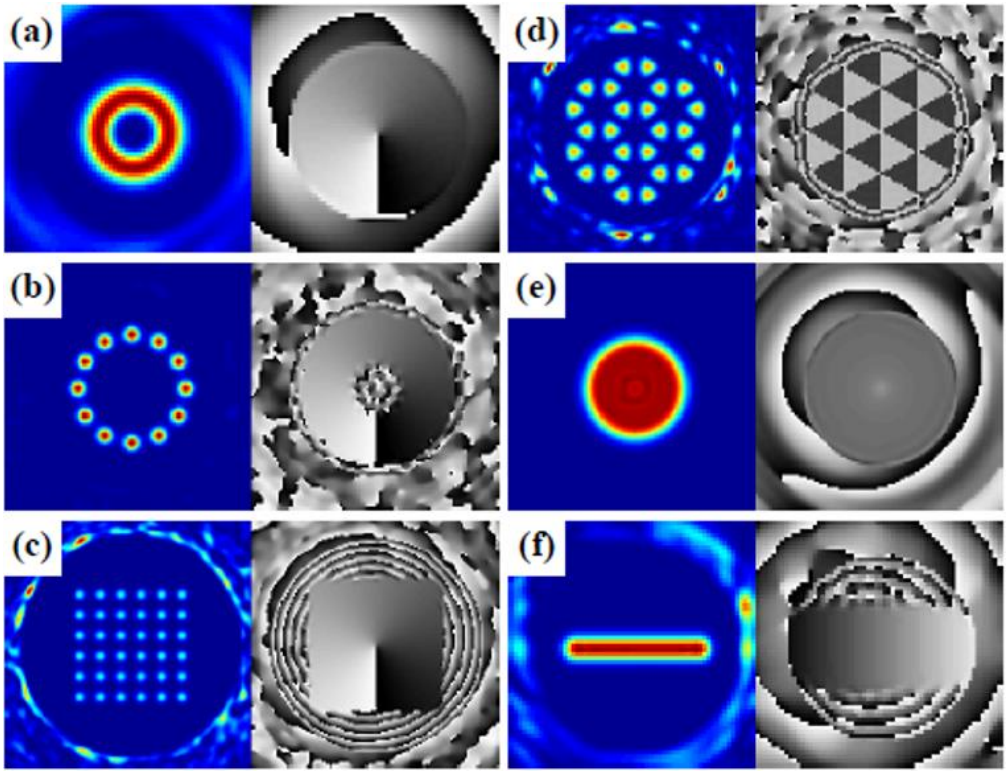

Figure 2.15 The far-field results from the conjugate gradient optimization showing normalized intensity and phase in the region of interest [100].

2.5.3.3 Optical vector field control – vortex beam shaping

Laser beam with a space-variant electric field orientation and amplitude are referred to as vector beam [102]. Radial and azimuthal polarization states are extreme examples of these vector states and can be produced with specific laser cavity design [103], a spatial light modulator [104] or nano-structured waveplates [105]. Vector beams technique is widely used in microscopy [106], optical trapping [107] and ulta-relativistic electron acceleration [108]. Anoop et al [109] recently have generated vortex beams for laser induced periodical surface structure (LIPSS) processing on Silicon with a liquid crystal q-plate, showed a developing radial micro-structure and highlighted the multi-pulse feedback mechanism responsible for plasmon structuring. Yang et al [104] have demonstrated the ability to dynamically modulate radial and azimuthal polarization states in real time along with linearly polarized LG intensity profiles with a 532nm wavelength picosecond laser.

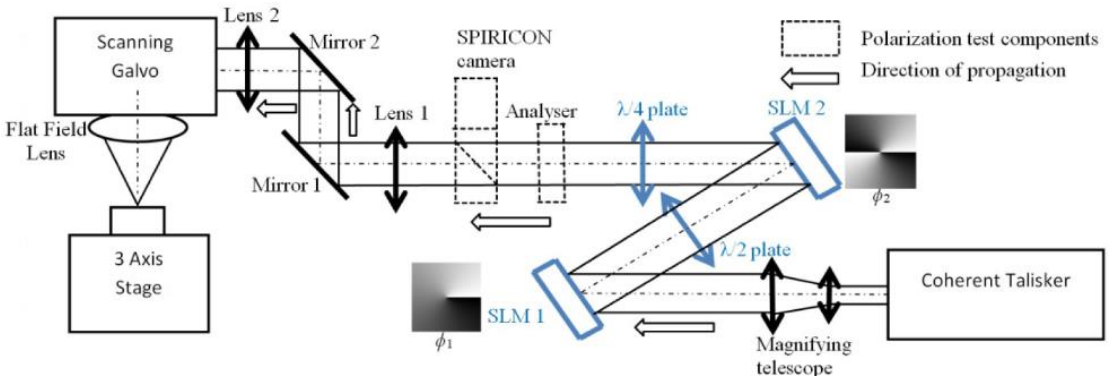

Figure 2.16 Wavefront and polarization control using two SLMs [104]

As shown in Figure 2.16, a horizontal linear polarized incident on the first SLM. A half-waveplate was placed after the first SLM to tilt the polarization direction to 45° and incident on the second SLM. The first SLM is used to control the wavefront whereas the second SLM is used to control the polarization.

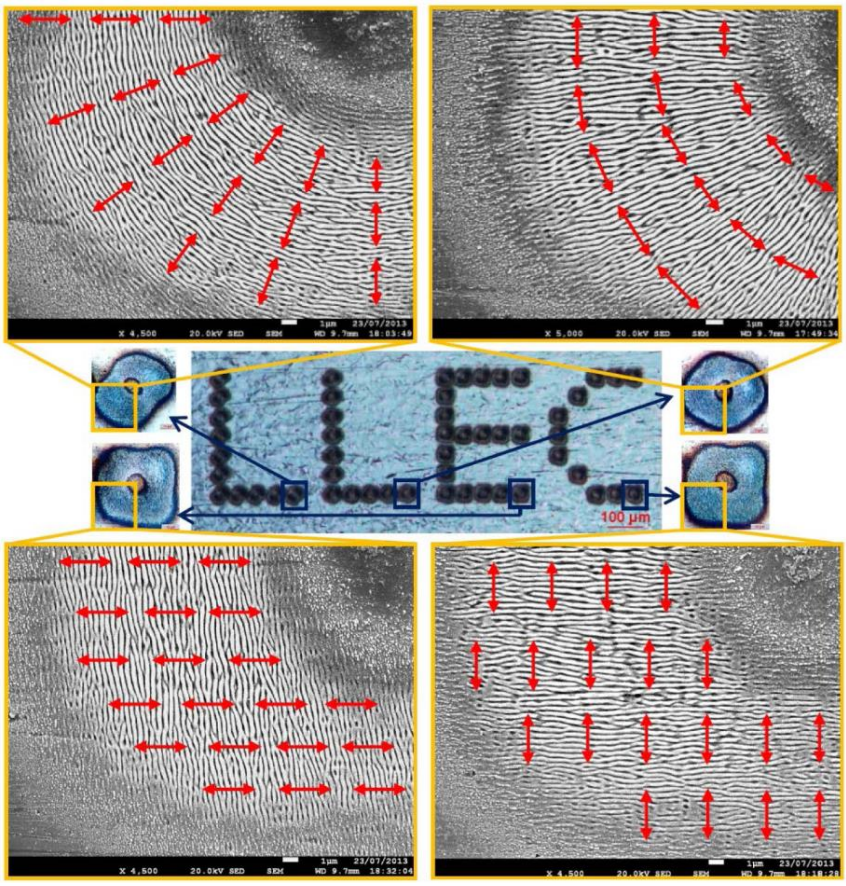

Figure 2.17 Footprints processed by laser beams with controlled wavefront and polarization [104]

As shown in Figure 2.17, each set was processed using a different state of polarization. The ablation spots had been produced either with a radially, azimuthally, horizontally and vertically polarized beam. The laser exposure had led to the developments of laser

induced periodical surface structure (LIPSS) with each spot, which verified the shaped polarization state. Additionally, each produced laser spot had a ring-shaped structure, which was caused by change of the wavefront.

Recently, Ouyang et al [73] had showed a technique for tailoring the optical vector beams using a SLM and a micro-structured S-waveplate. The influence of the Orbital Angular Momentum (OAM) on vector fields have been confirmed by the observed surface mirco-structures. A laser beam was illumined onto a SLM with a spiral phase hologram to control the OAM and then passed through an S-waveplate to obtain radial and azimuthal states. Figure 2.18 shows the measured intensity profile when translating the polarization and the camera in the vicinity of the lens focal plane and reveals a clear distortion between the vector beam with and without the OAM, in which RP, AP and IP refereed to a radial, an azimuthal and an intermediate tilted polarization respectively. All the beam with orbital angular momentum (OAM) had a twisted profile indicating the influence of the OAM on the vector fields.

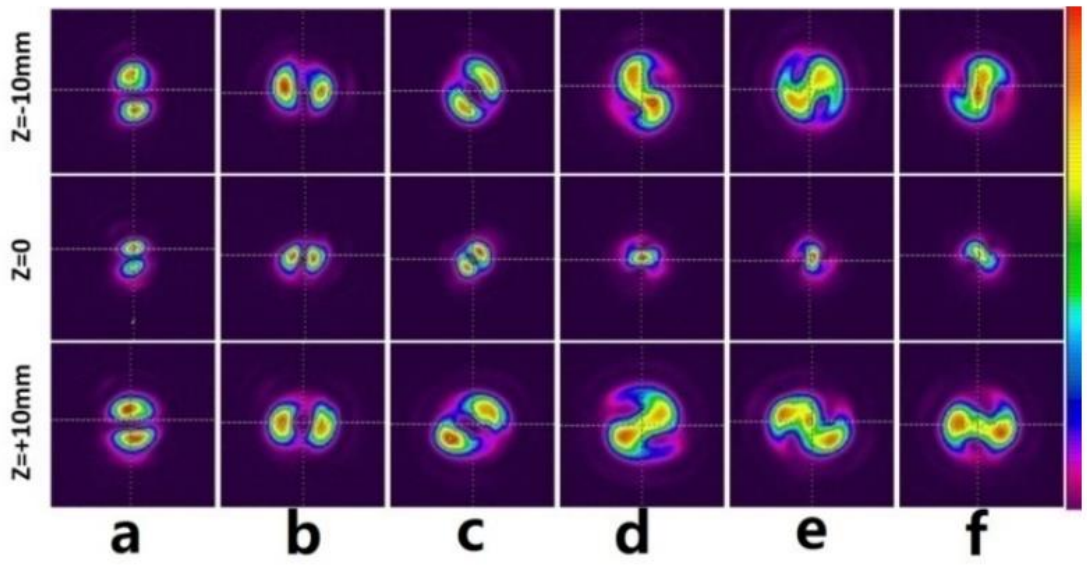

Figure 2.18 Reflected intensity distribution measured when polarization analyzer was translated near lens through focal plane. (a) RP (θ = 0°), (b) AP (θ = 90°), (c) IP (θ = + 45°), (d) RPAOM, (e) APAOM, (f) IPOAM [72].

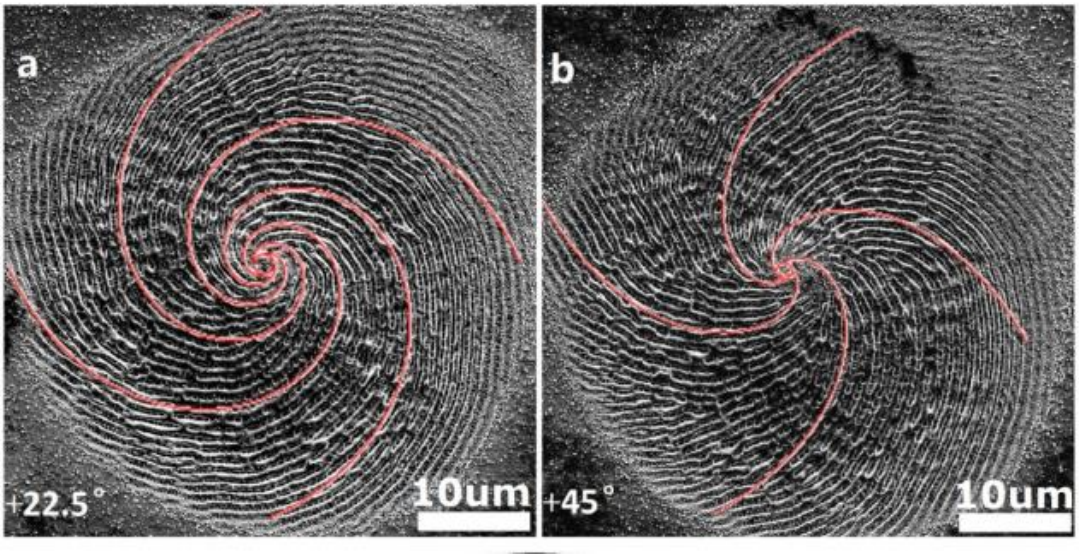

Figure 2.19 SEM images of spiral plasmons from superposition states generated by altering S-waveplate axis θ (a) 22.5° (b) 45° [73]

Figure 2.19 showed the machined results by the shaped vortex beam. It is conjectured

that the superposition of the radial and azimuthal vector field components led to a spiral micro-structures [110].

2.5.4 Conclusions

Beam shaping using geometric optics is a very efficient and accurate method to obtain required irradiance distribution. By setting a target profile, optical elements with specific parameters can be designed and fabricated based on the real beam profile. However, an optical equipment is usually designed for a unique original beam profile and a target irradiance distribution, leading to an insufficient flexibility.

Beam shaping using diffractive method has also been widely employed in last decade, due to the superior phase and polarization modulation ability of a SLM. Modification of outline profile, intensity distribution and diffractive pattern can be achieved by applying Fourier transform based holograms. However, generating holograms is complex and time-consuming progress, and it is also very difficult to obtain arbitrary intensity distributions using this method.

Beam shaping using a spiral phase hologram can modulate the wavefront and generate a ring shape profile by varying OAM. Combined with polarization modulation, interesting LIPSS can be generated at special arrangement. However, only a ring or circular shape can be generated using wavefront control due to the electric field

properties of a laser light.

Therefore, a more flexible and accurate method which adapts to any input distribution and target profile is ideal for a research study.

Chapter 3 Experimental Equipment and Techniques

3.1 Overview of the key laser systems used in this work

3.1.1 Fianium 20ps laser system

The first laser system used in this work was a Fianium FemtoPower 4uJ laser. This laser system is a class-4 fibre laser based source operating with the central wavelength of 1064nm. The system is based on a master source diode pumped passively mode locked fibre laser in the form of a core pumped ytterbium doped fibre. The designed specified pulse length is 20 picoseconds. A pulse picker system positioned after the master source comprising of control electronics, radio frequency(RF) driver, and an acousto-optic modulator (AOM) provides the feature of dividing the fundamental repetition rate (20MHz), resulting in selectable repetition rates of 0.2MHz and 0.5MHz, respectively. The laser and work stage are shown in Figure 3.1.

Figure 3.1 Picosecond Fianium laser

The maximum output power is 1W and the maximum pulse energy is 20μJ measured

at 0.5MHz. The M^2 value is 1.3 measured by a Thorlabs BC106 (camera+stage) beam profiler. The output from this laser was found to be a near Gaussian distribution as can be seen in Figure 3.2.

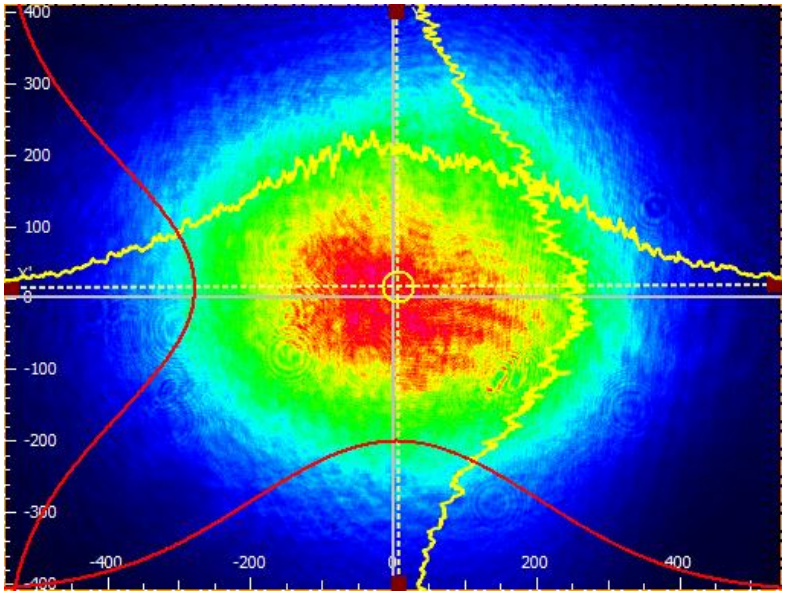

Figure 3.2 Original beam profile of Fianium FemtoPower 4uJ laser measured using a CCD camera (1pixel=6.45um)

3.1.2 High-Q 10ps laser system

The second laser source used in this work was a custom made seeded Nd:VAN regenerative amplifier laser system (High-Q IC-355-800ps [111]) capable of working at 5kHz, 10kHz, 20kHz and 50kHz repetition rate with output wavelengths at 1064nm, 532nm and 355nm. The maximum pulse energy, E*p*>0.1mJ, was measured at 1064nm and 20kHz, with pulse duration $\tau_p \approx$ 10ps. The high-Q IC-355-800ps system is principally comprised of a laser head, a laser controller (including power supply) and

a chiller, as shown in Figure 3.3.

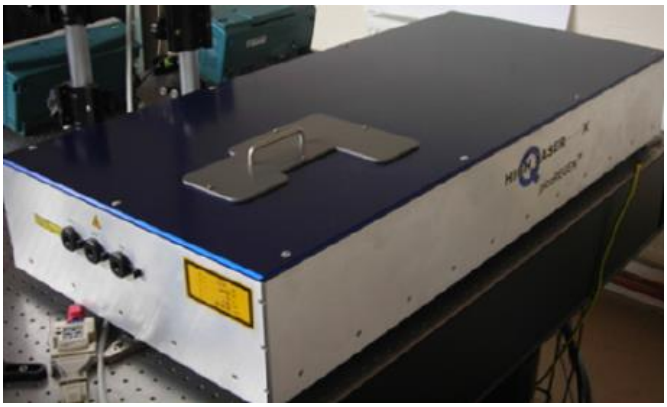

Laser head

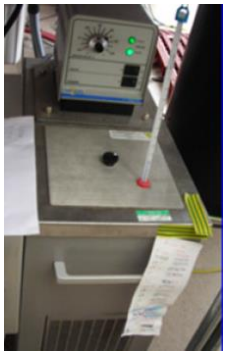

Laser controller Chiller

Figure 3.3 High-Q picosecond laser, consisting of laser head, laser controller integrated with power unit, and chiller

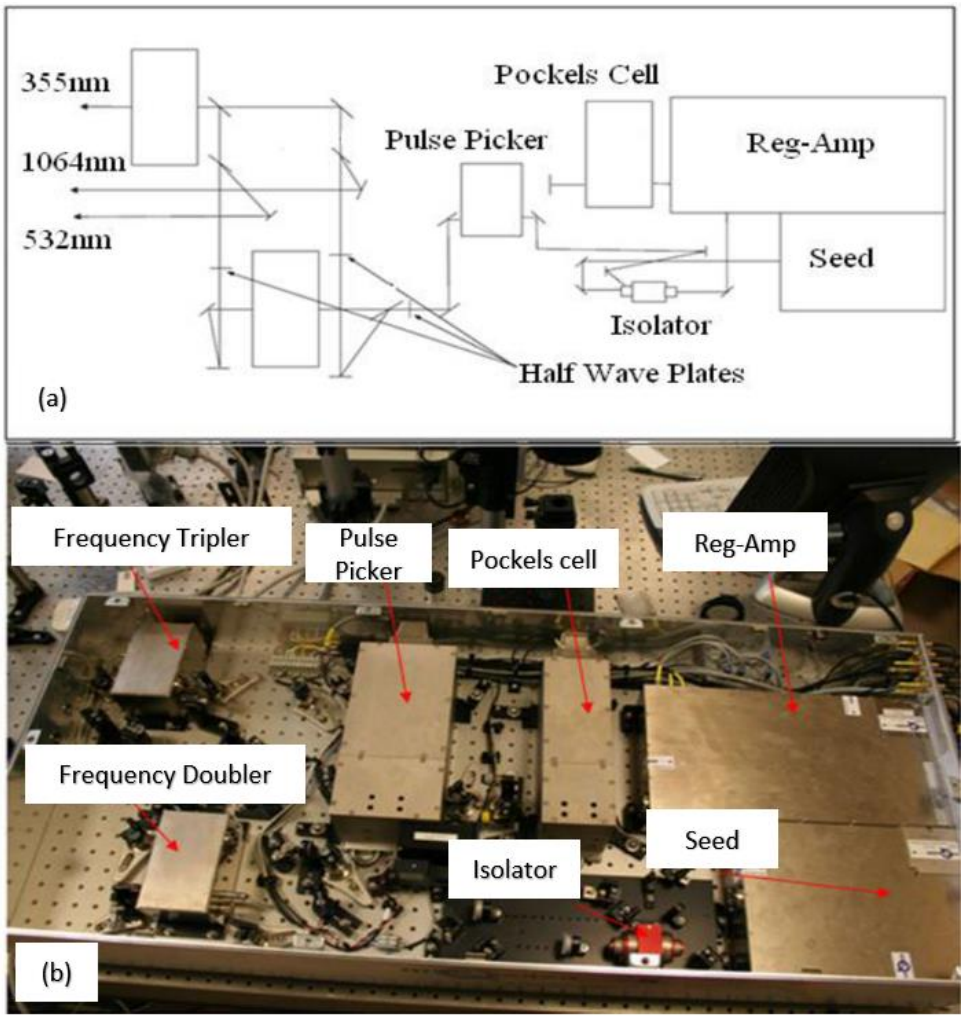

Figure 3.4 (a) Schematic of optical setup inside High-Q laser head and (b) the corresponding image of laser head internals

Figure 3.4 shows the schematic of the laser head. The mode-locked seed oscillator initially generates 10ps pulses at MHz level repetition rate with diode pumping. Then the pulse train enters the regenerative amplifier through a Faraday isolator. Only certain pulses are trapped by pulse picker and amplified with HV pulses applied to the Pockel's cell. The fundamental output wavelength of 1064nm can be frequency-

doubled and tripled by adjusting the relevant half wave plates, generating 532nm and 355nm output, respectively. Figure 3.5 shows the 1064nm output measured using Thorlabs BC106 beam profiler, which was found to be approximately Gaussian distribution.

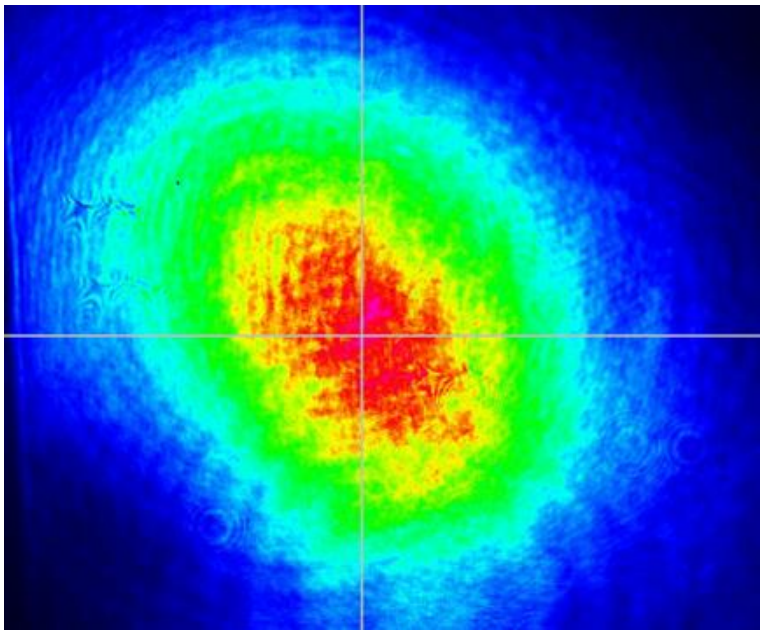

Figure 3.5 Original beam profile of High Q laser measured using a CCD camera

Figure 3.6 shows the interface of the control software, through which most of the common laser operations can be easily done by mouse clicks, e.g. switching the pulse repetition rate (by controlling the TTL signal), varying the output (by tuning the internal attenuator) and so on.

3.2 Spatial light modulators

Two different types of reflected SLMs were employed in this research, a Holoeye LC-R 2500 and a Hamamastu X10468-03.

3.2.1 Holoeye LC-R 2500

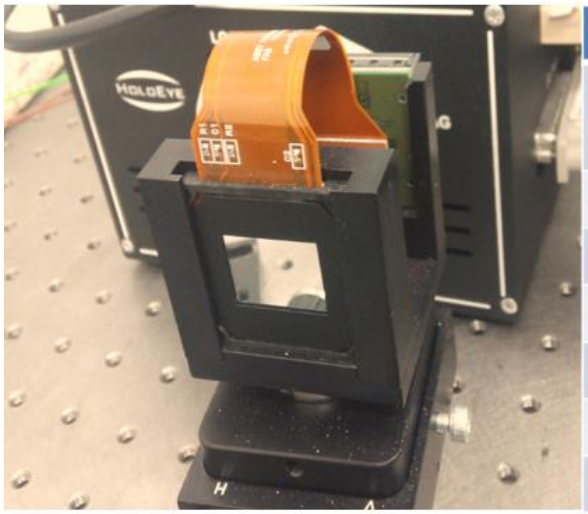

Model	Holoeye LC-R2500
LC Type	45 degree twisted nematic Phase and amplitude
Resolution	XGA (1064×768)
Pixel pitch(μm)	19
Effective area(mm^2)	19.5×14.6
Mirror coating	Board band metallic
Reflectivity	≈75%
Frame rate(Hz)	72

Figure 3.6 Holoeye LC-R 2500 and its specifications

As show in Figure 3.6, the Holoeye LC-R2500 is an electrically addressed reflective SLM (ER-SLM), based on a pixelated liquid crystal on silicon (LCoS) microdisplay supporting digital visual interface (DVI) signals with extended graphic array (XGA) resolution (1024×768 pixels). With broad band metallic coating, the maximum reflectivity of LC-R2500 have been measured to be 75%, when inputting the laser pulses from the Fianium laser with 20ps pulse duration and 1064nm wavelength at infrared region. The LC-R 2500 has a 45 degree twisted nematic LC layer whose molecules are arranged in

a twisted array from the front to the back of the device [112], the output properties of which will be introduced in the following sections.

3.2.2 Holoeye LC-R 2500 output test

3.2.2.1 Introduction

The beam shaping techniques presented in this research are an image-based process, in which the outline profile and intensity distribution of a laser beam is reconstructed onto metal surfaces. Thus, the precise controlling of the output intensity is essential in this research. In this section, the principle and practice of intensity modification of a Holoeye LC-R 2500 will be discussed.

3.2.2.2 Experimental setup

The Holoeye LC-R 2500 has a 45 degree twisted nematic LC layer whose molecules are arranged in a twisted array from the back of the device [112]. To have a better understanding of the principle and intensity modification ability, an experiment was carried out as in Figure 3.7.

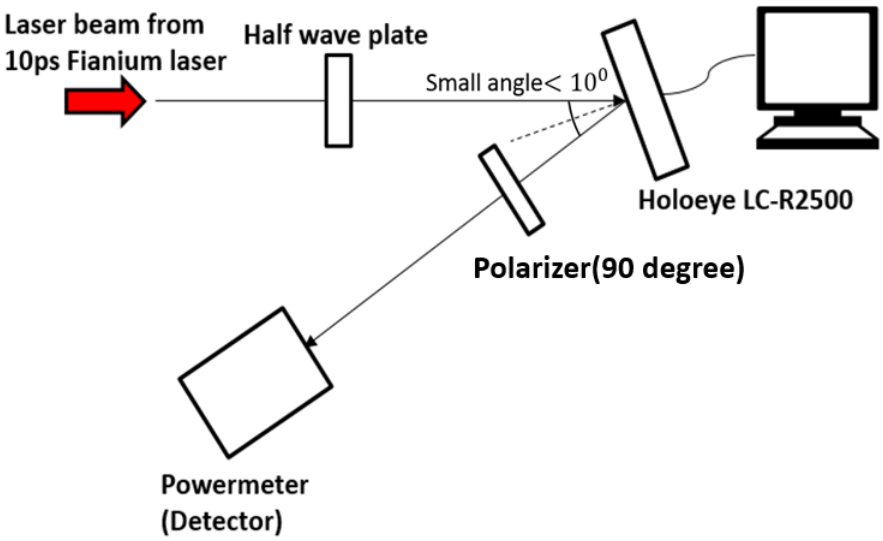

Figure 3.7 Experimental setup for Holoeye LC-R 2500 output test

As shown in Figure 3.7, a laser beam output (beam diameter: Dia.≈0.8, pulse duration: *tp*=20ps, wavelength: λ=1064nm, and repetition: *f*=200kHz) from the picosecond fiber laser system (Fianium) passes through a half-wave plate used for adjusting the polarization direction and illuminates the Holoeye LC-R 2500 SLM. The reflected beam passes a polarizer where the fast axis is 90 degrees and then reaches a power meter.

3.2.2.3 Results and discussion

The polarization angle was changed from 10° to 90° by rotating the half wave plate, and the gray level on SLM was changed from 0 to 255 on each incident angle. The results of measured output was shown in Figure 3.8.

On each incident angle, the output intensity was different while changing the gray level on the SLM. When the incident angle was 50° and 60°, the trendline of the output was

approximately linear to gray level changes and a curve when using other incident angles. In Figure 3.9 there is no obvious regularity in the relationship. However, all of their trendlines can be approximately fitted into a part of a cosine or sine function and the phase difference between gray level 0 and 255 was about 90°. As we know, when a linear polarized beam passed a polarizer where the fast axis was set as 0°, the output intensity is:

$$I_{out} = I_{in} \times \sin^2(\theta - 0)$$

$$I_{out} = \frac{1}{2} \times [I_{in} \times (1 - cos2\theta)] \quad (3.1)$$

Where I_{out} is the laser output intensity after the polarizer, I_{in} is the laser input intensity and θ is the polarised angle of the incident beam.

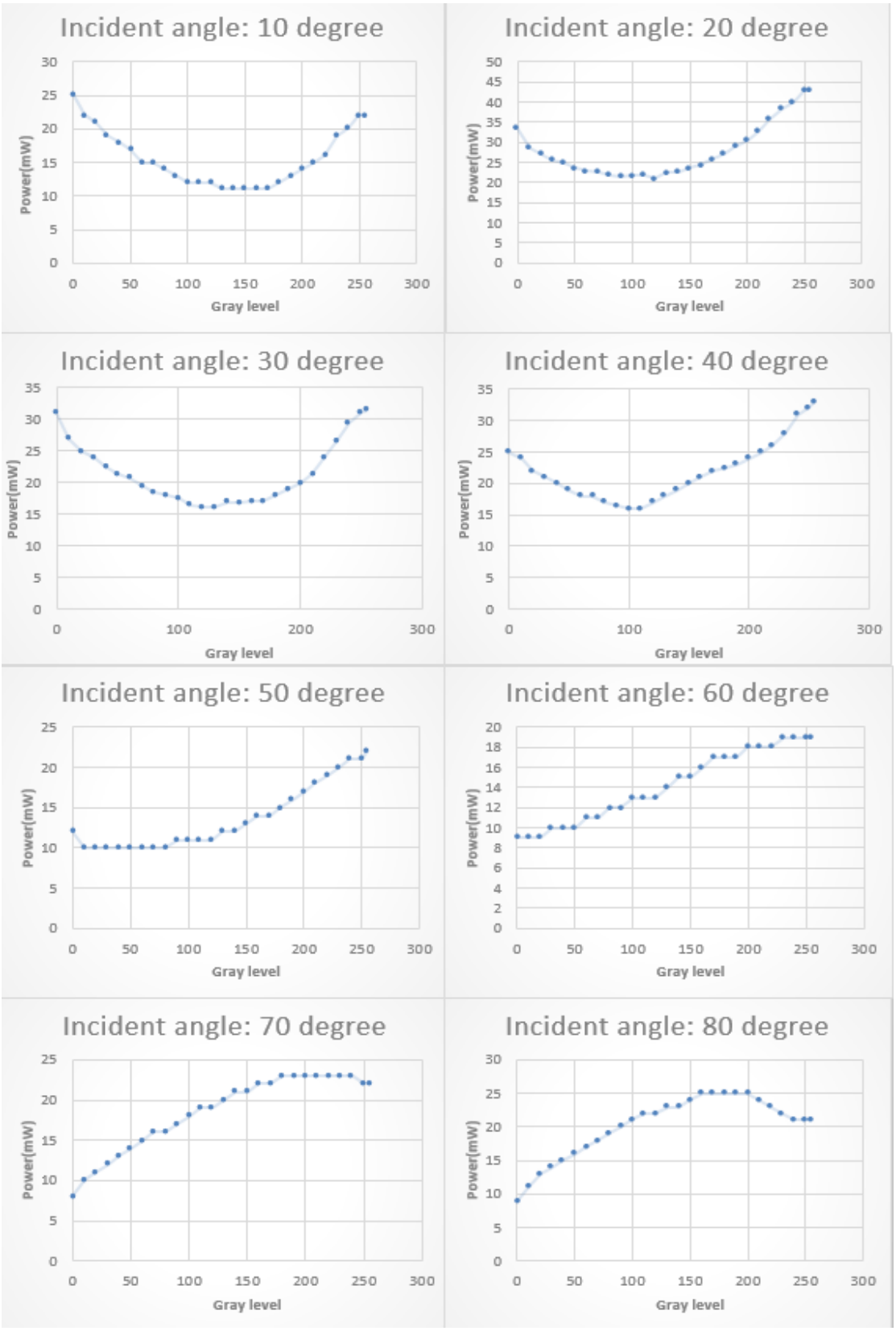

Figure 3.8 Output intensity while changing the incident angle and gray level on SLM

As shown in equation 3.1, the output is also a cosine function. If we assume that when the gray level changes from 0 to 255, the polarized angle of reflected beam changes by θ, then the output intensity will be twice the incident angle which is 2θ. In this case, we can tell from Figure 3.9 that $2\theta \approx 90^{\mathrm{o}}$, and then θ can be calculated to be $\theta \approx 45^{\mathrm{o}}$, which means for Holoeye LC-R2500, when the gray level changed from 0 to 255, the reflected angle is changed by 45° from the incident beam, regardless of the incident angle.

To verify this conclusion, another experiment was carried out. The experimental setup was the same, however, this time the incident polariser angle was set to be 90° and the gray level was changed from 0 to 255, the polarizer was then rotated to reach the minimum output. The minimum output and fast axis angle of the polarizer for each gray level was recorded in Figure 3.9.

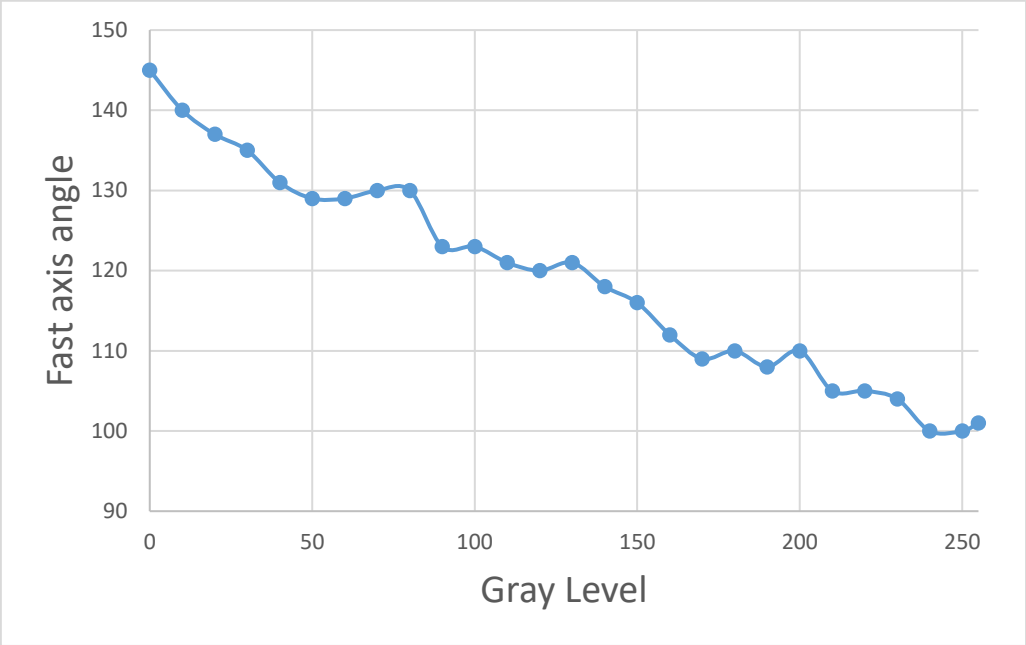

Figure 3.9 Gray level and corresponded fast axis angle when output is minimum

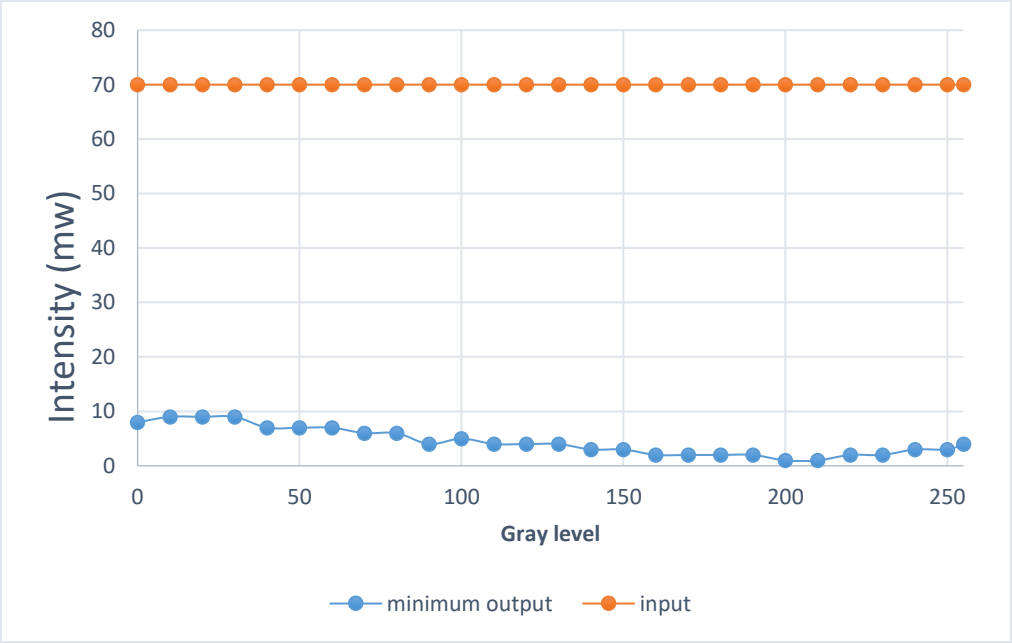

Figure 3.6 Gray level and corresponded minimum output

As shown in Figure 3.9, when the gray level was 0, the fast axis of the polarizer was set at 145° to obtain minimum output, and when the gray level was 255, the angle of fast

axis was 100°. It can be easily calculated that there is a 45° polarization difference in the reflected beam between gray level 0 and 255. Figure 3.10 showed the comparison between input and minimum output on each gray level. The laser input intensity was set at 70mw, and the minimum output varied from 1mw to 9mw which is very small compared to the input power. Therefore, it can be concluded that the polarization direction changed by 45° when the gray level changed from 0 to 255, regardless of the incident angle.

3.2.2.4 Conclusion

In the first part of this test, the incident angle and gray level was changed to find out the relationship between gray level and the output. It showed that all the trendlines can be approximately fitted into a part of a sine or cosine function and the phase difference from gray level 0 to 255 was approximately 90°, which indicated the polarization direction changed by 45°.

In the second part, the analyzer was rotated to reach the minimum output on each gray level. When the gray level changed from 0 to 255, the angle of analyzer changed by 45°, which further verified that the polarization direction has change by 45°.

3.2.3 Hamamastu X10468-03

Model	Hamamatsu X10468-03/04
LC Type	Parallel-aligned nematic Phase only
Resolution	SVGA(800 ×600)
Pixel pitch(μm)	20
Effective area(mm^2)	16×12
Mirror coating	Dielectric
Reflectivity	>90%
Frame rate(Hz)	60

Figure 3.7 Hamamastu X10468-03 and its specifications

The second SLM used in this research was a Hamamastu X10468-03 which is based on a pixelated liquid crystal device with SVGA resolution (800×600 pixels). In this case, this device has a dielectric coated mirror, providing >90% measured reflectivity for input laser beams with a specified wavelength (1064nm), for the high-Q picosecond laser system.

A difference compared to the LC-R 2500 is the characteristics of the liquid crystal (LC). As discussed in section 3.2.1, the LC-R 2500 has a 45 degree twisted nematic LC layer whose molecules are arranged in a twisted array from the front to the back of the device. In contrast, the X10468-03 has a parallel aligned nematic crystal, in which the LC molecules are aligned horizontally along the optical axis, hence causing a phase

change to the light polarised along the molecule axis, but leaving the light polarisation perpendicular to the molecular axis completely unaffected.

3.2.4 Hamamastu X10468-03 output test

3.2.4.1 Experimental setup and theoretical calculation

The Hamastu X10468-03 has a parallel aligned nematic crystal layer, which changes the polarisation along the molecule axis and leaving the light polarisation perpendicular to the molecular axis unchanged. To better understand the principle and properties of the X 10468-03, an experiment was carried out as in Figure 3.12.

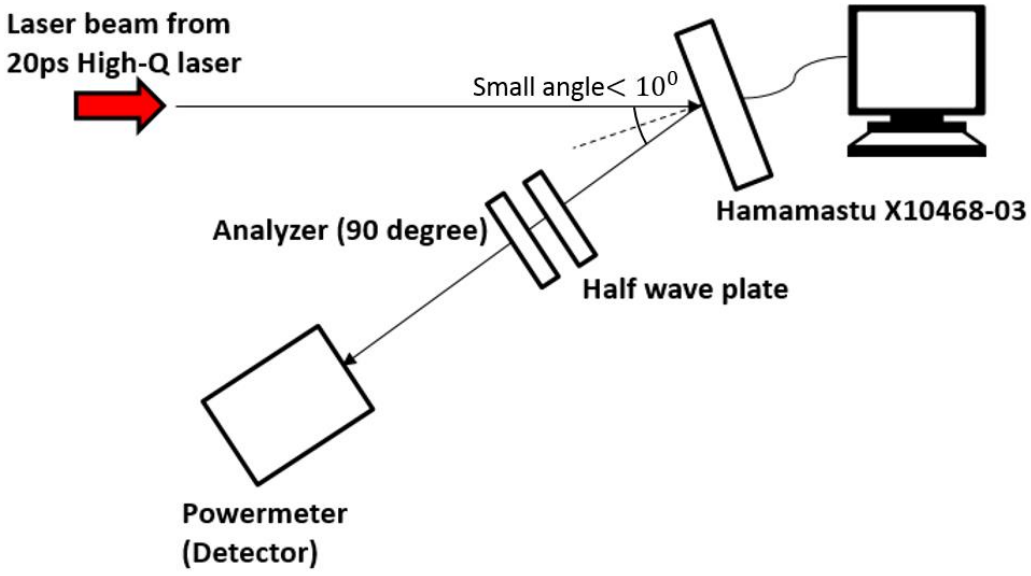

Figure 3.8 Experimental setup for Hamamastu X10468-03 output test

Due to the properties of changing polarisation of the incident beam in one direction,

the SLM can be described using a Jones matrices as $\begin{pmatrix} e^{i\times\emptyset(x,y)} & 0 \\ 0 & 1 \end{pmatrix}$, where $e^{i\times\emptyset(x,y)}$ is the phase delay of incident beam in horizontal and vertical direction. When all elements are described using Jones matrices, the theoretical intensity output can be derived as in Figure 3.13.

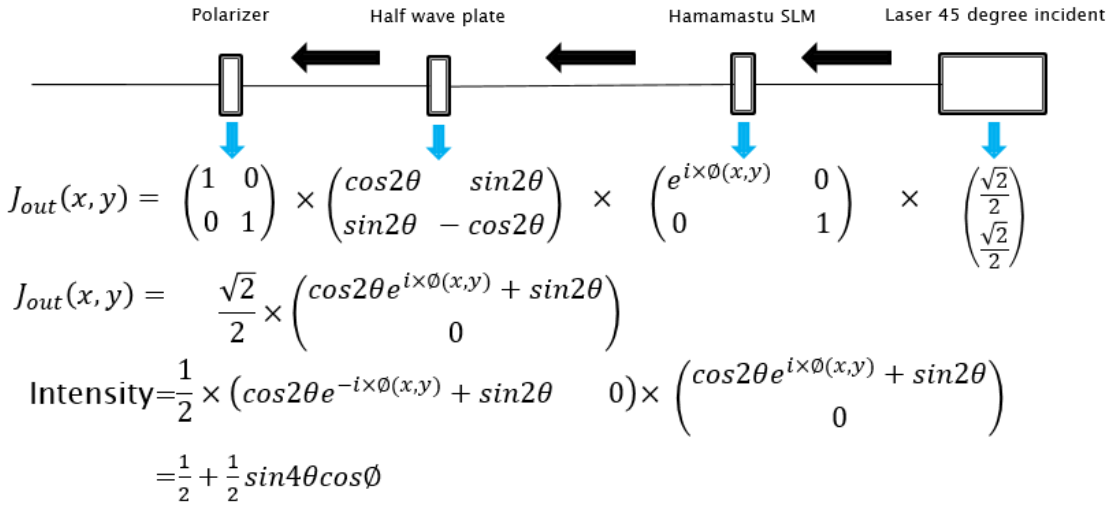

Figure 3.9 Output calculation

In Figure 3.14, the Jones matrices of each element was written under its block and the output intensity can be calculated to be $\frac{1}{2} + \frac{1}{2} sin4\theta cos\emptyset$, in which θ is the fast axis angle of half wave plate and $\emptyset$ is the phase modulation of SLM. When θ is set to be $\theta = -\frac{1}{8}\pi$, the output intensity is $\frac{1}{2} - \frac{1}{2} cos\emptyset$, which means if the phase delay can be adjusted from 0 to $\frac{\pi}{2}$, the output intensity can be adjusted from 0 to as much as the input.

3.2.4.2 Output test results and discussions

In this experiment, the fast axis angle of half wave plate was changed from $-\frac{\pi}{8}$ to $\frac{1}{8}\pi$, and at each fast axis angle, the gray level was changed from 0 to 255 to modulate phase delay. The results are shown in Figure 3.14.

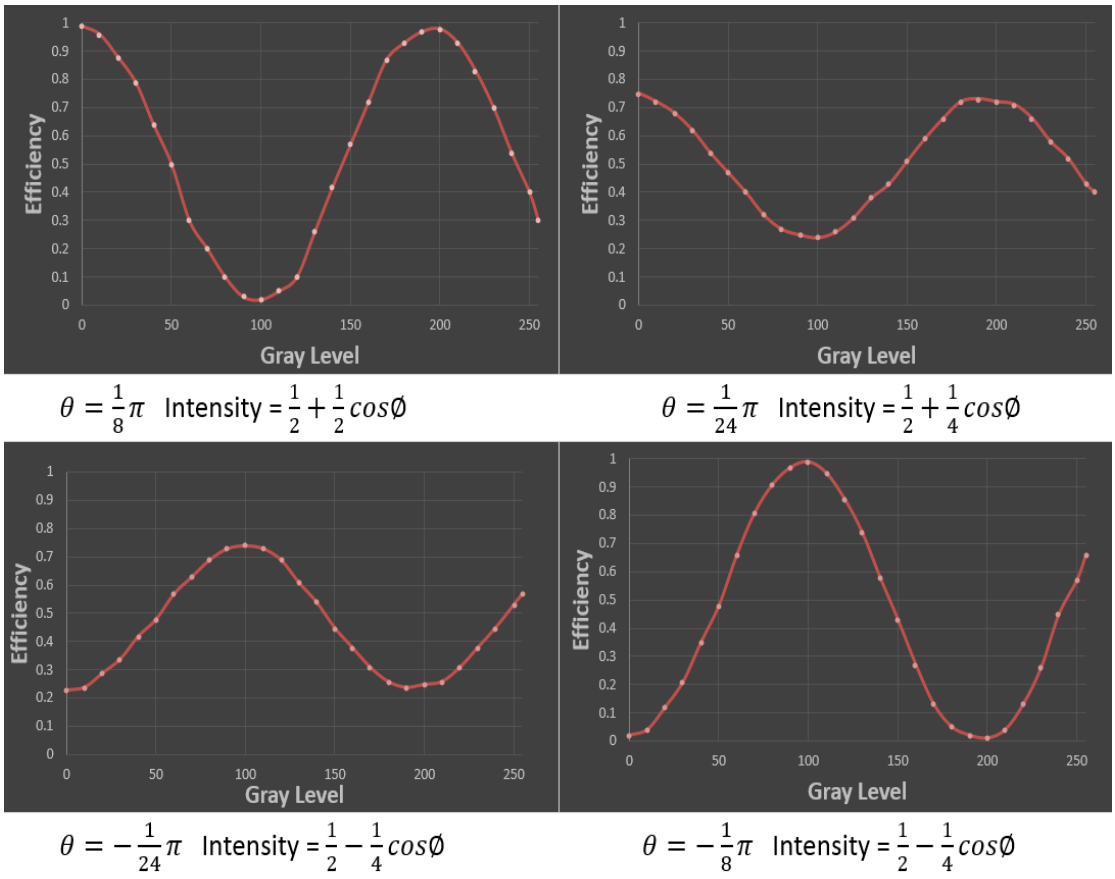

Figure 3.10 Output intensity vs Gray level at different half wave plate fast axis angle

The efficiency is the ratio of the output and input measured power. As shown in Figure 3.15, when changing gray level on the SLM, the phase delay changed accordingly. The

trendline of efficiency at all fast axis angles can be fitted into a cosine function with different phase, which matches the equation below each image. The phase modulation range from gray level 0 to 255 was approximately $\frac{5}{4}\pi$ according to the trend lines. When the fast axis angle of half wave plate was $\frac{\pi}{8}$ and $-\frac{\pi}{8}$, the modulation ability reached the maximum from 0 to 1, while in other conditions, the efficiency cannot reach 0 or 1.

3.2.4.3 Output test conclusions

The X10468-03 is a parallel aligning nematic crystal device, causing a phase change to the light polarised along the molecular axis and leaving the perpendicular direction completely unaffected. In this experiment, the working principle and modulation ability of X10468-03 has been studied. As in the calculation, if the phase delay can be changed from 0 to $\frac{\pi}{2}$, the intensity can be changed from 0 to maximum. The experimental results showed that the phase can be modulated approximately from 0 to $\frac{5}{4}\pi$ which is larger than $\frac{\pi}{2}$, therefore, when the fast axis angle of a half wave plate was $\frac{\pi}{8}$ and $-\frac{\pi}{8}$, the modulation ability reaches a maximum. Due to the different working principle compared to the Holoeye LC-R 2500, the intensity modulation ability of the X10468-03 was much higher, which can lead to a better result in terms of beam shaping.

3.3 Scanning Galvanometer and multi-axis motion control system

3.3.1 Scanning galvanometer systems

A Nutfield XLR8 galvanometer scanning head has been employed in this experimental work. This was used to scan the laser beam on a test sample. The module consists of 2 galvanometer scanners (X and Y), two mirrors, two servo-amplifiers, and communication electronics. Scanning galvanometer systems enables high speed (up to 10m/s) and high precision (μm level) control of ultrafast laser beam position on a large sample surface. The schematic configuration of a scanning galvanometer is shown in Figure 3.15.

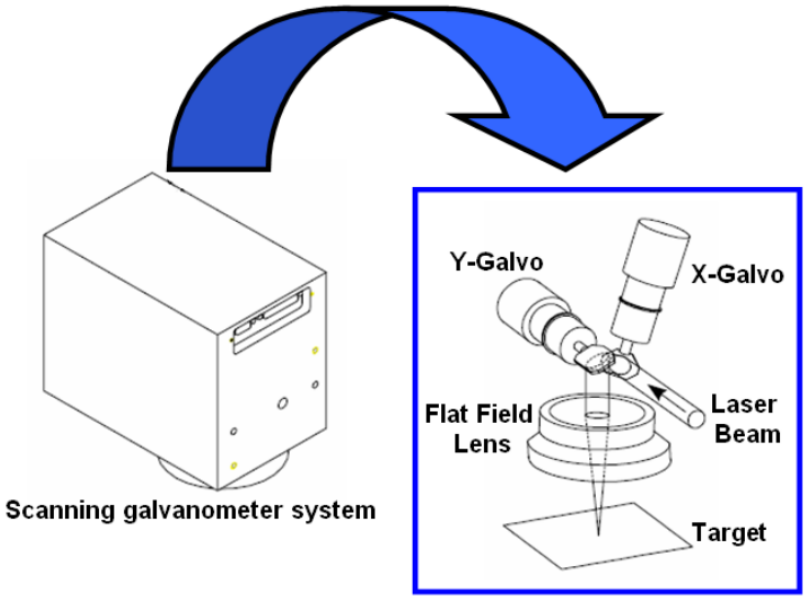

Figure 3.11 Schematic diagram of a scanning galvanometer system

Two dielectric mirrors attached on the galvanometers enable the deflecting optical beam move in a range of 60mm × 60mm. The synchronized actions of the two galvanometer servo-controlled turning mirrors directs the laser beam the specific locations on the target material. Since the laser beam is always perpendicular to the substrate top surface, the scanning field is flat without edge effects.

3.3.2 Motion control systems

Two Aerotech multi-axis motion control systems as shown in Figure 3.16 were used in this research. A three-axis motion control system (x,y,z) with an Aerotech A3200 controller has been employed in Fianium FemtoPower laser system (see Figure 3.17(A)) [113]. A3200 uses Motion Composer to create motion trajectories. The movement of all three axis can be programmed in native RS-274 G-code, Matlab or Labview. The operation interface is shown in Figure 3.17.

A five-axis motion control system (x,y,z,u,a) was used with the HighQ picosecond laser system (See Figure 3.16(B)). The X-axis and Y-axis use Aerotech ATS 150 controller. The Z-axies is an Aerotech AVS/AVSI100 Mechanical-bearing ball-screw left stage, which is capable of 13mm travel distance and $\pm 3.0\mu m$ accuracy [114]. The two tilting stage axis are Aerotech ANT-20G Goniometers, both features 20 degrees rotation angle [115].

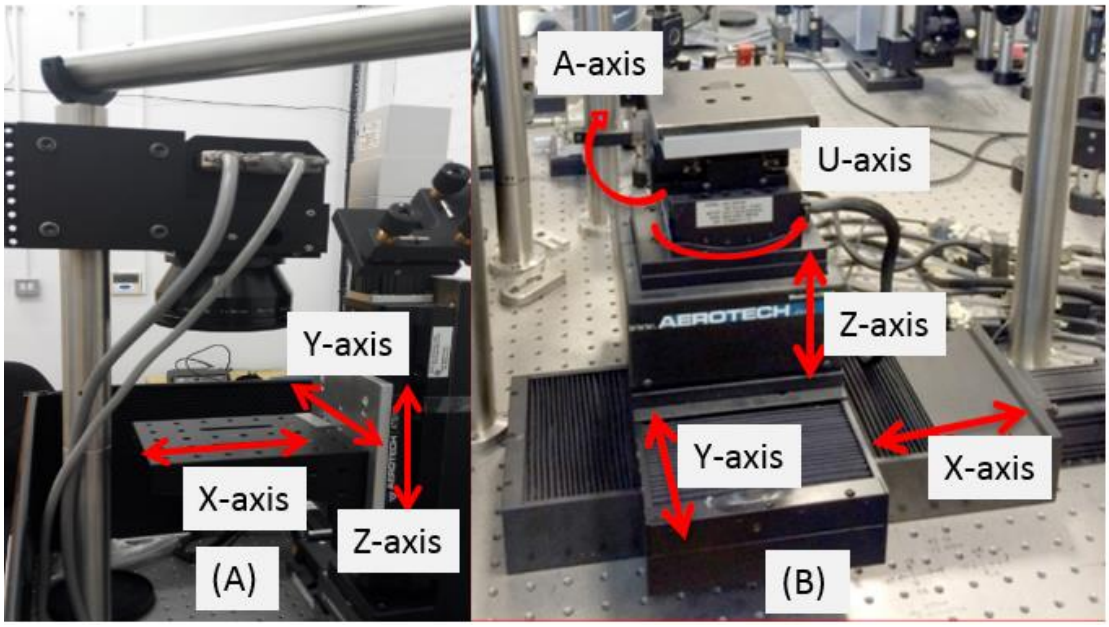

Figure 3.12 (A) 3-axis motion system for Fianium picosecond laser, (B) 5-axis motion system in HighQ picosecond laser system

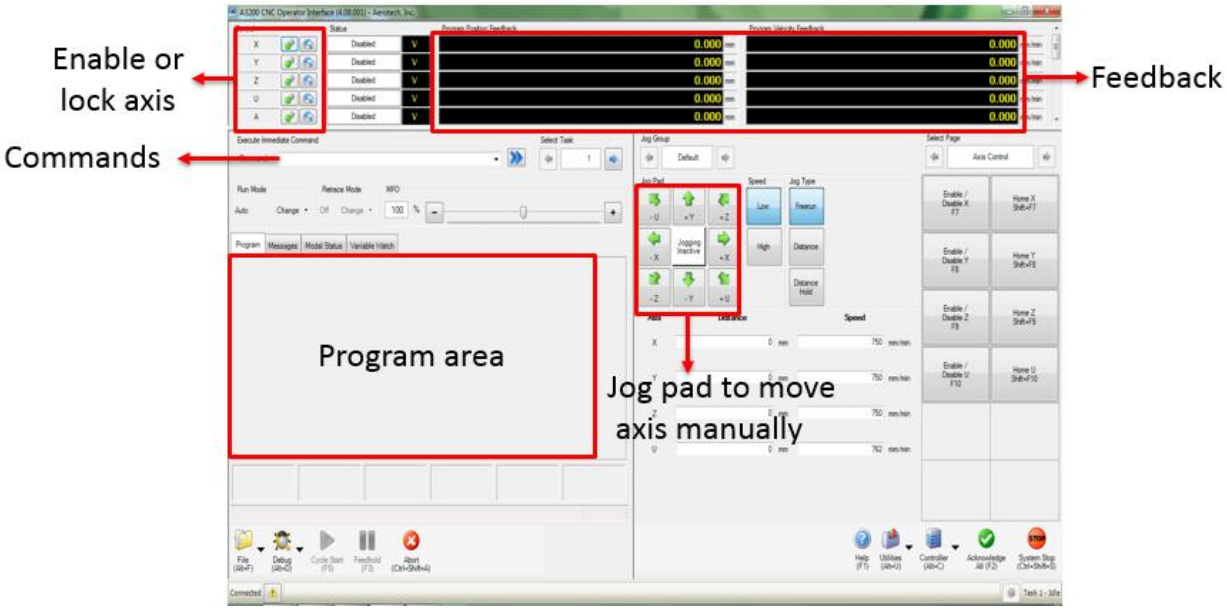

Figure 3.13 A3200 CNC Operator Interface

3.4 Beam profilers

Two different beam profilers were employed in this research, a Thorlabs BC106-VIS and Spiricon Model SP620U.

3.4.1 Thorlabs BC106-VIS

As shown in Figure 3.18, the Thorlabs BC106-VIS consists of the following equipment: an optical senor with a working range of 350-1100nm; a filter wheel with four absorptive neutral density (ND) filters (10dB, 20dB, 30dB and 40dB); a Mini B USB connector and a TTL Trigger input; a BC1M2 Extension mounted at the bottom of the profiler [116]. It provides all the essential features needed for laser beam analysis (see Figure 3.19). 2D and 3D beam profile can be displayed together at a high resolution. Important parameters of a beam profile such as intensity, beam diameter and peak density can be monitored at a high speed. The detector area is $8.8\mathrm{mm} \times 6.6\mathrm{mm}$ with a pixel spacing of $6.45\mu\mathrm{m} \times 6.45\mu\mathrm{m}$.

Additionally, a BC1M2 extension is mounted at the bottom for M^2 measurement. During the measurement, the profiler moved step by step along the propagation axis of a focussed beam and beam diameter is measured at each position in order to find the beam waist.

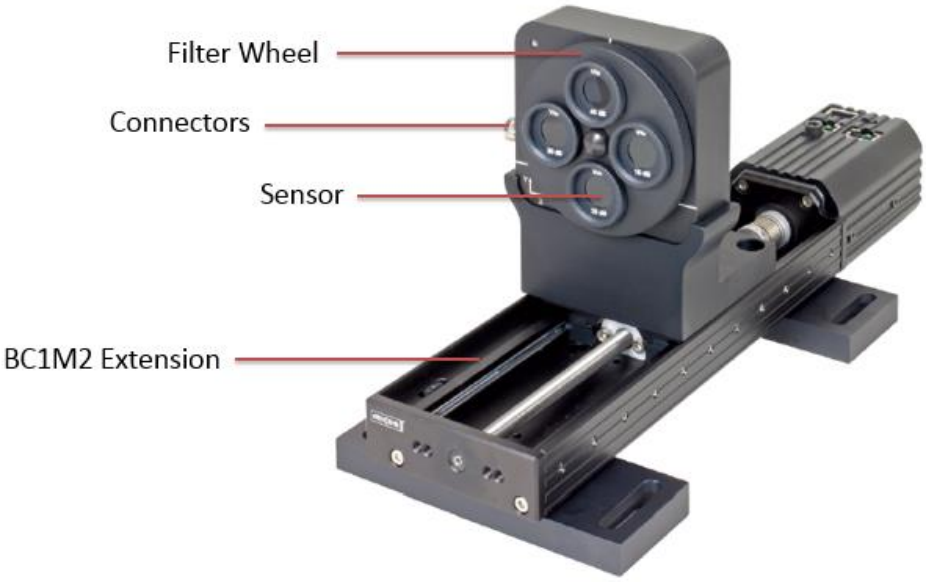

Figure 3.14 Picture of a Thorlabs BC106-VIS beam profiler

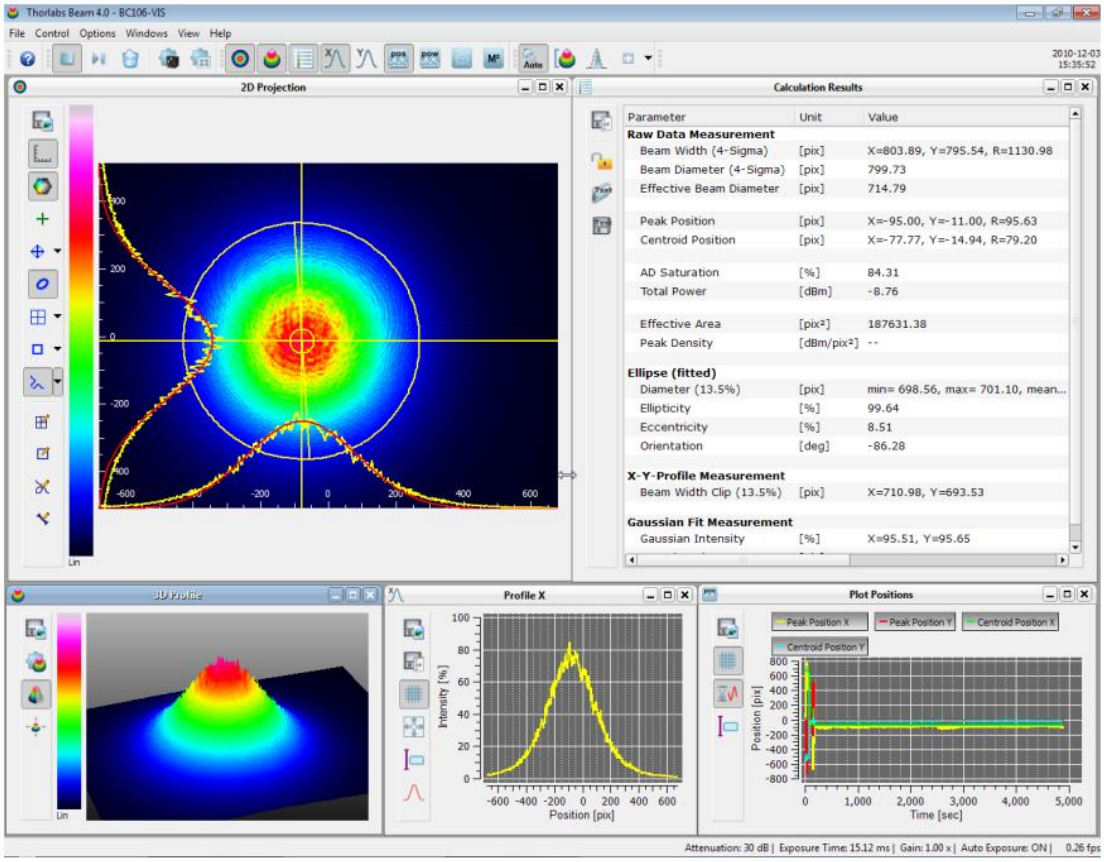

Figure 3.19 Operation interface of Thorlabs BC106-VIS

3.4.2 Spiricon SP620U

The second beam profiler employed in this experiment is a Spiricon SP620U [117], as shown in Figure 3.20 (A). This beam profiler system consists of a Spiricon frame grabber card with software and a CCD camera. A wedged fused silica plate placed before the CCD chip near the Brewsters angle allows a small portion of laser beam to reflected onto the sensitive CCD detector. Therefore, only s-polarized beam will be reflected to the CCD chip and the rest of the beam transmitted. 2D and 3D beam profile can be displayed with high speed and high resolution, as shown in Figure 3.20(b). The detector area is $8\text{mm} \times 6\text{mm}$ with a pixel spacing of $9.9\mu\text{m} \times 9.9\mu\text{m}$.

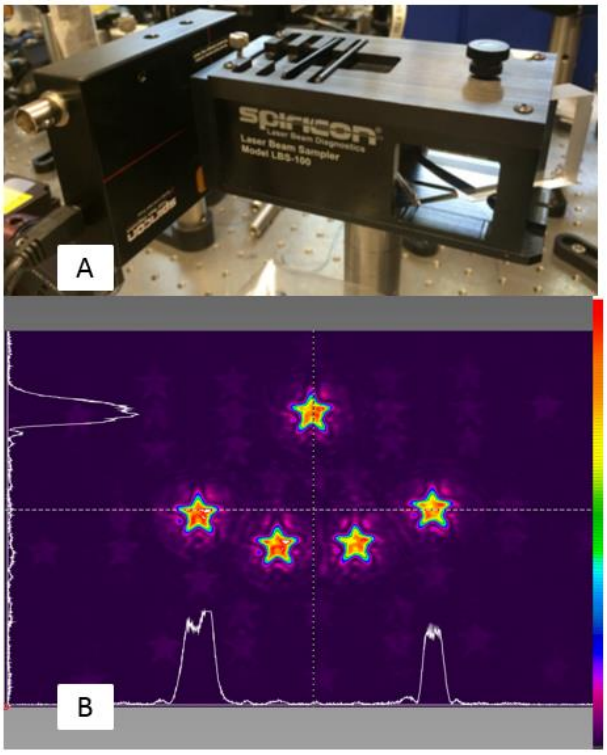

Figure 3.15 (A) Spiricon laser camera used in this research and (B) 2D profile measurement interface

3.5 Analysis equipment for machined samples

3.5.1 Nikon Digital Microscope

The Nikon microscope provides 2D images of the surface condition after the laser treatment. The microscope has several available magnifications to allow detailed inspection of processed surface: x4, x10, x20, x40 and x100. The Nikon digital microscope consists of an optical microscope, a digital camera, and a software running in Windows environment for operating the digital Camera. A 3-axis stage was integrated with the optical microscope for placing the sample and finding the focal plane of the microscope.

3.5.2 WYKO NT1100 white light microscope

A WYKO NT1100 interferometric microscope was employed to achieve the surface topography in three dimensions. It is a non-contact optical profiler which provides the XY plane with 0.5 micron level resolution and Z resolution of a few nanometers. During the measurement, a white light illumination source split into two beams, with one beam impinged on the sample surface and reflected back to interfere with the reference beam generating fringe patterns, giving the 3D profile of the sample surface. This microscope connect with an advanced computer software, which offers an analysis package, allows dissection and formatting the measured surface data (see

Figure 3.21).

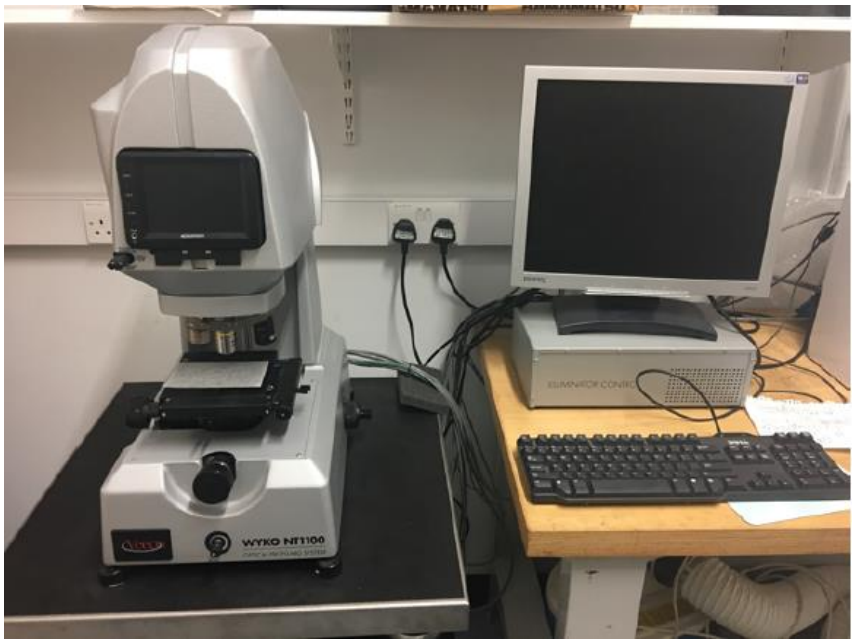

Figure 3.16 WYKO NT1100 interferometric microscope

Chapter 4 Beam shaping at imaging plane using binary masks

4.1 Introduction

This chapter presents the results of Fianium picosecond laser ($\tau_p \approx 20ps, \lambda = 1064\text{nm}$ and f=0.2MHz) beam shaping for material processing at the imaging plane by binary masks using a Holoeye LC-R2500 SLM.

The methodology of processing at the image plane will be firstly demonstrated in section 4.2, where the difference between processing at focus and image plane will be discussed. The specific experimental setup will be explained in 4.3, in which a long beam path has been created.

Section 4.4 presents the results and discussion about shaping quality and efficiency. In which the size of the mask, the processing position and the shapes of a mask are discussed.

4.2 Beam shaping at the focal plane and imaging plane

4.2.1 Beam shaping at the focal plane

In many methods for beam shaping such as using beam splitting gratings, diffractive diffusers and some geometrical optics devices, the laser beam is directly focused onto the material surface due the highest efficiency and diffractive accuracy. Recently, spatial light modulator technology has gained popularity due to the flexibility and efficiency. A brief introduction of creating a required pattern at the focal plane using

computer generated holograms (CGH) is shown in Figure 4.1.

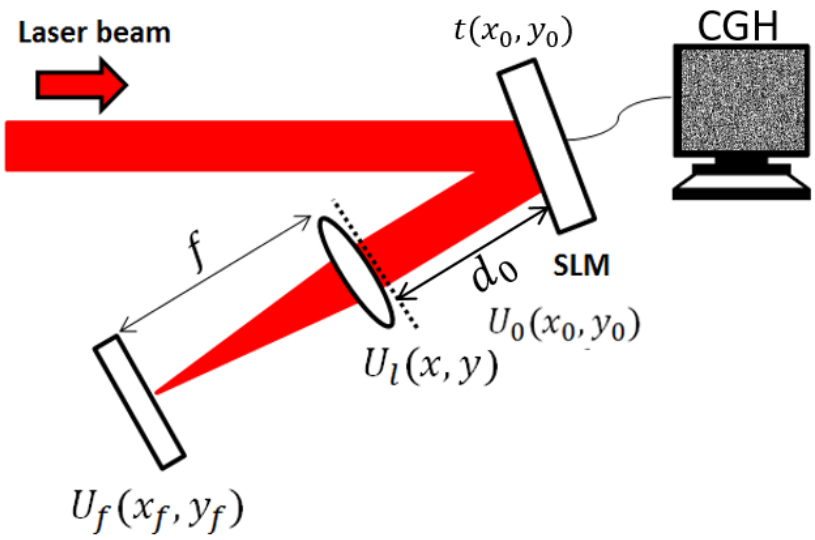

Figure 4.1 Schematic of processing at the focal plane

As shown in Figure 4.1, a laser beam is illuminated onto a SLM with a CGH applied on it, and the reflected beam is passed through a thin focusing lens onto the surface of a sample in the focal plane. In Figure 4.1, t is the complex amplitude transmittance function of the CGH, U_0 is the complex amplitude just after the SLM and U_f is the complex amplitude at the focal plane. A calculation of the modulation can be made based on Fourier optics [53].

Firstly the light field at U_0 can be described as:

$$U_0(x_0, y_0) = At(x_0, y_0) \tag{4-1}$$

where A is the amplitude of laser beam. The frequency spectrum before the lens can be derived as：

$$\mathcal{F}\{U_l(x,y)\} = \mathcal{F}\{U_0(x_0,y_0)\} \times H(f_x,f_y) \quad (4\text{-}2)$$

where $H(f_x,f_y)$ is the optical transfer function in the frequency spectrum, $\mathcal{F}$ represents Fourier transformation, and $H(f_x,f_y)$ can be expressed as:

$$H(f_x,f_y) = \exp[-i\pi\lambda d_0(f_x^2+f_y^2)] \quad (4\text{-}3)$$

And the frequency spectrum after the SLM can be expressed as:

$$\mathcal{F}\{U_0(x_0,y_0)\} = A\,\mathcal{F}\{t(x_0,y_0)\} = A \times T(f_x,f_y) \quad (4\text{-}4)$$

Combining equations (4-3) and (4-4), we can derive that:

$$\mathcal{F}\{U_l(x,y)\} = AT(f_x,f_y)\exp[-i\pi\lambda d_0(f_x^2+f_y^2)] \quad (4\text{-}5)$$

The phase modulation of a lens can be expressed as:

$$t_l(x,y) = \exp[-\mathrm{i}\frac{k}{2f}(x^2+y^2)] \quad (4\text{-}6)$$

The complex amplitude at the focal plane U_f can be calculated as:

$$U_f(x_f,y_f) = \frac{A}{i\lambda f}\exp[i\frac{k}{2f}(x_f^2+y_f^2)] \times \mathcal{F}\{U_l(x,y)\} \quad (4\text{-}7)$$

Combining equations (4-5) and (4-7), we can derive that:

$$U_f(x_f, y_f) = \frac{A}{i\lambda f}\exp[i\frac{k}{2f}(1-\frac{d_0}{f})(x_f^2+y_f^2)] \times T(\frac{x_f}{\lambda f}, \frac{y_f}{\lambda f}) \quad (4\text{-}8)$$

where T is the Fourier transformation of t. We can see that from equation (4-8), the complex amplitude at the focal plane is proportional to the Fourier transformation of the object, but with a distortion in its phase. Additionally, if the distance between the CGH and the lens is very small and d_0=0, the light field distribution becomes the exact Fourier transformation of the object.

4.2.2 Beam shaping at the imaging plane

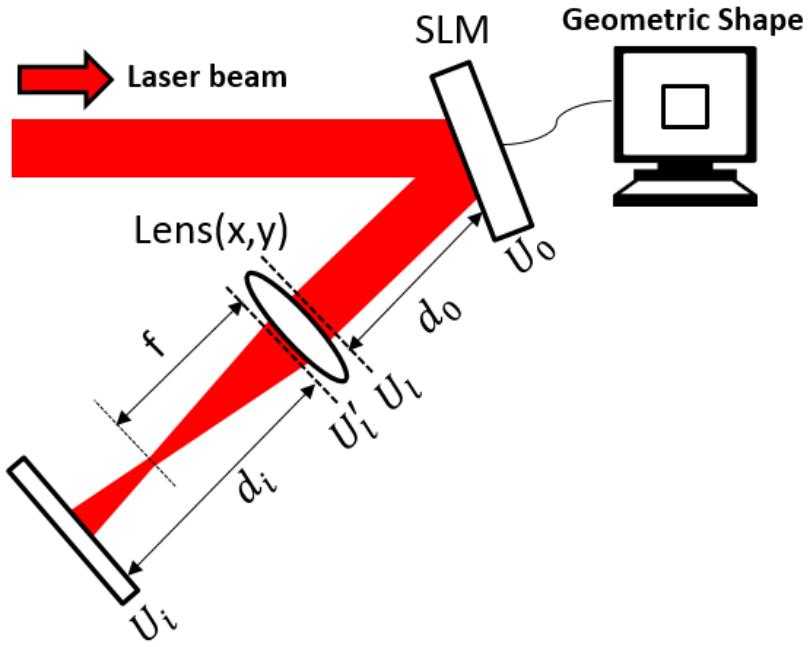

Figure 4.2 Schematic of processing at the imaging plane

Figure 4.2 shows a schematic of laser processing at the imaging plane. A laser beam is illuminated onto a SLM and a binary geometric figure is applied. The SLM in this case

is used as an intensity modulator. It is worth noting that a polarizing filter is also required here but is ignored to simplify explanation. The reflected beam passes through a thin focus lens and to a sample at imaging plane. In Figure 4.2, U_0 is the complex amplitude of the laser at the objective plane, U_l and U_l' refers to the complex amplitude before and after the lens, and U_i is the electric field diffraction pattern at the image plane.

Using the Fresnel diffraction integral, the complex amplitude at U_l can be described as [53]:

$$U_l(x,y) = \frac{1}{i\lambda d_0}\exp(ikd_0)\exp[i\frac{k}{2d_0}(x^2+y^2)] \times \iint_{-\infty}^{\infty} U_0(x_0,y_0) \times \exp\left[j\frac{k}{2d_0}(x_0^2+y_0^2)\right]\exp[-i\frac{2\pi}{\lambda d_0}(x_0x+y_0y)]dx_0dy_0 \quad (4\text{-}9)$$

In Fourier Optics, a complex amplitude of a lens t_l can be expressed as:

$$t_l(x,y) = P(x,y)\exp[-i\frac{k}{2f}(x^2+y^2)] \quad (4\text{-}10)$$

Where $P(x,y)$ is the pupil function of the lens. Since the laser beam diameter is much smaller than the size of the lens in this experiment, $P(x,y)$ can be approximately regarded as 1.

The complex amplitude after the lens at U_l' can be express as:

$$U_l' = U_l(x,y)t_l(x,y) \quad (4\text{-}11)$$

After the laser beam passes d_i and reaches U_i, the electric field diffraction pattern can be calculated using the Fresnel diffraction integral as:

$$U_i(x_i, y_i) = \frac{1}{i\lambda d_0}\exp(ikd_i)\exp[i\frac{k}{2d_i}(x_i^2 + y_i^2)] \times \iint_{-\infty}^{\infty} U_l'(x, y) \times \exp\left[j\frac{k}{2d_0}(x^2 + y^2)\right]\exp[-i\frac{2\pi}{\lambda d_i}(x_i x + y_i y)]dxdy \quad (4\text{-}12)$$

Combing equation (4-9) (4-10) and (4-11) into (4-12), we can derive that:

$$U_i(x_i, y_i) = \frac{1}{\lambda^2 d_0 d_i}\exp[i\frac{k}{2d_i}(x_i^2 + y_i^2)] \iint \iint_{-\infty}^{\infty} U_0(x_0, y_0) \times \exp\left[i\frac{k}{2}\left(\frac{1}{d_0} + \frac{1}{d_i} - \frac{1}{f}\right)(x^2 + y^2)\right]\exp\left[j\frac{k}{2d_0}(x_0^2 + y_0^2)\right] \times \exp\left[-i\frac{2\pi}{\lambda d_0}(x_0 x + y_0 y)\right] \times \exp[-i\frac{2\pi}{\lambda d_i}(x_i x + y_i y)]dxdy\, dx_0 dy_0 \quad (4\text{-}13)$$

This complex multiple integral needs to be simplified. It can be noted that the component $\exp[i\frac{k}{2d_i}(x_i^2 + y_i^2)]$ does not affect the final intensity distribution and can be neglected, since for each point on imaging plane, there should be a small relating area on the objective plane, and the phase difference is relatively small. Therefore, we can also assume that:

$$\exp\left[j\frac{k}{2d_0}(x_0^2 + y_0^2)\right] \approx \exp[i\frac{k}{2d_0}(\frac{x_i^2 + y_i^2}{M^2})] \quad (4\text{-}14)$$

where M=$\frac{d_i}{d_0}$ is the magnification factor. Thus, the factors of x_0 and y_0 can be simplified.

$$\frac{1}{d_0} + \frac{1}{d_i} - \frac{1}{f} = 0 \quad (4\text{-}15)$$

using the thin lens equation in Geometric optics. The simplified electric field diffraction

pattern U_i can be calculated as:

$$U_i(x_i, y_i) = \frac{1}{\lambda^2 d_0 d_i} \iint_{-\infty}^{\infty} \left\{ \iint_{-\infty}^{\infty} U_0(x_0, y_0) \exp\left[-i \frac{2\pi}{\lambda d_0}(x_0 x + y_0 y)\right] dx_0 dy_0 \right\} \times$$

$$\exp[-i \frac{2\pi}{\lambda d_i}(x_i x + y_i y)] \,\mathrm{dxdy}$$

$$= \frac{1}{\lambda^2 d_0 d_i} \iint_{-\infty}^{\infty} G_0 \times \exp[-i \frac{2\pi}{\lambda d_i}(x_i x + y_i y)] \, dxdy$$

$$= \frac{1}{M} U_0(-\frac{x_i}{M}, -\frac{y_i}{M}) \qquad (4\text{-}16)$$

Therefore, with a geometric shape applied on the SLM, the electric field pattern on the imaging plane can be approximately derived as $U_i(x_i, y_i) = \frac{1}{M} U_0(-\frac{x_i}{M}, -\frac{y_i}{M})$, which remains the exact shape but reversed.

The formation of diffractive patterns at both focal plane and imaging plane have been explained. For processing at the focal plane, the intensity distribution of diffractive patterns is proportional to the Fourier transformation of objects such as a CGH. When the distance between SLM and lens is smaller, the results gets more accurate. This is the foundation of many beam shaping methods based on parallel processing [49]. However, by using this method, complex CGHs need to be calculated and generated, it is a relatively time consuming procedure, only software with powerful calculation ability can complete this job.

For processing at the imaging plane, the pattern remains the same shape and intensity distribution as the object, which is much more flexible and Fourier transformations

can be avoided. However, the efficiency could be decreased significantly due to the much larger irradiance area at imaging plane. In addition, for phase only SLMs, some adjustment is needed for intensity modulation. To solve these two problems, a new experimental setup was devised.

4.3 Experimental setup

4.3.1 Overall setup

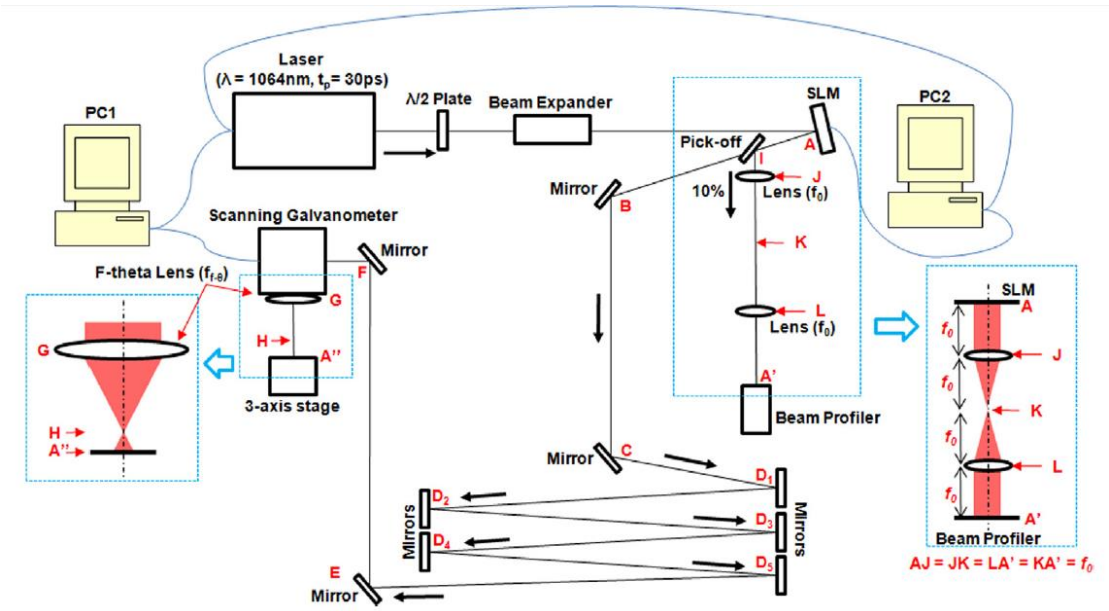

Figure 4.3 Experimental setup for image-based outline profile beam shaping

Figure 4.3 shows the schematic of the experimental setup for image-based beam shaping. A laser beam outputs (beam diameter: Dia.≈0.8, pulse duration: *tp*=20ps, wavelength: λ=1064nm, and repetition: *f*=200kHz) from a picosecond fiber laser system (Fianium) passes through a half-wave plate used for adjusting the polarization

direction, a beam expander (M≈×5), and illuminated on a reflective SLM (Holoeye LC-R 2500), oriented at <10^{o} angle of incidence. A pick-off (10%) beamsplitting mirror, placed after the SLM, reflected the beam through two positive lenses (focal length: f_0=200mm) formed 4f system to a CCD camera-based laser beam profiler (Thorlabs) to observe the reconstructed beam shape. After the SLM, the laser beam travelled a long distance by multiple reflections on a series of mirrors, passed through a scanning galvanometer and reached a focusing F-theta lens ($f_{f-\theta}$=100mm). Machining samples were mounted on a three-axis (*x,y,z*) motion control stage (Aerotech), placed under the F-theta lens.

4.3.2 Intensity modulation using SLM

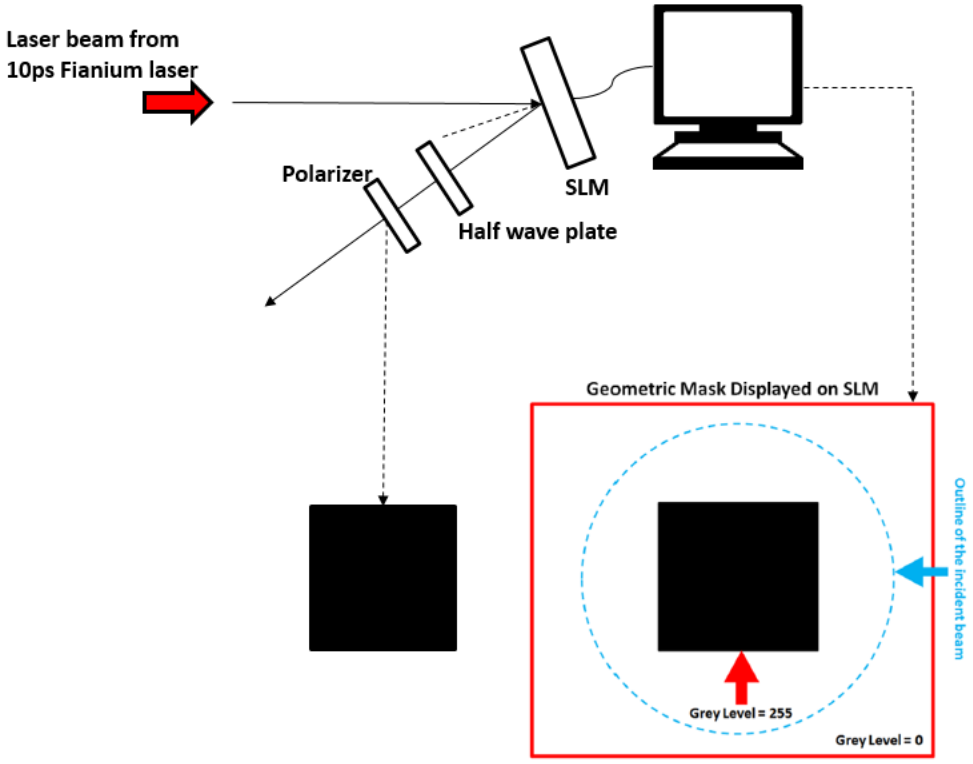

Figure 4.4 A schematic of SLM setup

As shown in Figure 4.4, a half wave plate and a polarizer were placed after the Holoeye LC-R 2500. The LC-R2500 has a 45 degree twisted nematic LC layer which was already introduced in Chapter 3. When the grey level changes from 0 to 255, the polarization of incident beam changes 45°, independent from the incident angle. Therefore, as in Figure 4.4, if a black square (gray level=255) was put on a white screen (gray level=0), the polarization of laser beam will change 45° in the black area while the other area remain unaffected. Thus, putting a polarizer with certain fast axis angle behind the SLM will partially block the unwanted area and let the useful part pass through.

4.3.3 Beam reconstruction at imaging plane

As discussed in 4.2, for image-based beam shaping, the efficiency will decrease significantly when the imaging surface is far away from the focal plane. In order to ensure the intensity at imaging plane is sufficient for material processing, the distance between focal plane and imaging plane should be as short as possible. The position of imaging plane A'' can be calculated, based on the thin lens imaging equation below.

$$\frac{1}{\mathrm{u}}+\frac{1}{\mathrm{v}}=\frac{1}{f} \tag{4-17}$$

where u is the objective distance and v is the image distance. As shown in equation (4-17), in order to minimize the image distance, the objective distance should be as long as possible. In this experiment, $\mathrm{u}\approx 15000\mathrm{mm}$ is the distance from the SLM to the F-theta lens, f=100mm is the focal length of the F-theta lens and v can be calculated as:

$$\mathrm{v}=\frac{f\mathrm{u}}{\mathrm{u}-f}\approx 100.67\mathrm{mm} \tag{4-18}$$

The gap between the focal and imaging plane is:

$$x=f-\mathrm{v}\approx 0.67\mathrm{mm} \tag{4-19}$$

The magnification of the image system is $\mathrm{M}\approx 1/150$. Since the size of the shaped beam at A was approximately 3mm, the size of the reconstructed beam should be

approximately 20μm, which was comparable to the beam waist at focal plane and guaranteed sufficient fluence to machine various materials. To better understand the importance of a long objective distance, a figure was made as below:

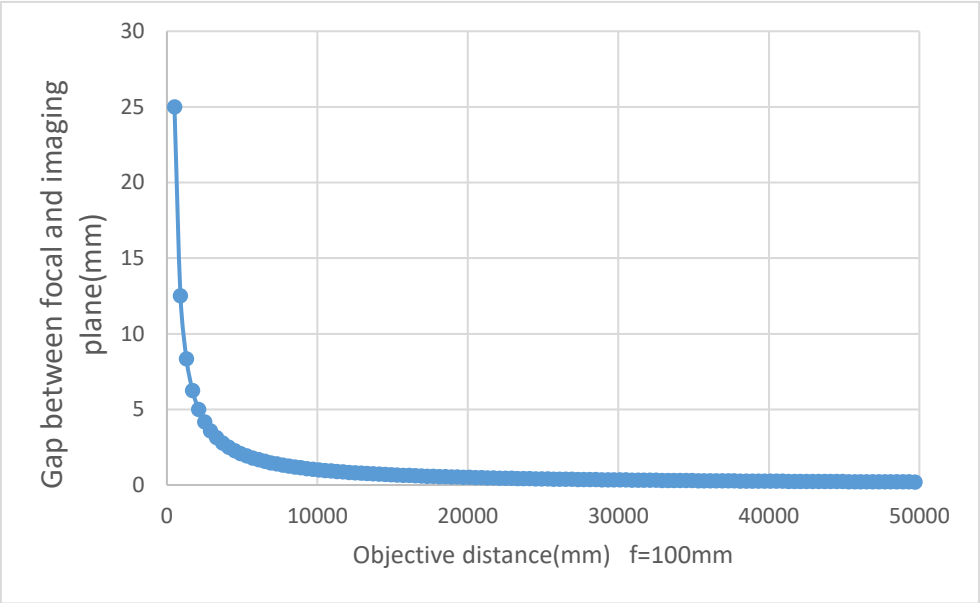

Figure 4.5 Gap between focal and imaging plane versus objective distance

As shown in Figure 4.5, when the objective distance was shorter than 2100mm, the gap between focal and imaging plane is larger than 5mm, and the magnification is larger than M=1/21. In this case, the size of the reconstructed beam should be approximately 143μm, and the intensity will be insufficient to generate any footprint on surface of sample. When the objectives reaches 10100mm, the gap between focal and imaging plane can be calculated as 1mm, the magnification is M=1/101 and the beam diameter at imaging plane was approximately 30μm. When the objective distance keeps increasing, the gap between focal and imaging plane decreases slowly

and closes to 0 at infinity. However, due to the original beam waist and diffraction limit, it become meaningless when size of the beam is below approximately 15μm. Therefore, using this method, the objective distance is recommended to be between 5000mm to 20000mm to have sufficient power intensity and reasonable beam size at same time.

4.4 Results and Discussion

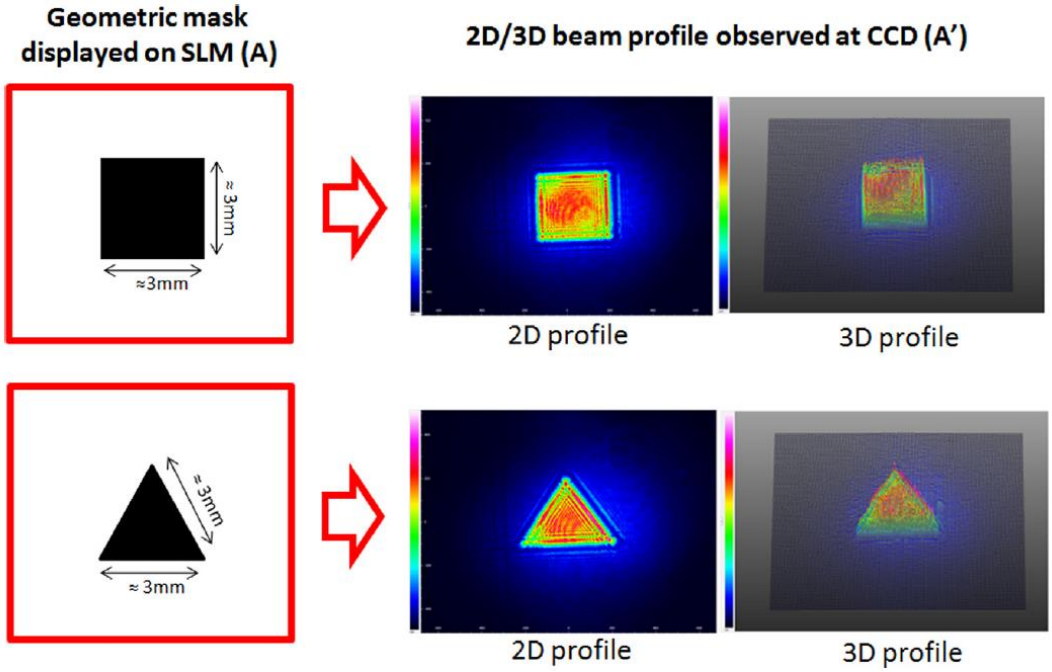

Figure 4.6 Geometric mask, square and triangle, applied to the SLM and the correspondent beam profiles observed using a CCD camera placed at A'

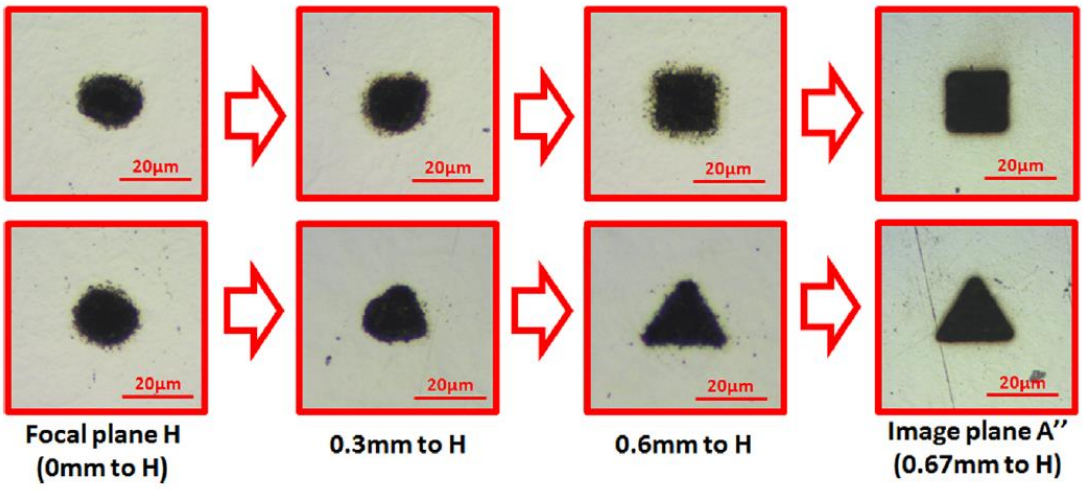

Figure 4.7 Micrographs of machined footprints on a polished stainless steel sample, machined at different heights on the stage from the focal plane H to the image plane A'' Pulse energy $E_p \approx 5\mu J$, Exposure time t=0.5s.

Figure 4.6 shows two geometric masks, square and triangle, applied to the SLM at A and the corresponding beam profile observed at A' (see Figure 4.3). As shown, the beam has been successfully shaped to the desired geometries near the SLM surface. Figure 4.7 shows micrographs of a series of machined footprints on a polished stainless steel sample. The sample was machined at different heights on the Aerotech stage from the focal plane H to the image plane A''. The input laser energy E_p was approximately 5µJ, measured before the scanning galvanometer aperture, and the drilling time for each footprint was 0.5s, i.e. 100k pulses per footprint. When machining at the focal plane H, the footprints were not shaped to the desired geometries at A due to diffraction effects. As shown, the shape of footprints gradually changes when approaching the image plane A'', and the desired geometries (square

and triangle) are successfully reconstructed at the image plane A'' with a size of 20μm, comparable to the beam waist.

By using this technique, arbitrary shapes can be obtained at the imaging plan (A'') with sufficient fluence to process different type of materials. As shown in Figure 4.8, the beam was shaped to a circle, ring and star geometries by applying corresponding geometric masks on the SLM (A) (observed at CCD A') and successfully ablated the polished stainless steel sample at the imaging plane (A''). The input laser pulse energy (Ep), measured before the scanning galvanometer aperture, was $\approx 5\mu J$, and the dwelling time to create each footprint was 0.5s, allowing 100k pulses per footprint.

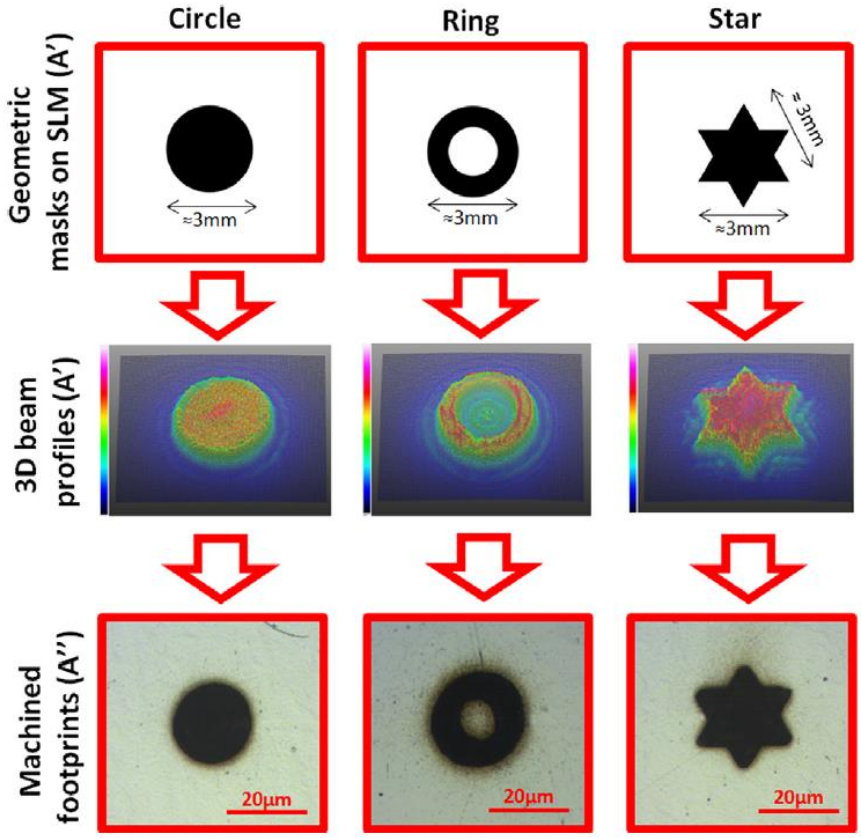

Figure 4.8 Beam shaped to circle, ring and star geometries. First line: geometric masks applied to the SLM (A). Second line: 3D beam profiles observed by the CCD camera (A''). Third line: mircographs of machined footprints at surface of the stainless steel sample (A''). Pulse energy $E_p \approx 5\mu J$, Exposure time t=0.5s.

Figure 4.9 shows the beam profiles observed by the CCD and the footprints machined on a stainless steel sample when changing size of geometric mask. The input laser beam diameter was measured $\approx 6mm$. As shown in Figure 4.9, the shaping quality is affected by the size of the geometry displayed on the SLM at A. When applying a laser sized square (e.g. 5mm×5mm or 4mm×4mm), the machined footprint at the image plane did not have a good square shape. However, when applying a smaller sized

square (e.g. 3mm×3mm or 2mm×2mm), the machined footprint was accurately shaped to a square.

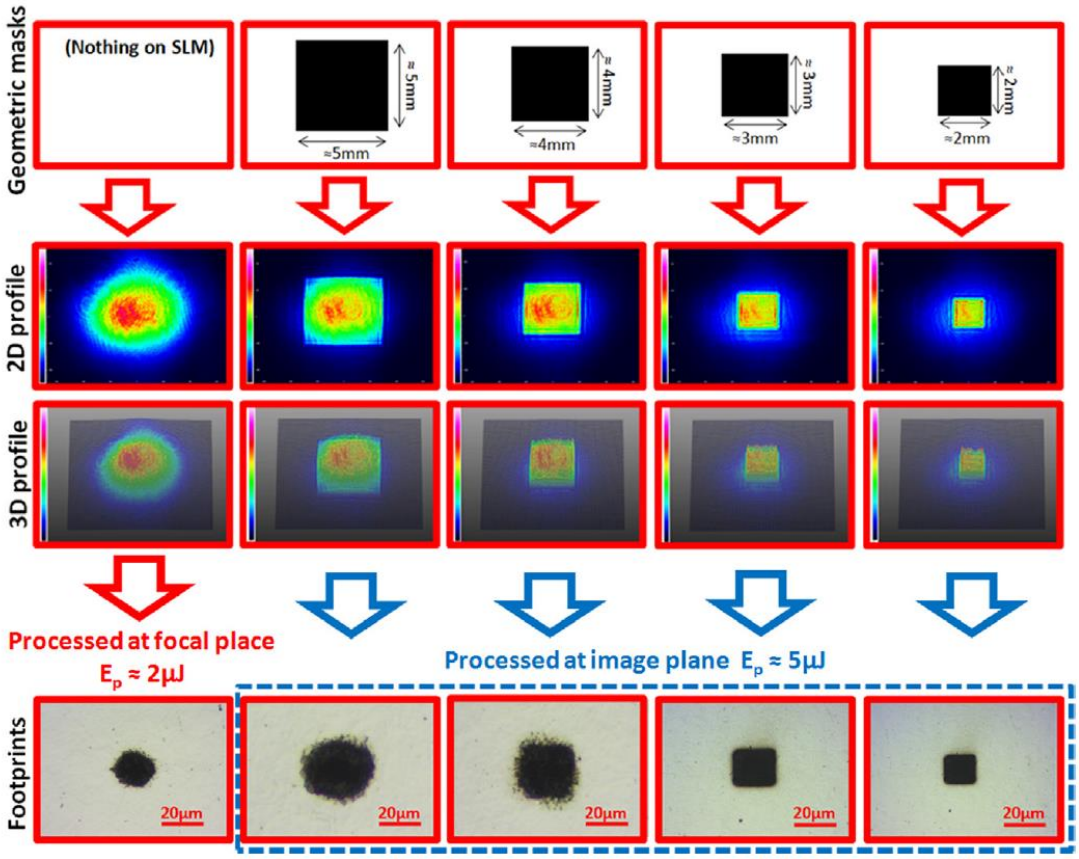

Figure 4.9 Shaping when changing the size of geometric mask (i.e. the square size). First line: geometric masks applied on the SLM. Second and third line: 2D and 3D beam profiles observed by the CCD camera. Fourth line: mircographs of machined footprints at surface of stainless steel sample. Exposure time t=0.5s.

Shaping efficiency was measured by the following method. Firstly, a beam intensity profile was observed by the CCD at A' when applying a geometric mask at A. The integral of the shaped area intensity profile ($\oint I_{shaped} ds$) and the entire intensity profile ($\oint I_0 \, ds$) are then recorded, as shown in Figure 4.10. The shaping efficiency (η)

is the ratio between $\oint I_{shaped} ds$ and $\oint I_0 \, ds$, cacluated using the equaitons below.

$$\eta = \frac{\oint I_{shaped} ds}{\oint I_0 ds} \times 100\% \tag{4-20}$$

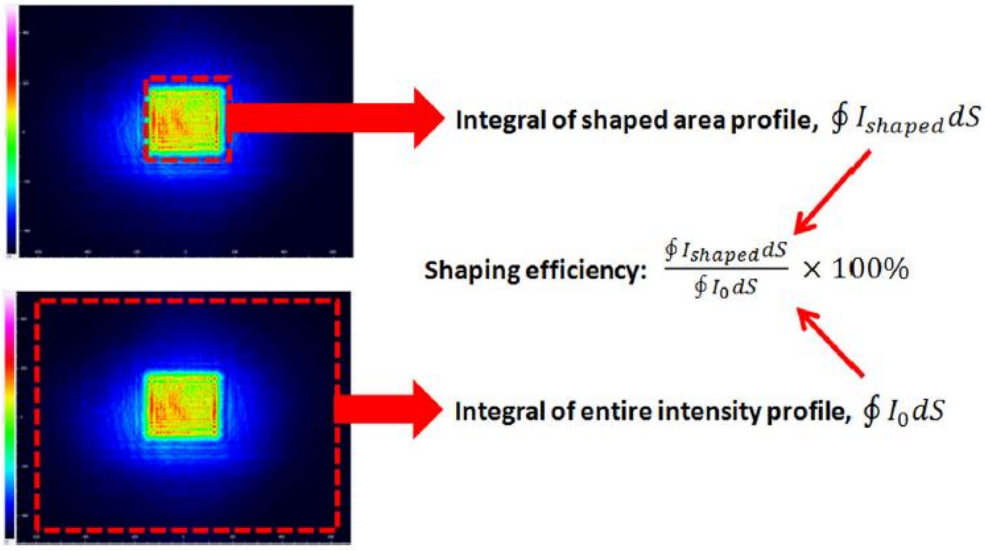

Figure 4.10 Shaping efficiency mearsurement

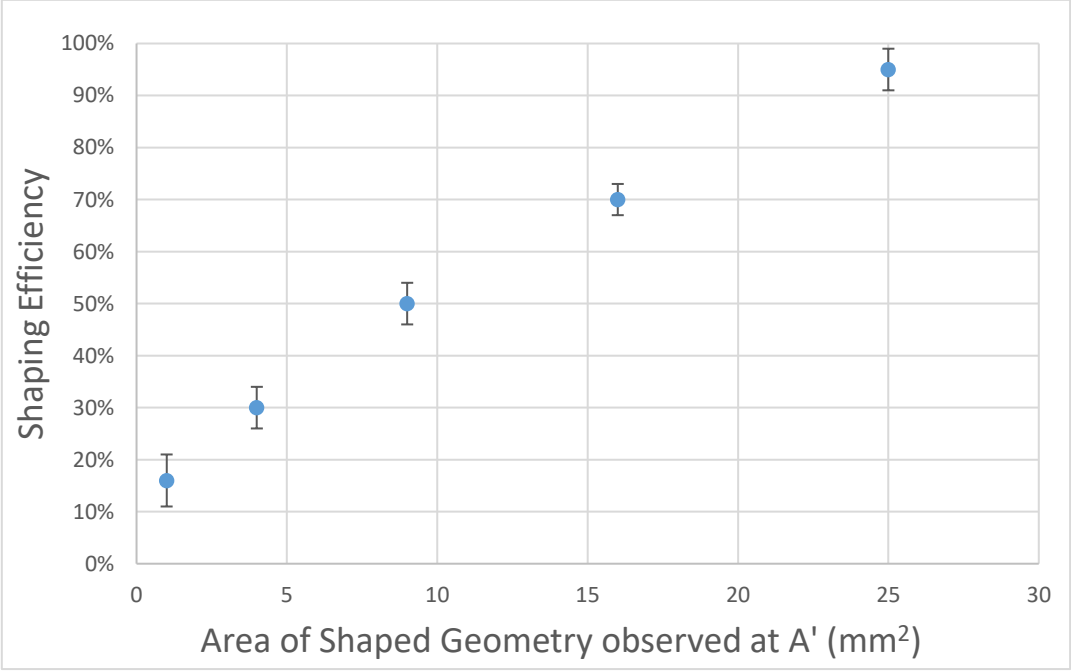

Figure 4.11 Shaping efficiency against the area of the shaped geometry observed at A' by the CCD

Figure 4.11 shows how the shaping efficiency varies when changing the area of the shaped geometry observed at A' by the CCD. As shown, laser shaping geometry gives higher shaping efficiency. This is probably due to the fact that the larger geometry is acting on more area of the original beam.

As demonstrated in Figure 4.11, both shaping quality and efficiency are significantly affected by the size of the geometric mask. In order to machine a accurate shaped footprint on a sample with a high efficiency, the size of the geometric mask should be appropriate size relative to input beam diameter.

4.5 Summary

An original ultrafast laser beam shaping technique for material processing using a spatial light modulators (SLM) has been demonstrated in this chapter. Simple and direct geometric masks are used to shape the input beam at the diffraction near-field. Arbitrary intensity shapes can be obtained and then reconstructed at the imaging plane of a focusing lens. The size of the shaped beam ($\sim 20\mu m$) is comparable to the beam waist at the focal plane. A polished stainless steel sample was machined by the shaped beam at the imaging plane. The machined footprint has the corresponding shapes of the beam. Both shaping quality and efficiency vary when changing the size of input beam. Smaller masks size gives a better shaping quality due to the shaping ability of the SLM, however, the shaping efficiency is decreased. Depending on the

input beam diameter, appropriate mask sizes should be selected to keep a good balance between the shaping quality and efficiency.

Although arbitrary shapes were obtained and reconstructed, the intensity distribution still remains the Gaussian distribution as for the incident beam. Gray level masks are investigated in the next chapter.

Chapter 5 Beam shaping at the imaging plane by gray level masks

5.1 Introduction

Beam outline profile shaping using binary masks has been introduced in Chapter 4. Geometric shapes were generated at the objective plane and reconstructed at the imaging plane. However, the intensity remained the original Gaussian distribution and the machined footprints were uneven in depth. This chapter presents the results of the Fianium Femtopower picosecond laser beam ($\tau_p \approx 20ps, \lambda = 1064\text{nm}$ and f=0.2MHz) shaping for both outline profile and intensity distribution at the imaging plane by gray level masks using a Holoeye LC-R2500 SLM.

The specific experimental setup will be explained in section 5.2, in which the shaping ability of the Holoeye LC-R2500 will be discussed. Additionally, the methodology for gray level mask generation will also be introduced. Section 5.3 presents the results and discussion about shaping quality and efficiency.

Section 5.4 presents an algorithm for generating high quality gray level masks using Matlab. In addition to Gaussian and flat-top beams, arbitrary intensity distributions have also been obtained.

5.2 Experimental methodology

5.2.1 Overall setup

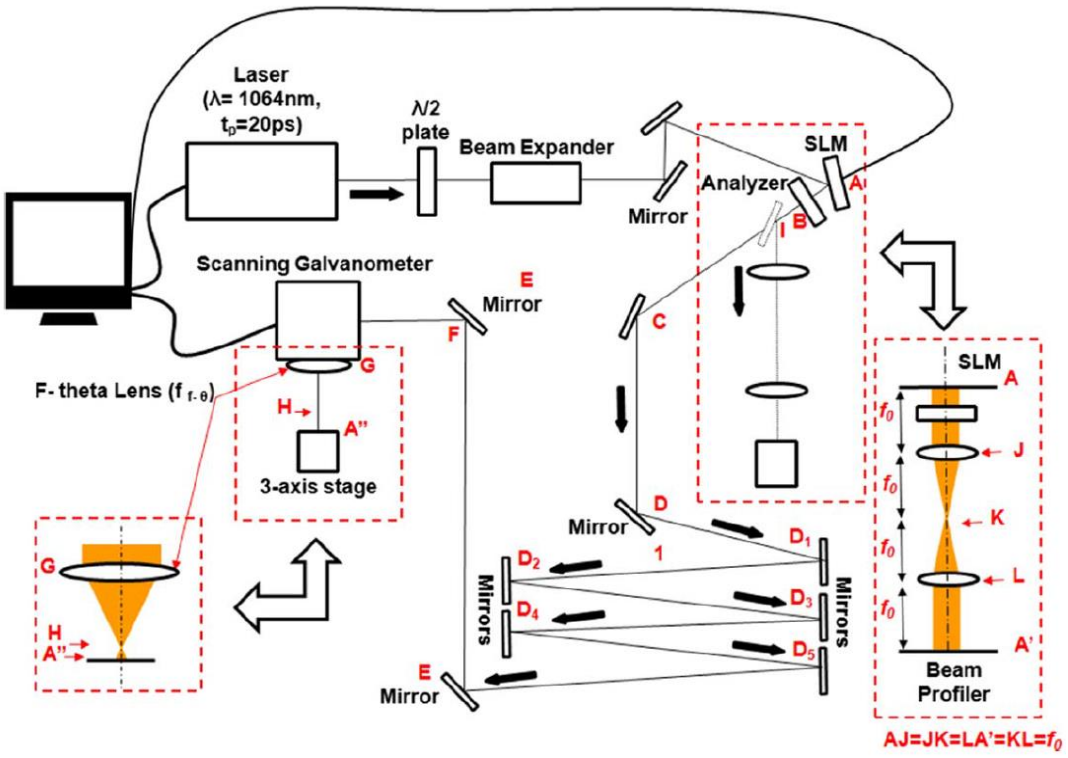

Figure 5.1 Experimental setup for image-based outline profile and intensity beam shaping

As shown in Figure 5.1, a linear polarized laser beam output (beam diameter: Dia.≈0.8mm, pulse duration: *tp*=20ps, wavelength: λ=1064nm, and repetition: *f*=200kHz) from a picosecond fiber laser system (Fianium) passed through a half-wave plate used for adjusting the polarization direction, a beam expander (M≈×5), two plane mirrors for controlling the beam path, and illuminated on a reflective, liquid crystal SLM (Holoeye LC-R 2500).

An analyzer was placed after the SLM to modulate the laser beam intensity. Due to the 0°-45° twisted nematic microdisplay cells, the output beam polarization rotates at a certain angle depending on how much the relevant LC cell is twisted. Amplitude modulation is, hence, achieved by adding a polarizer (analyzer) afterward.

When observing the beam profile, the laser beam was reflected by a flip mirror and then passed through two positive lenses (focal length: f_o=200mm) to form a 4*f* system to reach a CCD camera-based laser beam profiler (Thorlabs). When processing, the flip mirror was removed from the optical alignment. The beam, thus, traversed a long distance by multiple reflections on a series of mirrors before reaching a scanning galvanometer, and a focusing *f*-theta lens($f_{f-\theta}$=100mm). Machining samples were mounted on a three-axis(*x,y,z*) motion control stage (Aerotech), placed under the *f*-theta lens.

5.2.2 Shaping ability of the Holoeye LC-R2500 SLM

As introduced in Chapter 3, for the Holoeye LC-R2500 SLM, when the grey level changes from 0 to 255, the polarization of the incident beam changes by 45°, independent from the incident polarization angle. For this experimental setup, the output intensity can be expressed as:

$$I_{out} = \frac{1}{2} \times [I_{in} \times (1 - cos2\theta)] \quad (5\text{-}1)$$

Where I_{out} is the laser output intensity after the polarizer, I_{in} is the laser input intensity and θ is the polarised angle of incident beam. Since $0^\circ < \theta < 45^\circ$ and $0^\circ < 2\theta < 90^\circ$, and a period of a sine function is 360°, the selection of shaping range is critical. In order to explain the shaping range selection, a schematic of a cosine function $\frac{1}{2}(\cos\alpha + 1)$ from 0° to 360° is shown in Figure 5.2. For example, two ranges are selected from a cycle of a cosine function, both of them contains a phase difference of $\frac{\pi}{2}$. If we define the shaping ability A as:

$$\mathrm{A} = \frac{E_{max}}{E_{min}} \tag{5-2}$$

Where E_{max} is the highest efficiency and E_{min} is the minimum efficiency. When the shaping ability A reaches nearly infinity, it means the intensity of output beam can be reduced to 0 and any intensity distribution can be obtained theoretically. When the shaping ability A decreases, the intensity modulation ability of SLM decreases correspondingly.

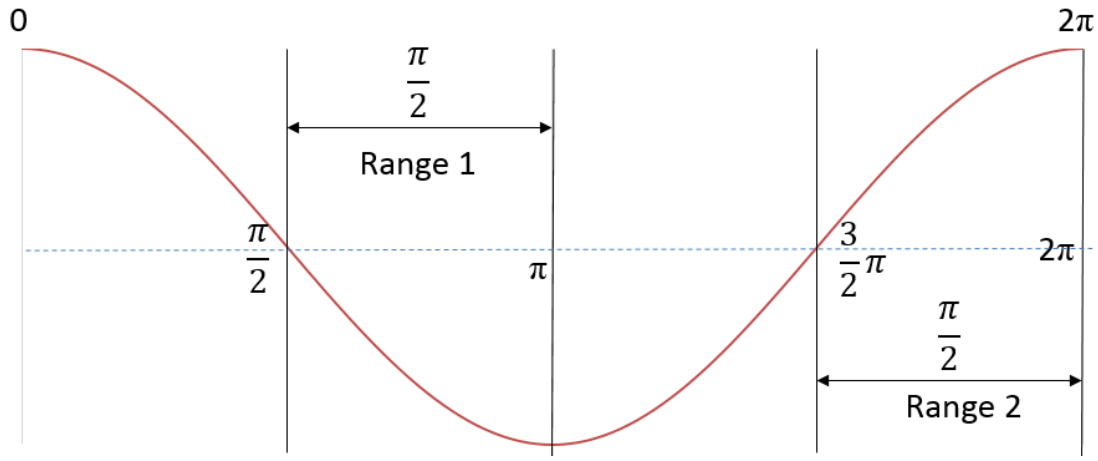

Figure 5.2 Schematic of the shaping range selection

Range 1 is from $\frac{\pi}{2}$ to π and the shaping ability A_1 can be calculated as:

$$A_1 = \frac{\frac{1}{2}(\cos\frac{\pi}{2}+1)}{\frac{1}{2}(\cos\pi+1)} \to \infty \quad (5\text{-}3)$$

Range 2 is from $\frac{3\pi}{2}$ to 2π and the shaping ability A_2 can be calculated as:

$$A_2 = \frac{\frac{1}{2}(\cos 2\pi+1)}{\frac{1}{2}(\cos\frac{3\pi}{2}+1)} = 2 \quad (5\text{-}4)$$

It can be seen from equation (5-4) and (5-3) that the shaping ability of A_1 is much larger than A_2, which means that range 1 is more flexible for beam shaping. However, the efficiency also needs to be considered.

For range 1, the highest efficiency is:

$$E_{1max} = \frac{1}{2}\left(\cos\frac{\pi}{2}+1\right) \times 100\% = 50\% \quad (5\text{-}5)$$

And for range 2, the highest efficiency is:

$$E_{2max} = \frac{1}{2}(\cos 2\pi + 1) \times 100\% = 100\% \quad (5\text{-}6)$$

Figure 5.3 shows a comparison between shaping ability and shaping efficiency using a Holoeye LC-R2500 SLM. In the phase range between π and $\frac{3}{2}\pi$, these two curves show an opposite trend, therefore there is not an ideal phase range for perfect beam shaping. Therefore, the selection of shaping range should be based on the specific situation such as the input intensity, target intensity, shaping accuracy and the optimisation for the best results.

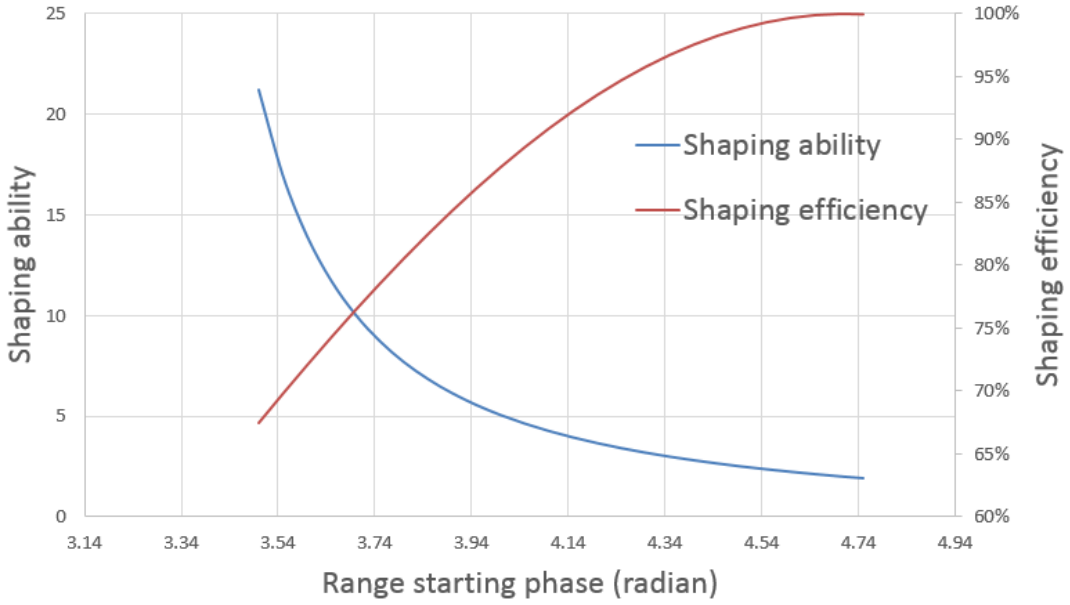

Figure 5.3 Shaping ability versus shaping efficiency at different starting phase

5.2.3 Generation of flat-top beam using grey level gradient masks

As discussed in section 5.2.2, a Holoeye LC-R 2500 SLM is a reflective Liquid Crystal on

Silicon (LCoS) based spatial light modulator (SLM). By changing the gray level from 0 to 255, the output polarization varies from 0° to 45° accordingly. Based on this characteristic, gray level masks were generated to modify the intensity distribution accurately.

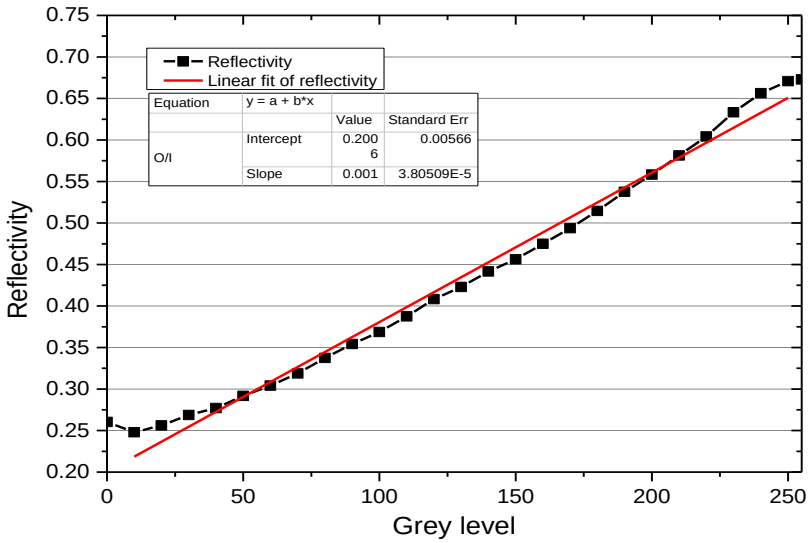

Figure 5.4 The SLM reflectivity versus mask gray level

As shown in Figure 5.4, a phase area was selected to make the trendline as close to a linearly function as possible and give sufficient shaping ability and efficiency. The relation between reflectivity (R) and gray level (GL) can be expressed as:

$$R = f(GL) = 0.001GL + 0.2006 \qquad GL \in [0,255] \tag{5-7}$$

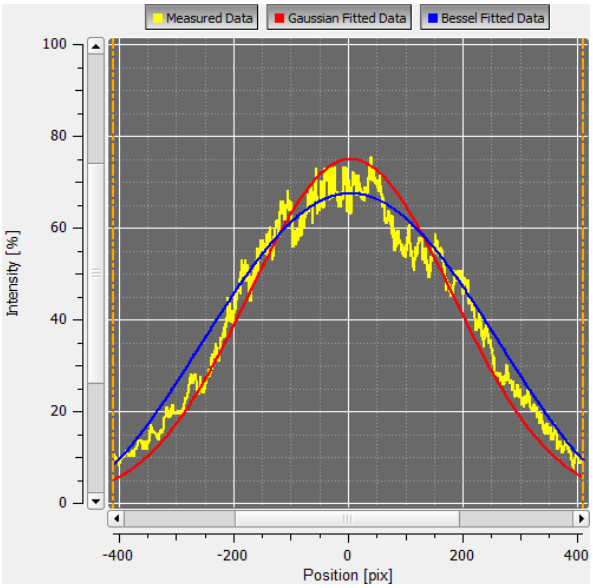

Figure 5.5 Intensity distribution along beam diameter

Figure 5.5 shows that the original laser beam profile (y) well matched with the Gaussian distribution (red line) in equation (5-8).

$$y = \frac{1}{\sigma\sqrt{2\pi}} e^{\frac{-x^2}{2\sigma^2}} \tag{5-8}$$

Where σ is calculated to be 2.03, based on the data shown in Figure 5.5. Thus, y becomes:

$$\mathrm{y} = \mathrm{g(x)} = \frac{1}{5.08} e^{\frac{-x^2}{8.24}} \tag{5-9}$$

Since the shaped beam profile is the product of the original beam profile (y) and the reflectivity of SLM (R), a flat top distribution can be obtained when:

$$\mathrm{y} \times R = \mathrm{c} \tag{5-10}$$

Where c is a constant. By combining equation (5-9) with (5-10), the distribution of reflectivity (R) becomes:

$$\mathrm{R} = \mathrm{ce}^{\frac{\mathrm{x}^2}{8.24}} \tag{5-11}$$

By combining equation (5-7) and (5-11), we can derive:

$$ce^{\frac{x^2}{8.24}} = 0.001GL + 0.2006 \tag{5-12}$$

As discussed in Chapter 4, both shaping quality and efficiency vary when changing the size of geometric masks. A smaller mask size gives better quality; however, it decreases the shaping efficiency. This is mainly due to the lack of shaping ability at a relatively high efficiency. Depending on the input beam diameter, an appropriate mask size should be used to keep a good balance between the shaping quality and efficiency. In this research, $x \in [-2,2]$ (i.e. the length of 400pixels, corresponding to ≈ 2.6mm) was set to balance the shaping quality and the efficiency. Figure 5.6 shows how the original Gaussian profile (y) is shaped to flat-top (y') with the intensity mask that modulates the reflectivity of the SLM (R).

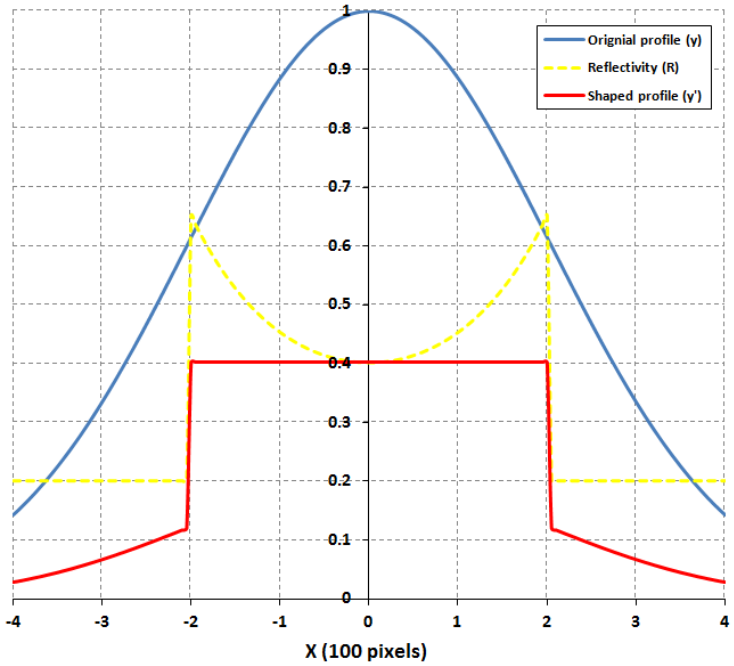

Figure 5.6 Gaussian profile (y) shaped to flat-top (y') with the intensity mask that modulates the reflectivity of SLM (R) y' = y×R

When x=±2 (i.e. the edge of the mask geometry), the reflectivity (R) should reach the maximum and GL hence should be 255, based on Figure 5.4. So, m is calculated to be 0.277. Thus:

$$GL = \frac{0.277e^{\frac{x^2}{8.24}} - 0.20}{0.001} \quad x \in [-2,2] \tag{5-13}$$

Based on equation (5-13), intensity masks with various shapes were created using Matlab. As shown in Figure 5.7, two GL gradient masks were created to shape the beam to (a) circle flat top and (b) square flat top.

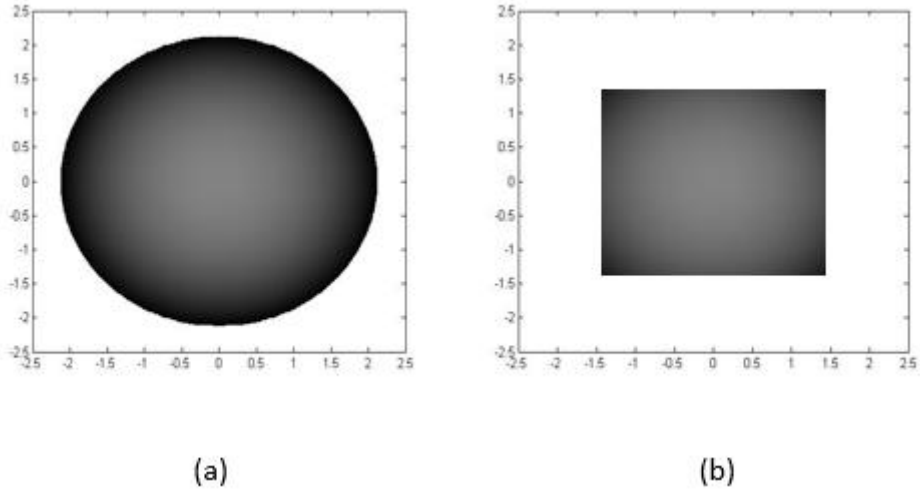

Figure 5.7 Grey level gradient masks generated by Matlab

5.3 Results and discussions

5.3.1 Beam shaping results observed by CCD camera at A'

As shown in Figure 5.8, the first line shows geometric binary and grey level masks applied to the SLM, while the second and the third line show the corresponding beam profiles observed at A' (Figure 5.1) and intensity distribution along the beam diameter, respectively. The binary masks only shaped the outline profile but left the inside intensity distribution essentially unchanged, while the 256 grey level masks shaped both the outline profile and the inside intensity distribution, hence successfully created circular and squared flat-top beams.

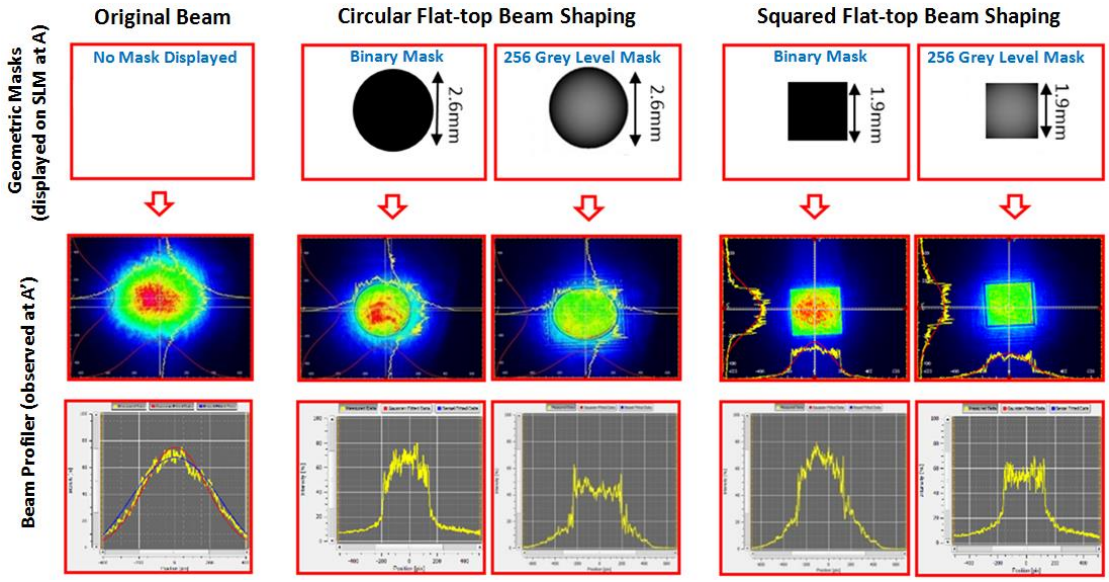

Figure 5.8 Comparison between the binary and 256 grey level masks shaping results - First line: geometric masks applied on the SLM. Second line and Third line: 2D beam profile and intensity distribution across the beam diameter, observed by the beam profiler at A'

5.3.2 Shaped beam machining results at A''

Figure 5.9 and 5.10 shows the circular and squared flat-top beam machined results, respectively. The beam was shaped using the binary (upper) and 256 grey level masks (lower). Footprints were fabricated on a polished titanium sample by the shaped laser beams at the image plane A". The input laser pulse energy (Ep) was approximately 2.1 µJ, measured before the scanning galvanometer aperture. Since the laser frequency was F = 200kHz repetition rate and the drilling time for each footprint was 1s., ~200k pulses were used to fabricate each footprint. The machined footprints were then observed using the white light interferometer (WYKO). As shown in Figure 5.9, the

footprints fabricated by binary masks show an approximately Gaussian shaped bottom indicating that the inside beam intensity distribution was unshaped. The footprints fabricated by 256 grey level masks demonstrated a relatively flat bottom. This demonstrates a good match between the footprint shapes machined at the image plane at A" and the created beam shapes observed at A', as shown in Figure 5.8.

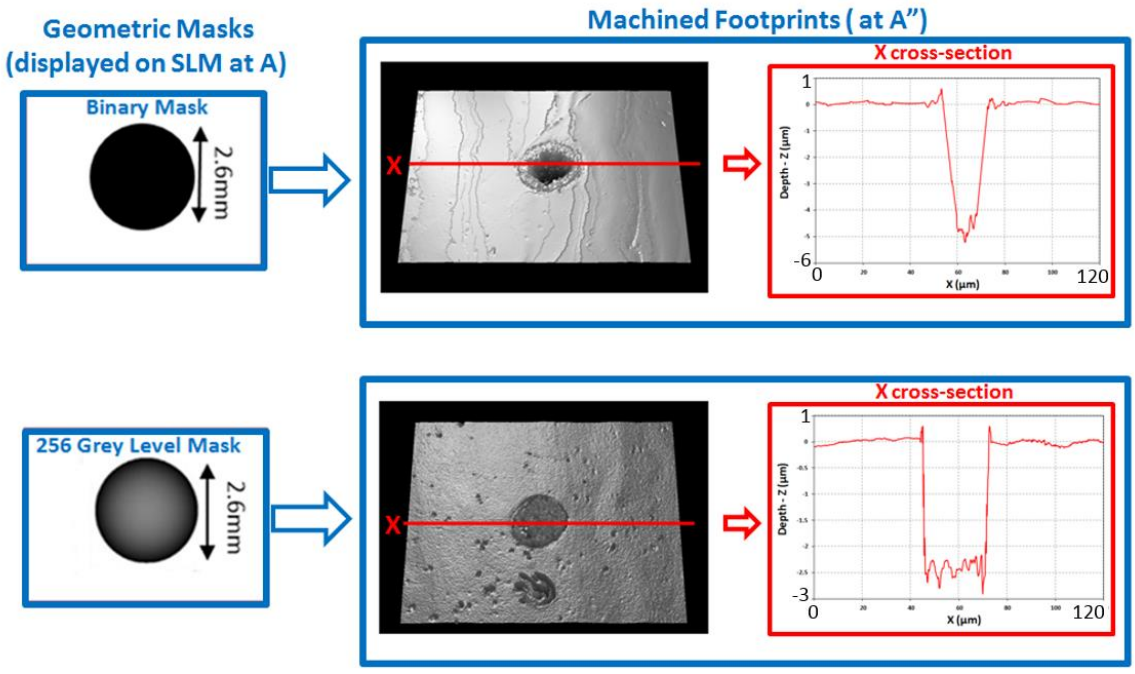

Figure 5.9 Comparison between binary and 256 grey level masks machining results (circular flat-top) – upper: using binary mask; lower: using 256 grey level mask. Pulse energy $E_p \approx 2.1\mu J$, Exposure time t=1s.

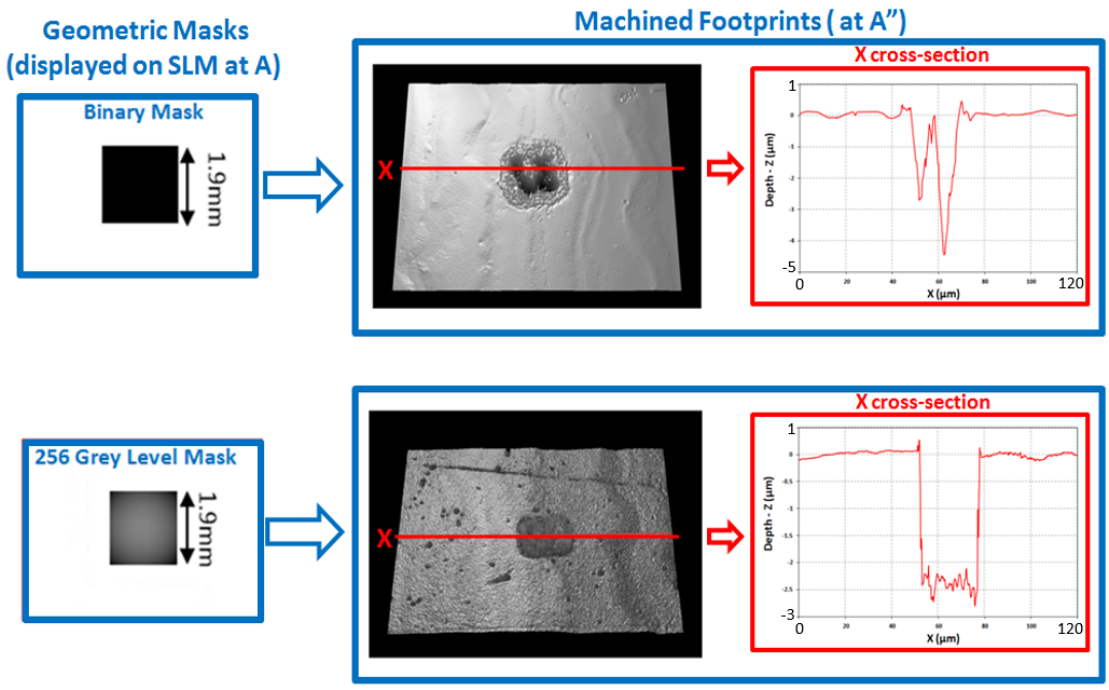

Figure 5.10 Comparison between binary and 256 grey level masks machining results (squared flat-top) – upper: using binary mask; lower: using 256 grey level mask. Pulse energy $E_p \approx 2.1\mu J$, Exposure time t=1s.

5.3.3 Shaping quality and efficiency versus the size of mask

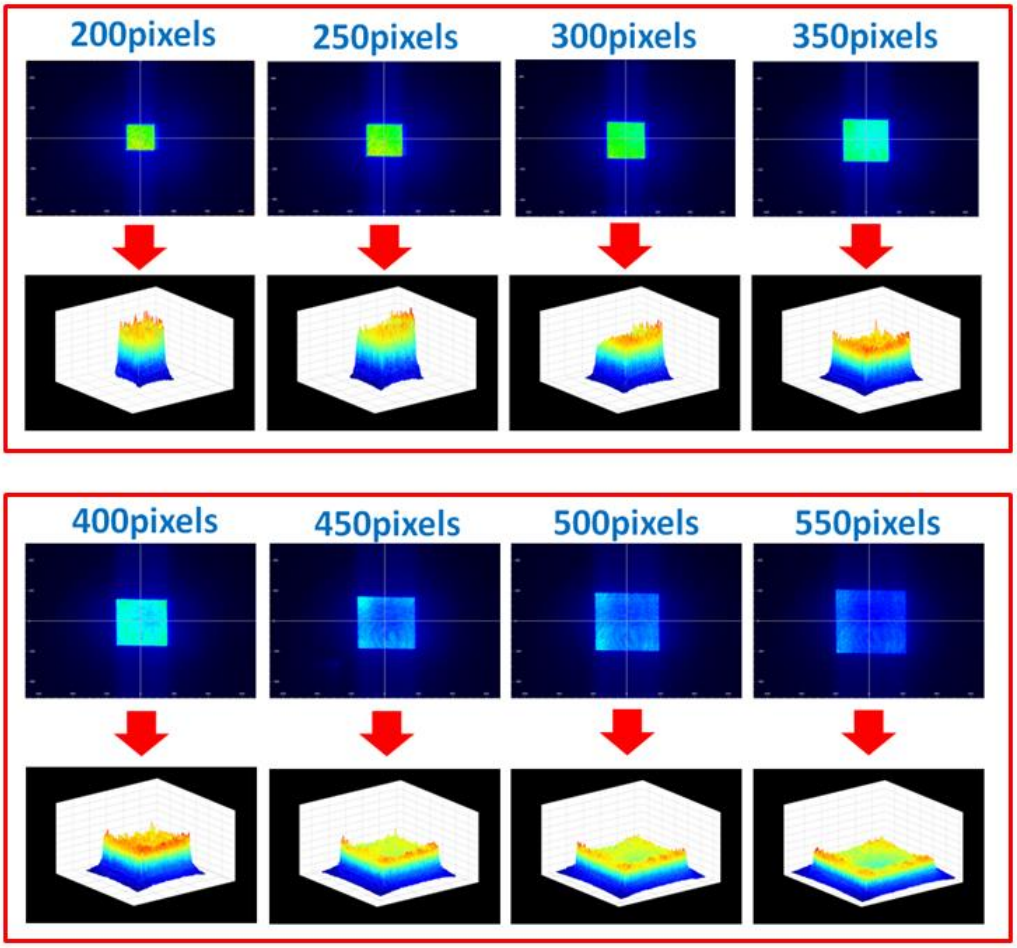

Figure 5.11 Shaping by varying mask size on the SLM (side length of mask varied from 200 to 550pixels)

Both shaping quality and efficiency has been found to change when varying the size of the geometric mask. Figure 5.11 shows the shaped beam profile observed at A' when varying the mask size (side length varied from 200 to 550pixels).

In order to quantitatively study the beam quality variation, images of shaped beam

profiles observed at A' were analyzed by Matlab. As shown in Figure 5.12, the lower right corner matrix was extracted, which quantitatively demonstrated the intensity distribution in a tiny area (3×3 pixels). Accordingly, an entire shaped area matrix can be extracted. A roughness values (R) of the shaped area can be defined using the equation below:

$$R = \frac{\sigma}{M} \times 100\% \tag{5-14}$$

where M is the mean of all the values in the shaped area matrix and σ is the standard deviation. Thus, when shaping the beam to a flat-top, the shaping quality can be quantitatively presented by R. The lower the value of R, the closer the shape is to a uniform flat top.

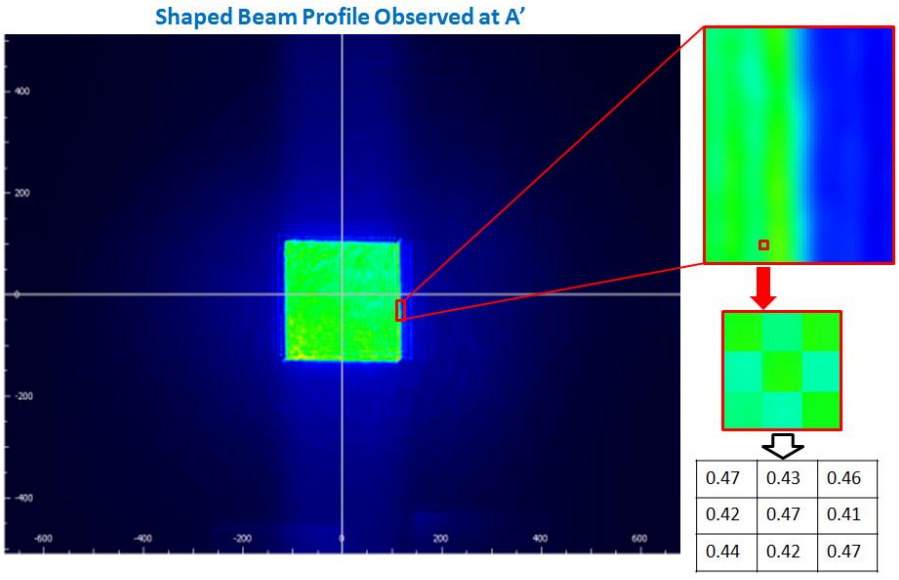

Figure 5.12 Analysis of shaped beam profile observed at A'

Figure 5.13 shows the roughness value against the size of the geometric mask used for square flat-top shaping. When the side length of the mask is between 200 and 550 (unit×100pixels), the roughness values were measured below 10%, indicating a good shaping quality.

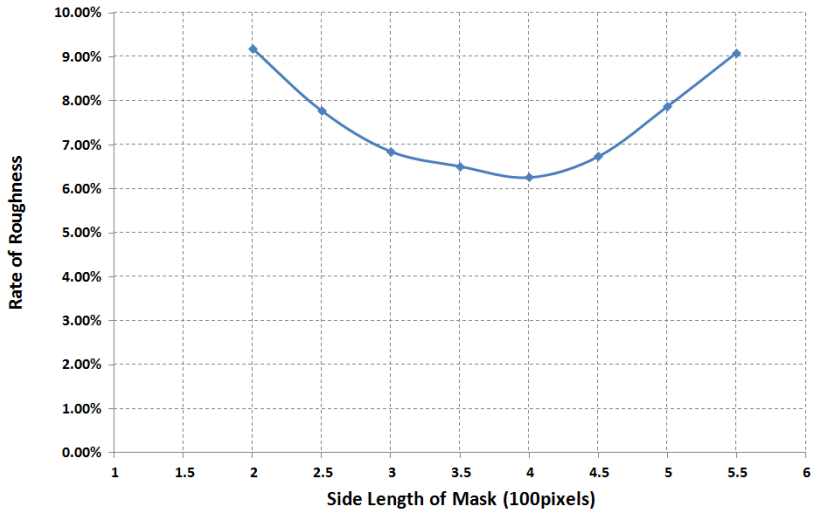

Figure 5.13 Roughness value against the size of the mask

Shaping efficiency can be calculated using the equation below.

$$\eta = \frac{\oint I_{shaped} dS}{\oint I_0 dS} \times 100\% \quad (5\text{-}15)$$

Where $\oint I_{shaped} dS$ is the integral of the shaped beam intensity profile and $\oint I_0 dS$ is the integral of the original beam intensity profile obtained at A'.

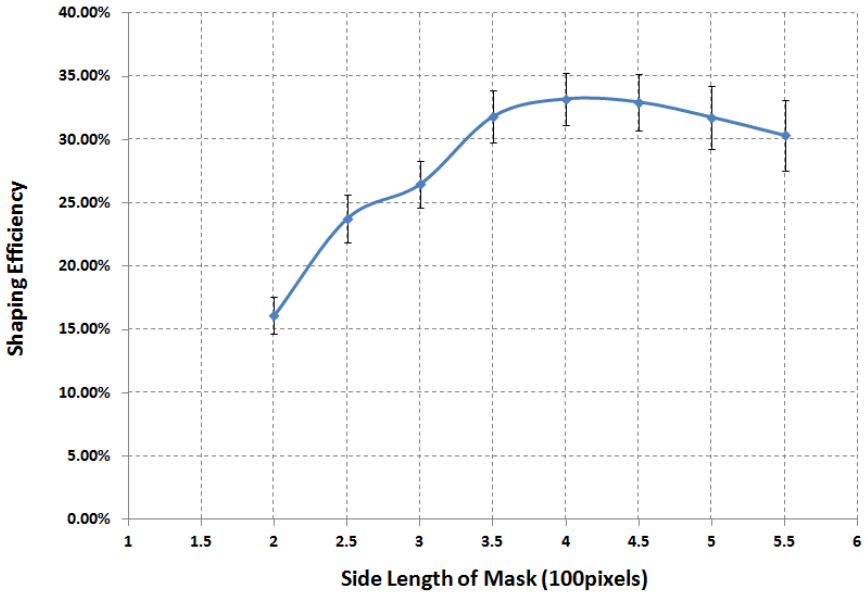

Figure 5.14 Shaping efficiency against the size of the mask

Figure 5.14 demonstrates shaping efficiency against the size of the mask. As shown, when the mask side length was set around 4 (unit×100pixels), the shaping efficiency reached the highest. As shown in Figure 5.15, this is probably because the highest shaping efficiency can be achieved when the rectangular area (A) under the Gaussian curve reaches the maximum (A_{max}). Using equation (5-9), the area A under the Gaussian curve in Figure 5.15 can be defined as :

$$A = f(x) = 2xy = 2xg(x) = \frac{2x}{5.08} e^{\frac{-x^2}{8.24}} \quad (5\text{-}16)$$

Thus, A_{max} is reached when:

$$\frac{df(x)}{dx} = 0 \quad (5\text{-}17)$$

By solving the formula (5-17), we can calculate that the highest shaping efficiency is

achieved when x ≈ 2, i.e. the side length of mask = 2x ≈ 4 (unit: 100pixel), hence the result in Figure 5.14.

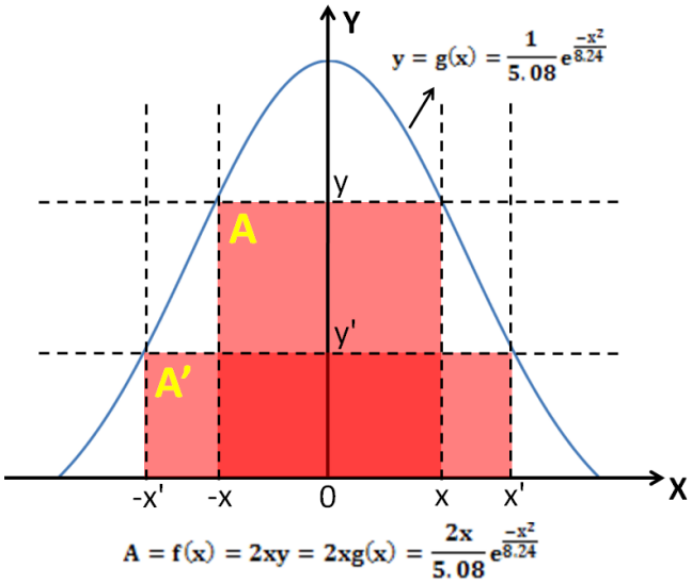

Figure 5.15 How to maximize the shaping efficiency

5.4 Gray level masks for arbitrary intensity distribution programmed using Matlab

The method to obtain flat-top laser beams has been introduced in Section 5.2 and tested in Section 5.3. In order to obtain a flat-top intensity distribution, as in equation (5-10), a constant [c] was set as the target and all the original value were brought to the target value by using a coefficient. The combination of all coefficient were recorded and converted to a gray level figures and finally applied onto the SLM.

In this section, instead of a constant [c], other distributions have been applied into this function, thus creating various intensity distributions of the laser beam. Since the

same SLM is employed, the relationship between reflectivity (R) and gray level (GL) is same as equation (5-7):

$$R = f(GL) = 0.001GL + 0.2006 \quad GL \in [0,255] \tag{5-18}$$

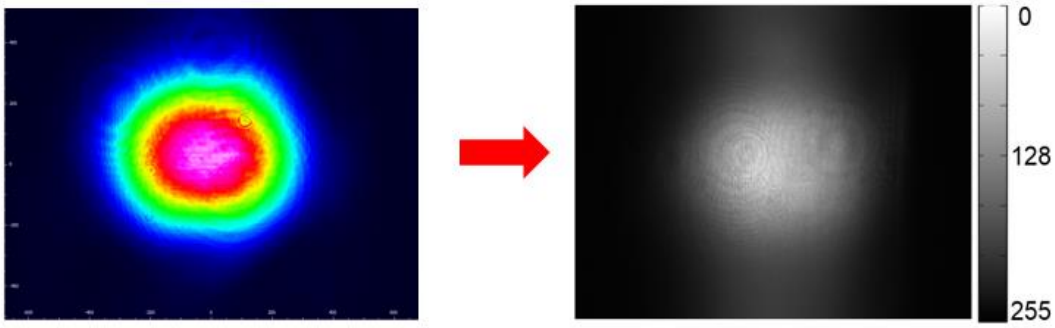

Figure 5.16 Original laser beam profile taken by CCD camera

This technique allows the original beam intensity distribution to be taken into account rather than an assumed Gaussian shape. Figure 5.16 shows the original laser beam profile taken by CCD camera. Image data is exported from camera by pixels (0.645µm×0.645µm) and read by Matlab, in which black colour is set as value 0 and white is set as value 255. The intensity per pixel decreases from highest (white) to 0 (black) linearly. In order to obtain other beam profiles, the function of required intensity distribution (Y) should be proportional to the result of reflectivity (R) multiplied by the original intensity distribution (O).

$$\mathrm{Y} = \alpha \times \mathrm{R} \times \mathrm{O} \tag{5-19}$$

where α is a factor to normalize the required intensity (Y) between 0 and 1. By combining equation (5-18) with (5-19), we can derive:

$$GL = (\frac{Y}{\alpha O} - 0.2006)/0.001 \quad (5\text{-}20)$$

Programming the function of Y and equation (5-20) into Matlab, gray level masks were generated. For instance, a step structure can be obtained by setting Y as a step function:

Z=0.2(x<=100)+0.4(100<x<200)+0.6(x>200) (5-21)

The corresponding structure can be generated by Matlab as in Figure 5.17 (a), and combining equation (5-21) into equation (5-20), a gray level mask can be generated as in Figure 5.17(b)

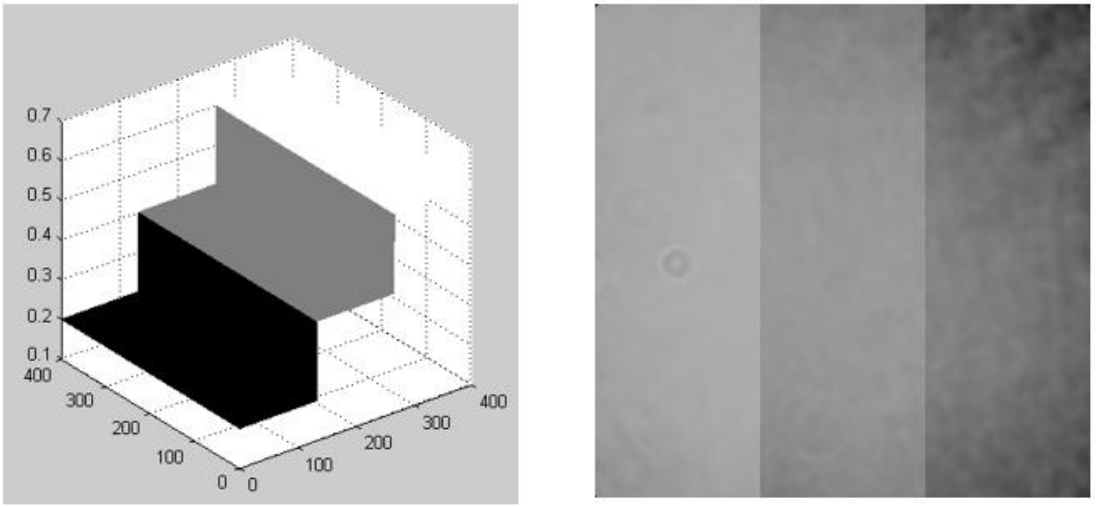

(a) (b)

Figure 5.17 Demonstration of beam shaping using Matlab

By applying the gray level mask onto the SLM, a beam profile can be observed as in Figure 5.18.

As shown in Figure 5.18, the first column shows the desired target intensity distribution. The second column shows the gray level mask generated based on the original beam profile. The third column shows the corresponding beam profiles observed at A'. The original beam profile appears to be circular and a Gaussian distribution. The grey level masks both have successfully shaped the outline profile and inside intensity distribution. It can also be seen that there are some diffraction artifacts in the gray level masks generated from the beam profile images. These appear to not have any significant effect on the shaped beam.

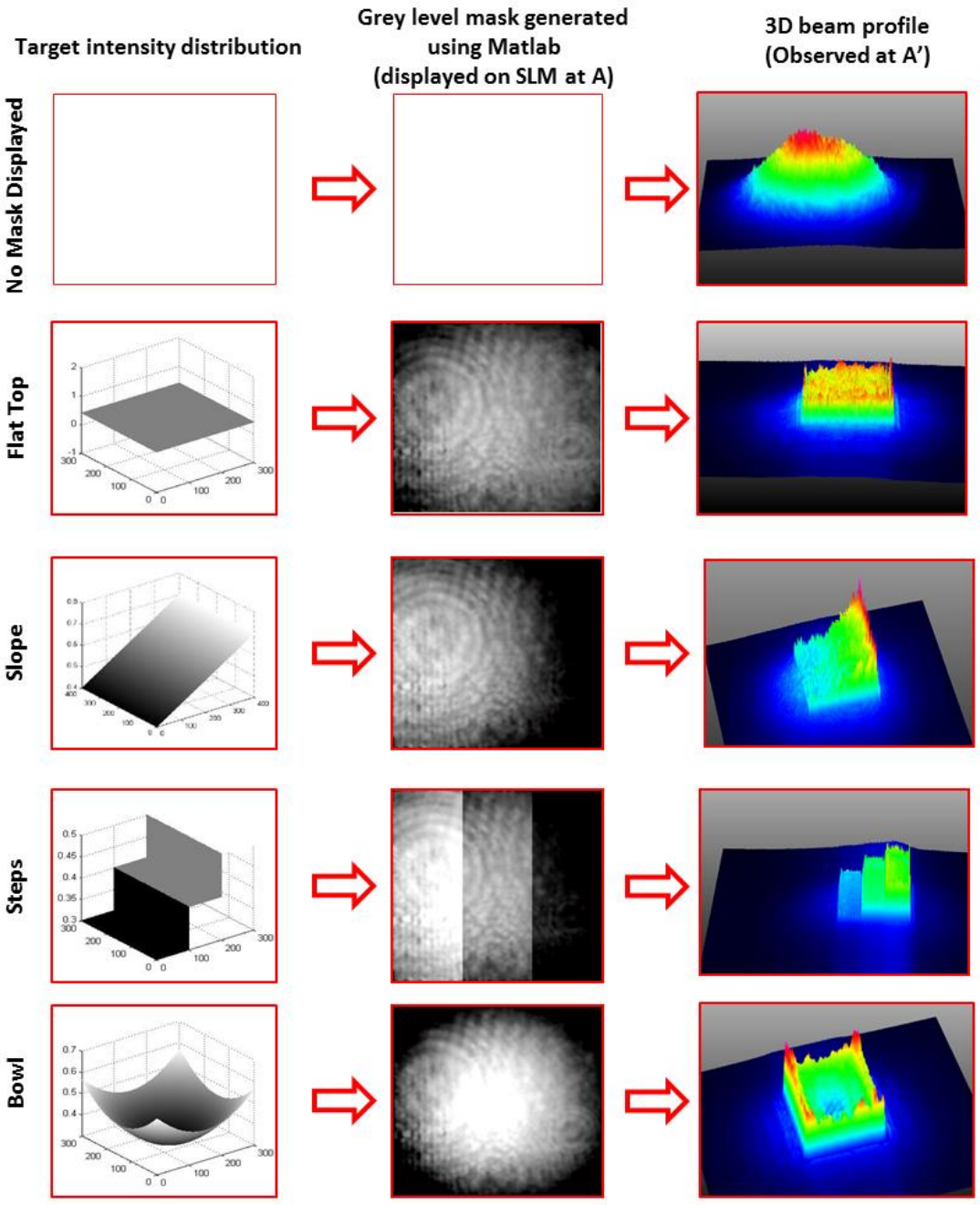

Figure 5.18 Gray level masks generated by Matlab and beam profile observed at A'

5.5 Summary

Image-based laser beam shaping to generate geometric flat-top beams has been

demonstrated in this chapter. Gray level masks designed according to the original beam profile were applied on a SLM to control the shape and intensity distribution of the reflected laser beam. A near Gaussian intensity beam was shaped into a round and square flattop both with uniform intensity. A polished titanium sample was machined by the shaped beam at imaging plane. The machined footprints have the corresponding shape and depth distribution of the beam. Additionally, an algorithm has been developed using Matlab for generating high quality grey level masks to give arbitrary intensity distributions.

Chapter 6 Parallel processing using shaped laser beams

6.1 Introduction

The technique for laser beam shaping for both outline and intensity distribution has been presented in Chapter 5. This chapter presents a novel technique for parallel processing using a shaped High-Q picosecond laser beam (beam parameter: pulse duration: $\tau_p \approx 10ps$, wavelength: λ=1064nm, and repetition: f=10kHz) for material processing. Two SLMs (Hamamastu X10468-03 and Holoeye LC-R2500) have been used to shape the properties (outline shape and intensity distribution) in a single beam spot and diffraction distribution of multiple beams.

The methodology of parallel processing using a shaped beam will be firstly demonstrated in section 6.2, where the theory and concept of convolution will be introduced.

The specific experiments setup will be explained in 6.3, in which two SLMs have been employed and a long beam path has been created.

Section 6.4 presents the results and discussion about the beam shaping quality and efficiency. The size of the mask, the shaping accuracy and processing parameters are discussed.

6.2 Theoretical Explanation

In order to explain the concept of parallel shaping using shaped beams, a theoretical

calculation of the modulation is made based on Fourier optics can be made.

Figure 6.1 shows a schematic of laser parallel processing using shaped beams. A laser beam is illuminated onto the first SLM and a geometric figure is applied. The SLM in this case is used as an intensity modulator. It is worth noting that a polarizing filter is also required here but ignored to simplify explanation. The reflected beam passes a long distance d_0 and reaches the second SLM with a CGH. The reflected beam passed through a thin focusing lens to a sample at imaging plane. It is worth noting that a 4f system is placed between the second SLM and lens to minimize the diffraction, thus the distance between them can be neglected. In Figure 6.1, U_0 is the complex amplitude of the laser at the objective plane, U_l and U_l' refers to the complex amplitude before and after the lens, and U_i is the electric field diffraction pattern at the image plane.

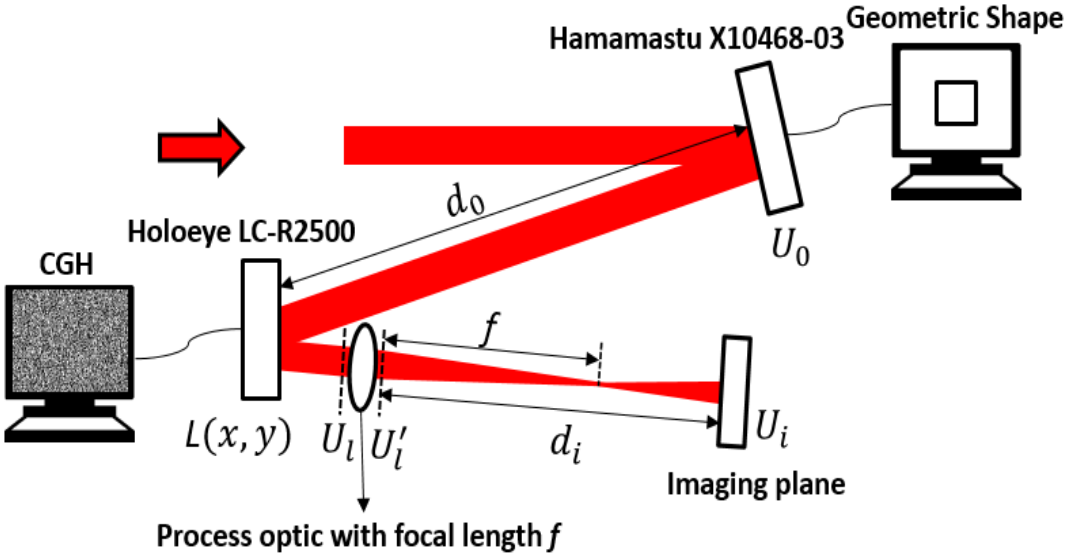

Figure 6.1 Schematic of laser beam shaping using two SLMs

Using Fresnel diffraction, the complex amplitude U_l can be described as:

$$U_l(x,y) = \frac{1}{i\lambda d_0}\exp(ikd_0)\exp[i\frac{k}{2d_0}(x^2+y^2)] \times \iint_{-\infty}^{\infty} U_0(x_0,y_0) \times \exp\left[j\frac{k}{2d_0}(x_0^2+y_0^2)\right]\exp[-i\frac{2\pi}{\lambda d_0}(x_0x+y_0y)]dx_0dy_0 \quad (6\text{-}1)$$

In Fourier Optics, a complex amplitude of a lens t_l can be expressed as:

$$t_l(x,y) = \exp[-i\frac{k}{2f}(x^2+y^2)] \quad (6\text{-}2)$$

$t(x,y)$ is the complex amplitude transmittance function of the CGH. Since the distance between the second SLM and the lens can be neglected, $t(x,y)$ can be combined into the expression of the lens and the new complex amplitude is:

$$t_l'(x,y) = t(x,y)\exp[-i\frac{k}{2f}(x^2+y^2) \quad (6\text{-}3)$$

Therefore, the complex amplitude after the lens at U_l' can be express as:

$$U_l' = U_l(x,y)t_l'(x,y) \tag{6-4}$$

After the laser beam passes d_i and reaches U_i, the electric field diffraction pattern can be calculated using the Fresnel diffraction integral as:

$$U_i(x_i,y_i) = \frac{1}{i\lambda d_0}\exp(ikd_i)\exp[i\frac{k}{2d_i}(x_i^2+y_i^2)] \times \iint_{-\infty}^{\infty} U_l'(x,y) \times \exp\left[j\frac{k}{2d_0}(x^2+y^2)\right]\exp[-i\frac{2\pi}{\lambda d_i}(x_i x + y_i y)]dxdy \tag{6-5}$$

Combing equation (6-1) (6-2) and (6-4) into (6-5), we can derive that:

$$U_i(x_i,y_i) = \frac{1}{\lambda^2 d_0 d_i}\exp[i\frac{k}{2d_i}(x_i^2+y_i^2)] \iint \iint_{-\infty}^{\infty} U_0(x_0,y_0)t(x,y) \times \exp\left[i\frac{k}{2}\left(\frac{1}{d_0}+\frac{1}{d_i}-\frac{1}{f}\right)(x^2+y^2)\right]\exp\left[j\frac{k}{2d_0}(x_0^2+y_0^2)\right] \times \exp\left[-i\frac{2\pi}{\lambda d_0}(x_0 x + y_0 y)\right] \times \exp[-i\frac{2\pi}{\lambda d_i}(x_i x + y_i y)]dxdy\, dx_0 dy_0 \tag{6-6}$$

This equation is very similar to equation (4-13) in Chapter 4, which described the diffraction pattern obtained using a geometric mask, only with an extra component $t(x,y)$ which presents the complex amplitude transmittance of the CGH. Therefore, the simplification method is similar. Component $\exp[i\frac{k}{2d_i}(x_i^2+y_i^2)]$ can be neglected since it does not affect intensity. Due to the relatively small change in phase, we can also assume that:

$$\exp\left[j\frac{k}{2d_0}(x_0^2+y_0^2)\right] \approx \exp[i\frac{k}{2d_0}(\frac{x_i^2+y_i^2}{M^2})] \tag{6-7}$$

Where M=$\frac{d_i}{d_0}$ is the magnification factor. Thus, the factors with x_0 and y_0 can be simplified. Using the thin lens equation in Geometric optics.

$$\frac{1}{d_0}+\frac{1}{d_i}-\frac{1}{f}=0 \tag{6-8}$$

The simplified electric field diffraction pattern U_i can be calculated as:

$$U_i(x_i,y_i)=\frac{1}{\lambda^2 d_0 d_i}\iint_{-\infty}^{\infty}\left\{\iint_{-\infty}^{\infty}U_0(x_0,y_0)\exp\left[-i\frac{2\pi}{\lambda d_0}(x_0x+y_0y)\right]dx_0dy_0\right\}\times$$

$$t(x,y)\exp[-i\frac{2\pi}{\lambda d_i}(x_ix+y_iy)]\,dxdy$$

$$=\frac{1}{\lambda^2 d_0 d_i}\iint_{-\infty}^{\infty}G_0(\frac{x}{\lambda d_0},\frac{y}{\lambda d_0})t(x,y)\times\exp[-i\frac{2\pi}{\lambda d_i}(x_ix+y_iy)]\,dxdy \tag{6-9}$$

where G_0 is the Fourier transformation of U_0. This is the diffraction pattern at U_i in this optical system. If the complex amplitude transmittance of the CGH is neglected, an equation can be derived as:

$$\frac{1}{\lambda^2 d_0 d_i}\iint_{-\infty}^{\infty}G_0(\frac{x}{\lambda d_0},\frac{y}{\lambda d_0})\times\exp[-i\frac{2\pi}{\lambda d_i}(x_ix+y_iy)]\,dxdy=\frac{1}{M}U_0(-\frac{x_i}{M},-\frac{y_i}{M}) \tag{6-10}$$

Which is exactly same as the result in equation (4-16), this is a revised pattern of the given shape with a magnification factor M=$\frac{d_i}{d_0}$. If $\tilde{h}$ is defined as the Fourier transformation of $t(x,y)$:

$$\iint_{-\infty}^{\infty}t(x,y)\exp\left[-i\frac{2\pi}{\lambda d_i}(xx_i+yy_i)\right]dxdy=\tilde{h}(x_i,y_i) \tag{6-11}$$

Using Convolution Theorem at equation (6-9), the complex amplitude at the imaging plane can be expressed as:

$$U_i(x_i, y_i) = \frac{1}{M} U_0\left(-\frac{x_i}{M}, -\frac{y_i}{M}\right) * \tilde{h}(x_i, y_i)$$

$$= \iint_{-\infty}^{\infty} \frac{1}{M}\left(-\frac{\tilde{x}_0}{M}, -\frac{\tilde{y}_0}{M}\right) \tilde{h}(x_i - \tilde{x}_0, y_i - \tilde{y}_0) d\tilde{x}_0 d\tilde{y}_0 \quad (6\text{-}12)$$

Equation (6-12) shows the complex amplitude at imaging plane is the result of convolution the geometric pattern and the Fourier transformation of the CGH.

Convolution is a mathematical operation on two functions to produce a third function, that is typically viewed as the modified original function, giving the integral of the pointwise multiplication of the two functions as a function of the amount that one of the original function is translated. A schematic of convolution is shown in Figure 6.2. In this case, the square or star beam shape can be regarded as the original objective function and the Fourier transformation can be regarded as the impulse response of the original function, thus a pattern with multiple shaped beams can be created. For instance, if a square shape is applied on the first SLM and a CGH of three separated points is applied on the second SLM, the diffractive pattern on the imaging plane will be three separated square points with the same intensity distribution as the object. This is the theoretical basis of the following research.

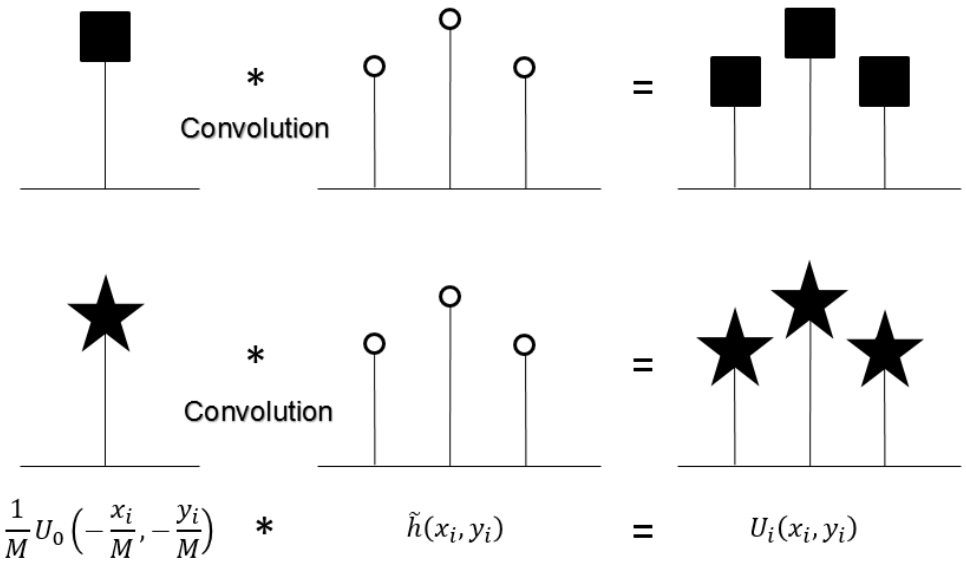

Figure 6.2 Schematic of convolution for parallel beam shaping

6.3 Experimental setup

6.3.1 Overall setup

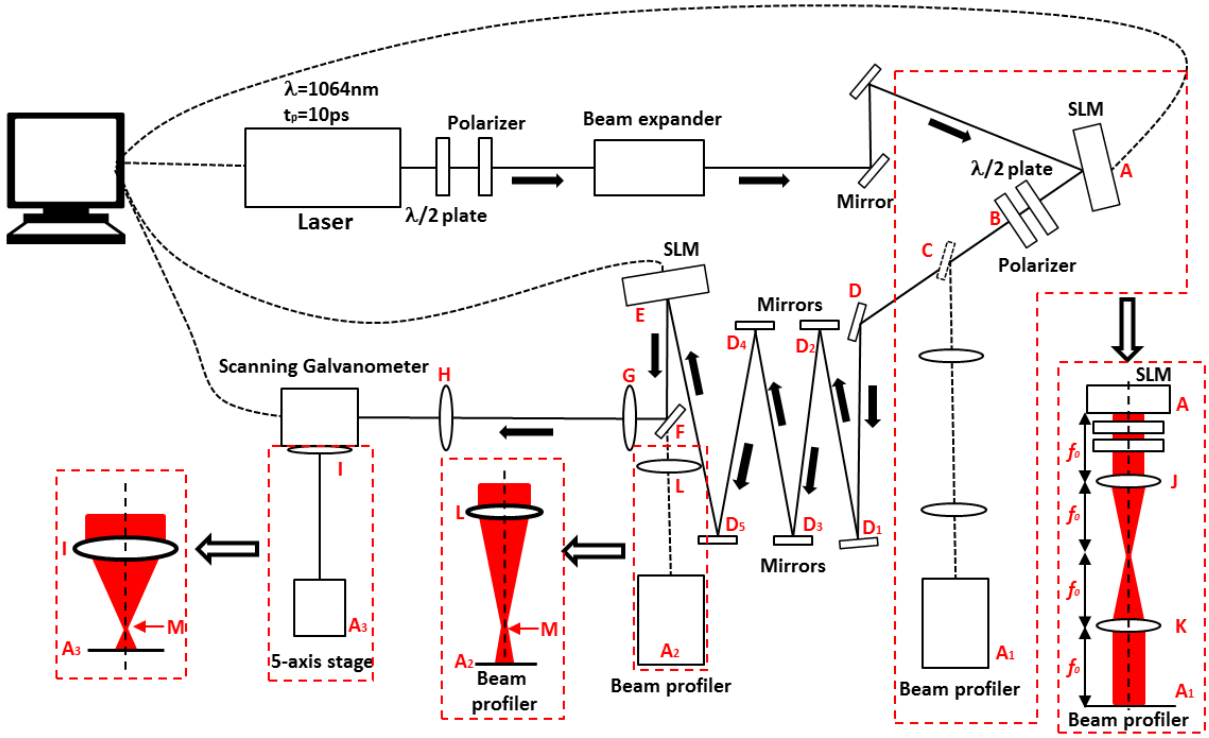

Figure 6.3 Experimental setup

A schematic of the experimental setup is shown in Figure 6.3. The ultrafast laser system used for this research is a custom made Nd:VAN seeded regenerative amplifier laser system(High-Q IC-355-800ps, Photonic solutions) as described in Chapter 3. A 45° linear polarized laser beam output (beam diameter: Dia.≈2.7mm, pulse duration: *tp*=10ps, wavelength: λ=1064nm, and repetition: *f*=10kHz) passes through a half wave plate and polarizer used for adjusting power and polarization direction, a beam

expander(M≈×3) and two plane mirrors for controlling the beam path, and illuminated on the first reflective, liquid crystal SLM (Hamamatsu X13139).

The SLM contains a parallel-aligned crystal liquid layer. An active matrix circuit is formed on the silicon substrate for applying voltages to pixel electrodes. Phase of the incident light can be modulated by aligning the polarization of the incident light in the same direction as the orientation of the liquid crystal. A polarization analyser was placed after the first SLM to modulate the laser beam intensity.

When observing the beam profile after shaping, the beam was reflected by a flip mirror and passed through a 4f system with two positive lenses (focal length: f_o=200mm) to reach a CCD camera based on a beam profiler (Thorlabs). When processing, the flip mirror was removed, and the beam traversed a long distance by multiple reflected mirrors to reach the second SLM (Hamamatsu X10468).

After the second SLM, the beam was reflected by a flip mirror and reached a scanning galvanometer, and a focusing lens ($f_{f\text{-}\theta}$=100mm). Machining samples were mounted on a five-axis (*x,y,z,u,v*) motion control stage, placed under the *f*-theta lens. When observing the beam profile after splitting, the flip mirror was removed from the optical alignment to let the beam passed through a positive lens (focal length: f_o=750mm) to reach the second CCD camera (Spiricon) which is placed at the image plane of the beam path.

6.3.2 Beam shaping using a Hamamatsu X10468 SLM

The setup of the intensity modulation system contains a 45° linear polarized incident laser beam, a Hamamatsu X10468 SLM, a half wave plate and a polarizer. The setup can be expressed as a Jones vector noted *J(x,y)*, where x and y are the horizontal and vertical coordinates across the beam profiles. A full derivation using the optical properties of the setup gives:

$$J(x,y) = \begin{pmatrix} 1 & 0 \\ 0 & 1 \end{pmatrix} \times \begin{pmatrix} cos2\theta & sin2\theta \\ sin2\theta & -cos2\theta \end{pmatrix} \times \begin{pmatrix} e^{i\emptyset(x,y)} & 0 \\ 0 & 1 \end{pmatrix} \times \begin{pmatrix} \sqrt{2} \\ \sqrt{2} \end{pmatrix} \quad (6\text{-}13)$$

Where $\emptyset(x,y)$ is the phase delay induced with the first SLM, and θ is the angle of the fast axis of half wave plate. The intensity of the output can be derived from Equation (6-14):

$$I = \frac{1}{2}\begin{pmatrix} cos2\theta e^{-i\times\emptyset(x,y)} + sin2\theta & 0 \end{pmatrix} \times \begin{pmatrix} cos2\theta e^{i\times\emptyset(x,y)} + sin2\theta \\ 0 \end{pmatrix}$$

$$= \frac{1}{2} + \frac{1}{2} sin4\theta cos\emptyset \quad (6\text{-}14)$$

where I is the transmission efficiency, when I = 1, laser beam passed through the polarizer without energy loss, when $I = 0$, the polarizer blocked all the energy. As shown in Equation (6-14), when $\theta = \frac{3}{8}\pi$, $I = \frac{1}{2} - \frac{1}{2}cos\emptyset$, which means using this method, the output intensity can be adjusted from 0 to 1 (same as the incident beam).

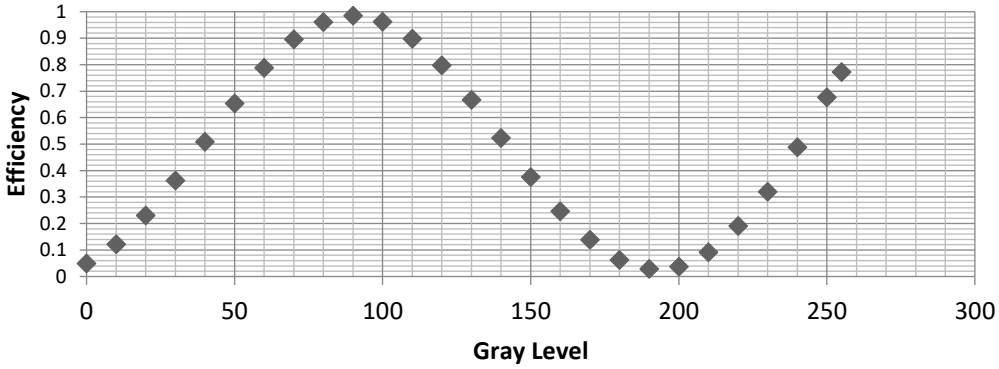

Figure 6.4 Efficiency versus gray level

6.3.3 Outline shape and intensity distribution design

Both the binary and gray level masks were created and applied on the first SLM. With a binary mask, the outline of the input beam can be changed into any required shape, while the intensity distribution will remain same as the original distribution. Furthermore, with a gray level mask, the intensity distribution can be modified. For example, if the target beam has a flat top distribution and the intensity is set as (Y). In order to obtain a flat beam profile, the required intensity (Y) should be proportional to the result of the transmission efficiency (I) multiplied by original intensity distribution (O) which is taken by a beam profiler and edited using Matlab.

$$Y = \alpha \times I \times O \tag{6-15}$$

Where α is a factor to normalize the required intensity (Y) between 0 and 1.

The equation for (R) can be derived from Figure 6.4:

$$\mathrm{I} = \frac{1}{2} - \frac{1}{2}\cos\left(\frac{2\pi}{190} \times [GL]\right) \quad (6\text{-}16)$$

Where [GL] is the gray level of a given point in the 300 ×300 matrix and the value is displayed on the SLM. By combining equation (6-15) and (6-16), we can derive:

$$[GL] = \frac{190}{2\pi}\arccos\left[\left(\frac{[\mathrm{Y}]}{\alpha[\mathrm{O}]} - \frac{1}{2}\right) \times 2\right] \quad (6\text{-}17)$$

Based on equation (6-16), an intensity mask which can shape the original beam into a flat top distribution is created.

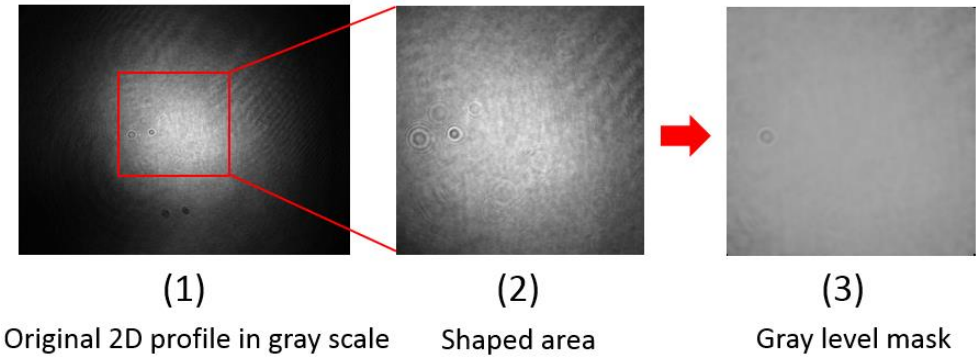

Figure 6.5 Original and shaped beam profile

As shown in Figure 6.5, the original beam profile was taken by a beam profiler and read using Matlab. Figure 6.5 (2) shows the square shaped area which has a side length of 300 pixels (≈2mm) and Figure 6.5 (3) shows the gray level mask calculated by pixels based on Equation (6-16). By applying the gray level mask on the SLM, a flat top beam can be achieved.

6.3.4 Beam splitting using a SLM

Diffractive multi-beam patterns are generated using a second spatial light modulator (Holoeye LC-R2500), on which computer generated holograms (CGHs) are displayed. An iterative Fourier-transform algorithm calculated by a provided Hamamatsu software called Lcos-control has been applied and created for multi-beam output.

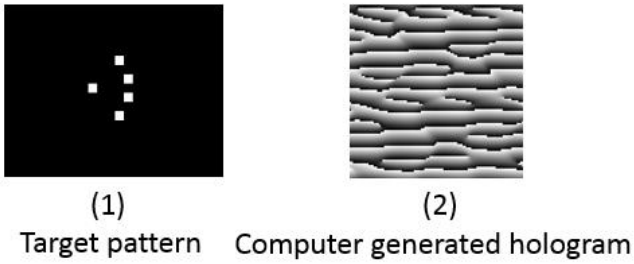

Figure 6.6 Target pattern and its CGH

As shown in Figure 6.6 (1), a pattern of five points was input into the Lcos-control software and a hologram was generated. By applying this hologram on the second SLM, an output of five spots will be generated at the focal plane after passing the focusing lens. In this case, the spots will retain the shape and intensity distribution.

6.3.5 Shaping reconstruction at the imaging plane of a focusing lens

Similar to the method presented in Chapter 4 and Chapter 5, a long beam path was created. As shown in Figure 6.3, there are five mirrors, D_1-D_5, added into the beam path to significantly increase the distance from the first SLM to the focusing F-theta

lens, i.e. the object distance. The purpose of this was to reconstruct the shape to a small size comparable to the beam waist. The position of the imaging plane A_3 can be calculated, based on the thin lens imaging equation below,

$$\frac{1}{u}+\frac{1}{v}=\frac{1}{f} \tag{6-18}$$

Where, $u \approx 4300mm$ is the object distance, i.e. the distance from the first SLM(A) to the F-theta lens (I), $f = 100mm$ is the focal length of the F-theta lens and v is the image distance, i.e. the distance from the F-theta lens (G) to image plane(A_3)

$$v = \frac{fu}{u-f} \approx 102.04\text{mm} \tag{6-19}$$

$$d = v - f = 2.04\text{mm} \tag{6-20}$$

The magnification factor of this system is M≈1/45. When a 300 pixel side length mask was applied, the original expanded size was approximately 2mm. The diameter of reconstructed beam at A_3 can be calculated to be approximately 41μm. The objective distance in this research is 4300mm, while it in Chapter 3 and 4, the distance is 15000mm. This is due to the much larger pulse energy (maximum≈ 0.1mJ) of the High-Q laser, which makes the average power sufficient for a larger shaping area.

Since both the shape and interference pattern need to be observed, a similar method is used at a second beam profiler A_2. A positive lens (focal length: f_o=750mm) was placed after the second SLM and a beam profiler was placed at the imaging plane.

6.4 Results and discussion

6.4.1 Beam shaping results observed by CCD Cameras at A_1 and A_2

As shown in Figure 6.7 and Figure 6.8, the first line shows the results of beam outline shaping using the first SLM. By applying a square or a star shape binary mask, the corresponding beam shape can be observed at A_1. The binary mask only shaped the outline profile but left the inside intensity distribution unchanged. The second line showed the results of beam splitting. A square shape beam was separated into four in Figure 6.6, while a star shape beam was separated into five in Figure 6.7. Both outputs have similar shape and intensity distribution as their input beam, the intensity of their central area was higher than other area due to the Gaussian nature of the original beam.

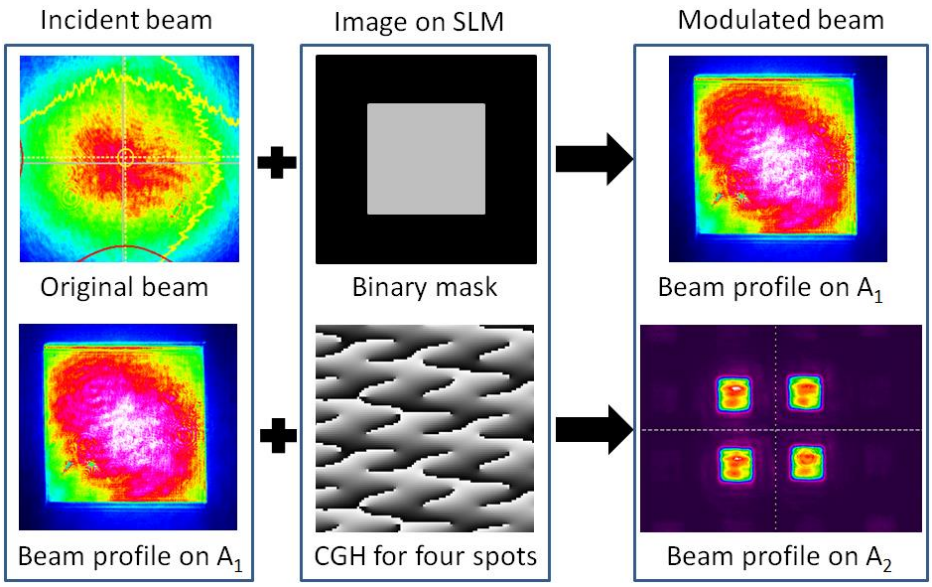

Figure 6.7 Four square beam. First line: the original distribution plus a binary mask to achieve a square shape beam at A_1. Second line: the square shape beam plus CGH to achieve four square beams at A_2.

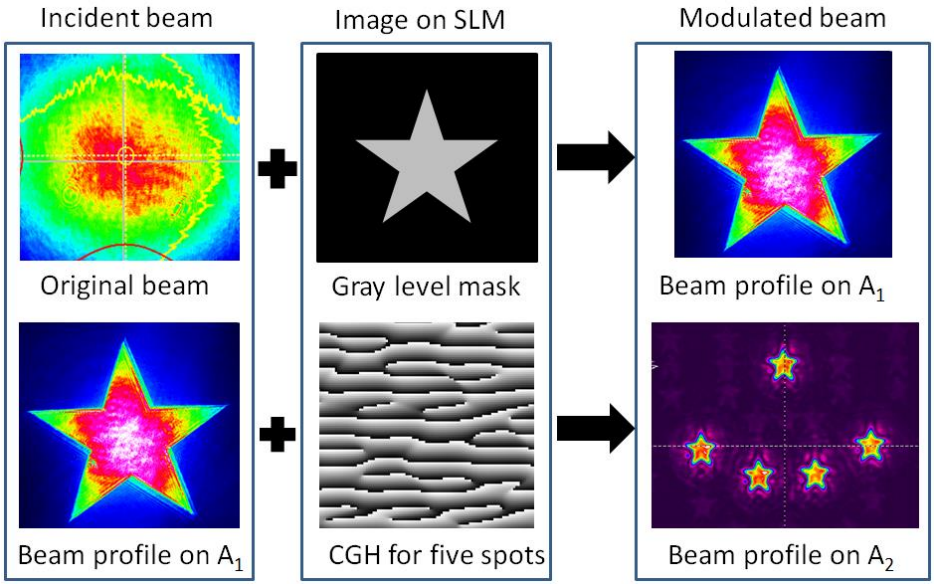

Figure 6.8 Five star shape beam. First line: the original distribution plus a binary mask to achieve a star shape beam at A_1. Second line: the square shape beam plus CGH to achieve three star beams at A_2.

Figure 6.9 compares the results between using a binary mask and a gray level mask. Figure 6.9 (1) shows an output modulated by a binary mask and shaped into a square shape. However, the intensity distribution was still similar to original Gaussian distribution at both beam profiler A_1 and A_2. Figure 6.9 (2) shows an output modulated by a gray level mask. Using a gray level mask on the first SLM, both the outline profile and intensity distribution are modulated, and a square flat top beam was created and separated into three beamlets.

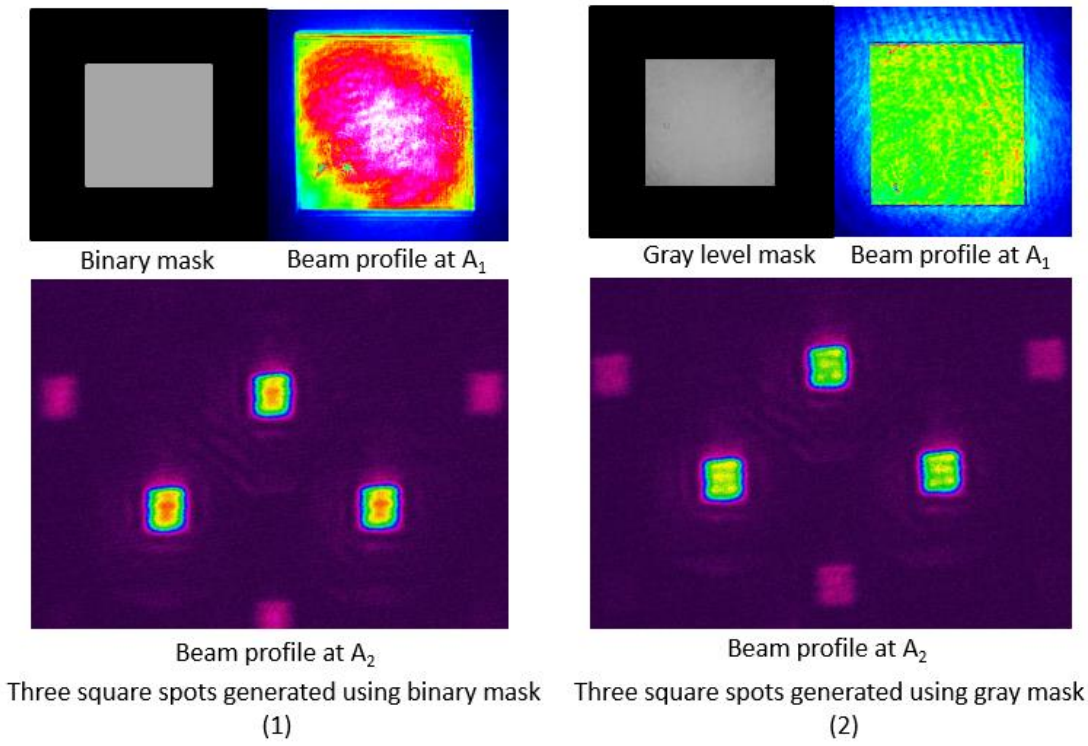

Figure 6.9 Comparison between a binary mask and gray level mask

There are also some ghost patterns can be seen in beam profile A_2. This is the higher

order of the diffractive patterns created by the CGH, which energy intensity is lower than the ablation threshold of the metal samples.

6.4.2 Beam shaping machining results at A_3

Figure 6.10 shows the machined footprints of multi beams with the shape of a star and a square. The beam was shaped by a binary mask on first SLM, and then separated into multi beams using a second SLM. Finally the beam reached the F-theta lens and processed at the imaging plane of the optical system. Footprints were fabricated on a polished titanium sample. The input laser energy (Ep) was approximately 10μJ, measured before the scanning galvanometer aperture. Since the laser frequency was *F*=10KHz and the drilling time for each pattern was 1s, ≈10k pulses were used to fabricate each footprint. As shown in Figure 6.10, the shape of footprints matched the beam profile very well. The side length of the square of was 300pixel (≈1.94mm) and the magnification factor system was 1/45. The theoretic side length of the machined footprints was 43μm, while the side length of footprint in the second line of Figure 6.10 was approximately 40μm, which was very close to the calculated value.

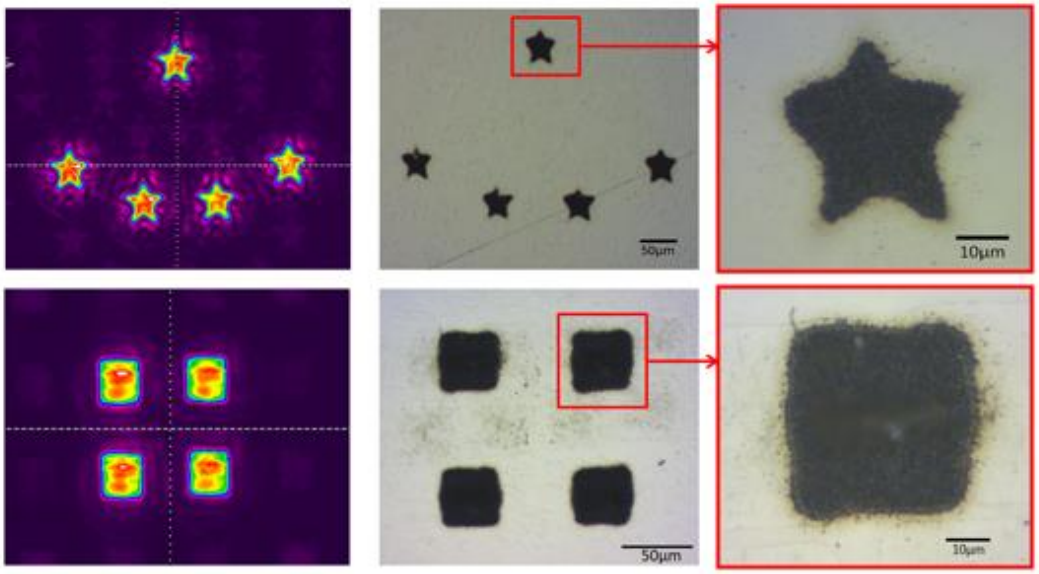

Figure 6.10 Beam shaping and machining results. First line: profile of five stars and machined patterns. Second line: profile of four squares and machined patterns.

Footprints machined with gray level mask were observed using a white light interferometer (WYKO), and a pattern with the same shape but a binary mask was also observed for comparison. As shown in Figure 6.11, the footprints fabricated by binary masks showed an approximately Gaussian-shaped bottom indicating that the inside beam intensity distribution was unshaped, while the footprints fabricated by gray level mask showed a relatively flat bottom. This demonstrated a good match between the footprint shapes machined at imaging plane at A_3 and beam shapes observed at A_1 and A_2.

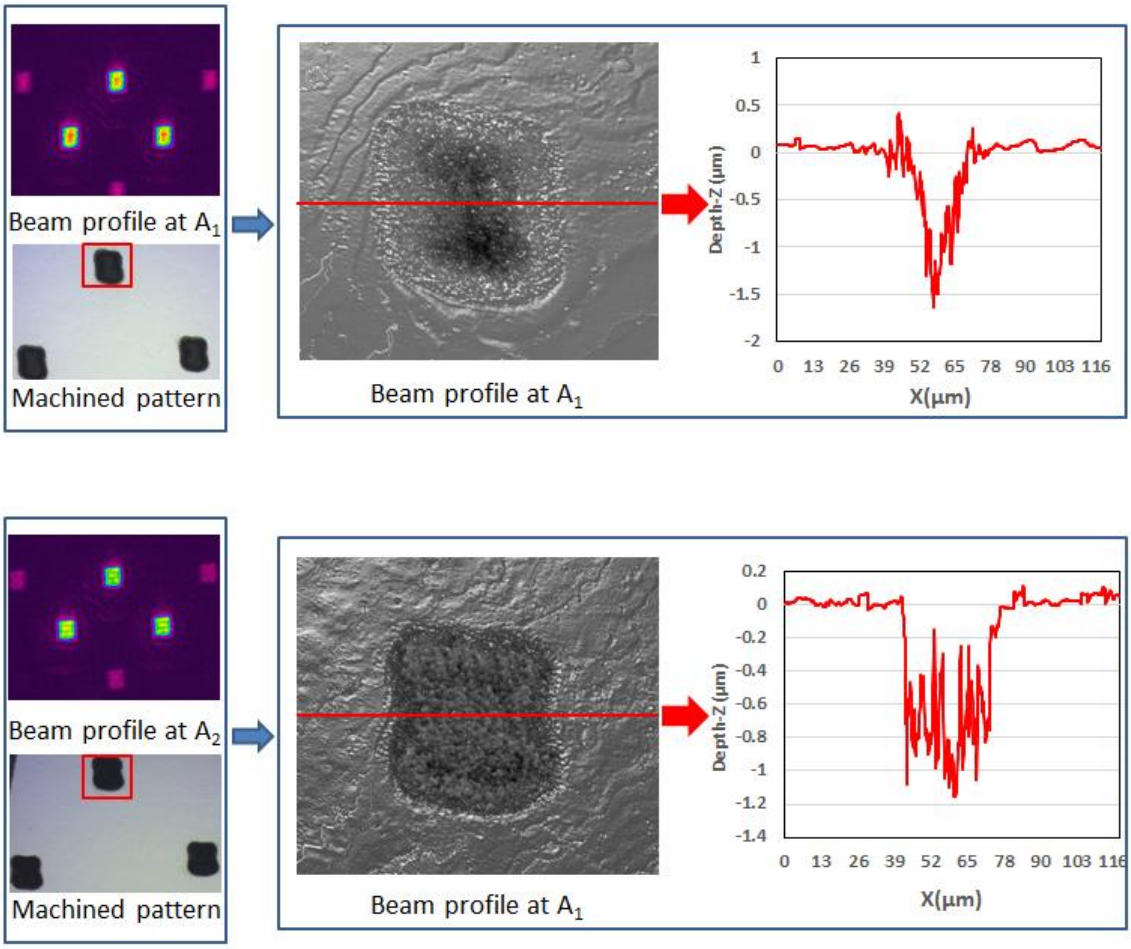

Figure 6.11 Comparison between using binary and 256 gray level masks. Top: binary mask. Bottom: gray level mask

6.4.3 Shaping efficiency versus the size of mask

In the process of beam shaping, a certain amount of energy will be blocked out due to the image applied on the first SLM. The shaping efficiency and quality may change when varying the size of geometric mask. Figure 6.12 shows both binary and gray level mask shaped beam profile observed at A_1 when varying the size of mask (side length varied from 150 to 500 pixels).

To quantitatively investigate the beam shaping efficiency and quality, images of the shaped beam profile observed at A_1 were analysed by MATLAB. As shown in Figure 6.13, the gray level beam profile was read using MATLAB and each pixel was valued from 0 (no power) to 1 (max power). The method to quantify the intensity value of a tiny area (3×3 pixels) was demonstrated in Figure 6.13. Accordingly, an entire shaped area matrix can be extracted. Shaping efficiency can be calculated using the equation below:

$$\eta = \frac{\iint I_{shaped} dxdy}{\iint I_0 dxdy} \tag{6-21}$$

where $\iint I_{shaped} dxdy$ is the integral of the shaped beam intensity profile and $\iint I_0 dxdy$ is the integral of the original beam intensity profile obtained at A_1. This calculation of efficiency was based on real beam profile and carried out using MATLAB, and the efficiency was also measured using a power meter.

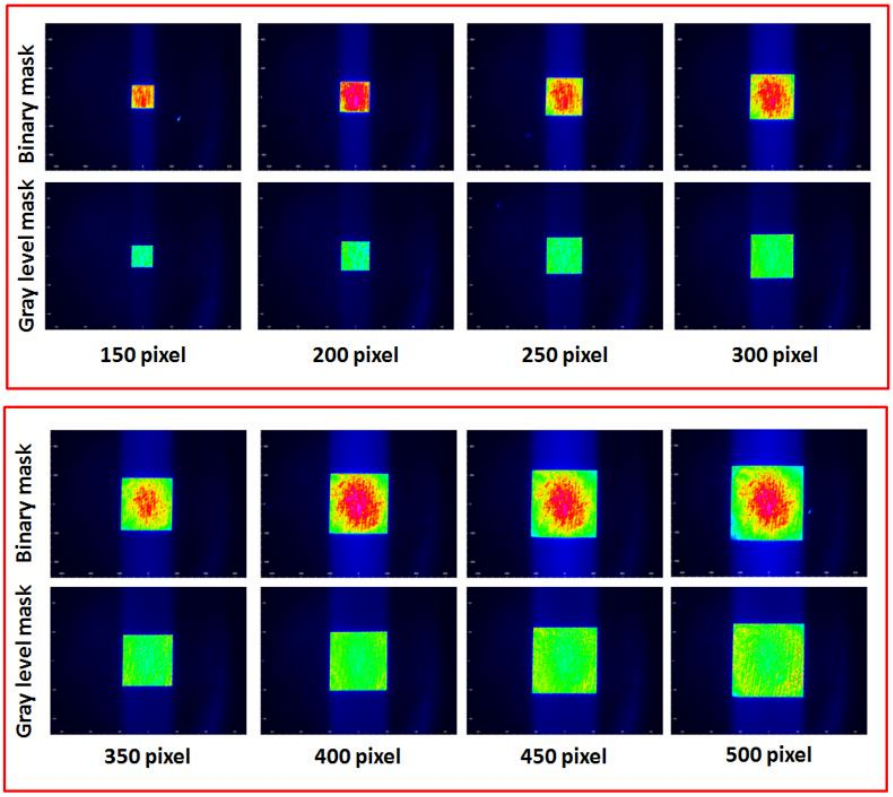

Figure 6.12 Shaping by binary and gray level mask by vary mask size (side length of mask varied from 150 to 500 pixels).

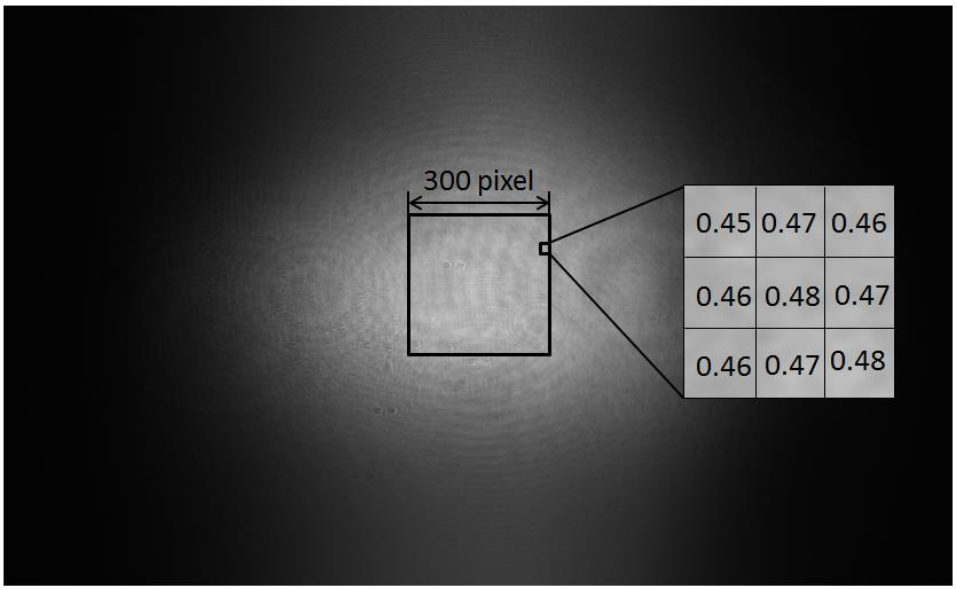

Figure 6.13 Analysis of shaped beam profile observed at A_1

Figure 6.14 shows the comparison between the calculated value and measured value using a binary mask. The shaping efficiency becomes higher when the size of mask is larger. The measured value is very close to calculated value, indicating good shaping quality and accuracy.

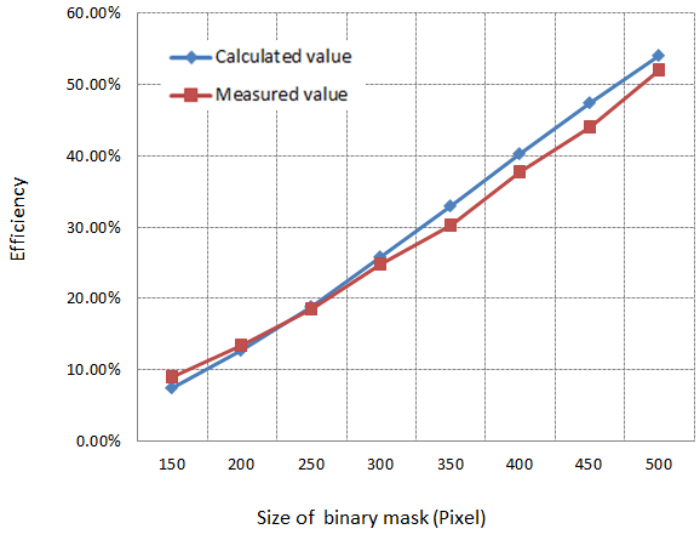

Figure 6.14 Shaping efficiency against the size of a binary mask

Figure 6.15 shows the comparison between calculated value and measured value using a gray level mask. The calculated values are higher than measured values due to the limitation of the shaping ability and original distribution. As shown in Figure 6.16, when calculating the efficiency, a target intensity is chosen and all pixels in the shaped area are set as the target intensity. However, if the target intensity is too high or the shape is too large, the intensity at the edge could already be lower than the target intensity, which explains the difference between measured and calculated

efficiency.

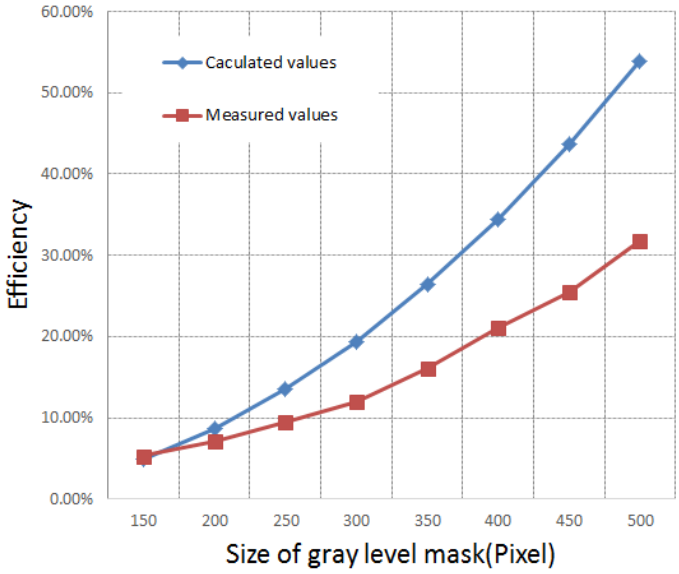

Figure 6.15 Shaping efficiency against the size of a gray level mask

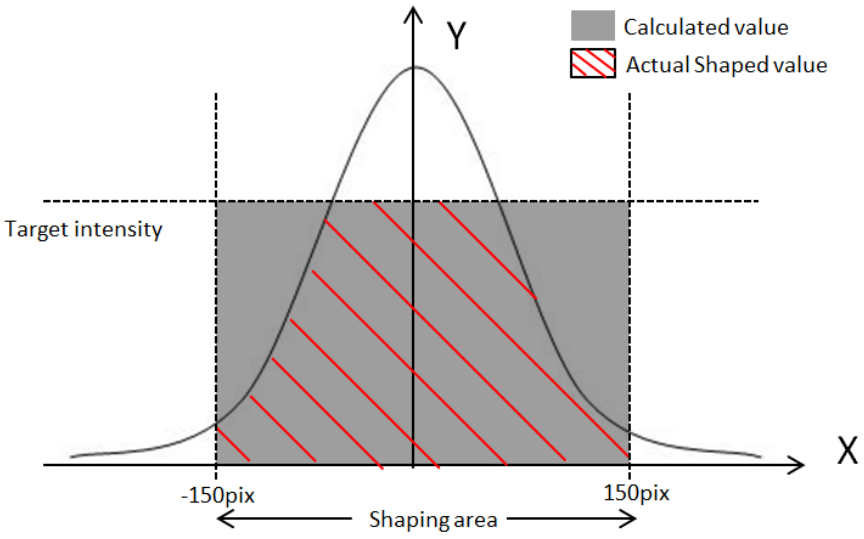

Figure 6.16 Shaping area

6.5 Summary

A novel ultrashort pulse laser beam-shaping technique to generate multiple geometric beams was demonstrated in this chapter. Binary and gray level masks applied on spatial light modulator (SLM) were used to shape the outline profile and intensity distribution of the incident laser beam. After a long beam path, a second SLM was used to separate the incident beam into multiple beamlets. A laser beam was effectively converted to a target shape, intensity distribution and separated pattern. A polished titanium sample was machined by the shaped beam at the imaging plane. The machined footprints have the corresponding shape and separated patterns. The size of the footprint can be adjusted from the mask and is comparable to the beam waist at the focal plane. The depth distribution also matches the designed intensity distribution very well.

Chapter 4, 5 and 6 have presented a novel beam shaping technique for material processing. Precise control of outline profiles, intensity distributions and diffractive patterns can be achieved by applying geometric gray level masks on SLMs. Compared with diffractive beam shaping method at focal plane, image-based processing has advantages in flexibility, as it can generate arbitrary shapes and intensity distributions. This provides some potential applications for this technique.

For example, a flat-top beam can be used in thin film processing due to the well-

defined ablation threshold of each layer. With a proper power intensity, a flat-top beam is capable of removing the top layer without damaging the substrate. Compared to a traditional circular beam, a square beam may generate a more uniform processed edge at a low pulse overlap rate due to the larger overlap area of two pulses. Additionally, a laser beam with a step distribution (see Figure 5.18) could also be used for multiple laser processing, since each layer has its unique ablation threshold and an accurately shaped beam can reach all the required intensities at same time.

This technique can also be applied to the generation of laser induced periodic surface structures (LIPSS). LIPSS can be created on the surface of a material when the fluence of irradiation approaches the damage threshold of the material. The unifom of LIPSS structure is affected by fluence of the incident laser. A flat-top laser could generate more uniform LIPSS, leading to a purer colour diffraction. Other intensity distributions such as a step and a slope may also lead to some unique structures of periodic patterns, which could be potentially used in security data encoding.

Chapter 7 Conclusions and future work

7.1 Conclusions

In this thesis, a novel beam shaping technique for material processing has been presented. By applying gray level geometric masks on spatial light modulators (SLMs), arbitrary shapes and distributions of a laser beam were obtained at the objective plane and reconstructed at the imaging plane on metal surfaces.

Simple and direct geometric binary masks were applied on a SLM (Holoeye LC-R2500) to shape the input beam. Arbitrary beam shapes with steep sides and Gaussian distribution were obtained at the imaging plane. In order to have sufficient intensity at the imaging plane, a long objective distance (~15000m) was built to minimize the distance between the focal plane and the imaging plane. The size of the beam ($\sim 20\mu m$) was comparable to the beam waist at the focal plane. A polished stainless-steel sample was machined by the shaped beams. The shape of machined footprints well matched the corresponding masks. Both shaping quality and efficiency varied when changing the size of input beam. Smaller masks size gave a better shaping quality due to the shaping ability of the SLM, however, they decreased the shaping efficiency. Depending on the input beam diameter, an appropriate mask size should be selected to keep a good balance between the shaping quality and efficiency. Using this technique, arbitrary beam shapes can be obtained simply by applying geometry masks with corresponding shapes and a complex Fourier transformation method was avoided,

leading to an improvement in flexibility. However, the intensity distribution remained the Gaussian distribution as for the incident beam, resulting in the footprints having uneven depth.

In order to control both the outline profile and intensity distribution of a laser beam, geometric gray level mask were employed. Gray level masks were designed according to the original beam profile and the shaping ability of the SLM (Holoeye LC-R2500). A near Gaussian beam was shaped into a round and square flattop both with uniform intensity. A polished titanium sample was machined by the shaped beam at the imaging plane. The machined footprints had the corresponding shapes and depth distributions of the laser beam. An algorithm has also been developed using Matlab for generating high quality gray level masks. Besides Gaussian and flat-top, arbitrary distributions such as a slope, steps and a bowl distribution were obtained using this method. This technique showed a significant improvement in shaping accuracy and flexibility due to the much higher shaping ability of the calculated gray level masks.

Additionally, the beam shaping technique was combined with parallel processing. Two SLMs were employed to shape the laser beam at the objective plane, and separate the beam into desired patterns. The diffractive pattern at the imaging plane was calculated to be the result of the convolution of the geometric pattern and the Fourier transformation of the CGH. Binary and gray level masks applied on the SLM

(Hamamastu X10468) were used to shape the outline profile and intensity distribution of the incident laser beam. After a long beam path, a second SLM (Holoeye LC-R2500) was used to separate the incident beam into multiple beamlets. A laser beam was effectively converted to target shape, intensity distribution and a separated pattern. A polished titanium sample was machined by the shaped beam at the imaging plane. The machined footprints had the corresponding shape and separated patterns. The depth distribution also matches the designed intensity distribution very well. Due to a parallel aligned nematic liquid crystal design for Hamamastu X10468 SLM, the shaping ability can reach maximum, which means arbitrary intensity distribution can be obtained from any original intensity distribution theoretically. This technique allows material processing using accurate and flexible shaped beams at a relatively high efficiency.

A flap-top beam has natural advantages for many applications, such thin film processing [63], laser printing [62], material annealing [64] and laser welding with improved weld quality and repeatability [66] due to the same interaction over the illuminated area. Among these applications, thin film processing particularly needs a good shaping quality and accuracy due to the well defined ablation threshold of each layer. Using this beam shaping technique, a uniform flat top beam can be generated at any given intensity, which matches the requirements of thin film processing very well. Additionally, using a calculated gray level mask, a step distribution with several

intensity stages can be obtained. This could potentially be used in multiple layer material processing, since each layer has its unique ablation threshold and an accurately shaped laser beam can reach all the required intensity at same time, which could significantly improve the processing efficiency.

This technique can also be applied to the generation of laser induced periodic surface structure (LIPSS). LIPSS can be created on the surface of a material when the fluence of irradiation approaches the damage threshold of the material. These have been widely investigated in many research areas, such as metallic surface wettability modification, either hydrophobic or hydrophilic [118], chemical etching rate control for microfluidic applications, reduction of friction coefficient of metal surfaces for tribological application [119], and large surface area biosensors applications [120, 121]. The uniform of LIPSS structure is affected by the fluence of incident laser. Metal surface could be further improved by using a flattop beam, which produce more uniform LIPSS structures, which could lead to a purer colour diffraction. Using other intensity distribution of a laser beam could also lead to some special structures of periodic patterns, which could be potentially used in security data encoding.

7.2 Recommendations for future work

The shaping system could be further improved to be more dynamic and user friendly. The size of shaped beam is comparable to the beam waist at focal plane, which allows

this technique to generate very small textures at a high accuracy. Therefore, the gray level mask can also be regarded as a mold to print required patterns onto metal surfaces. If all the masks are arranged at a certain order and displayed automatically, a series combination of patterns could be generated rapidly, which would be potentially used in anti-counterfeiting. This technique would also take the micro processing efficiency and flexibility to a new level.

Finally, a real-time feedback system would also be worth developing. Although a gray level mask is generated based on real beam profile, it will not always be effective since a laser source cannot always be stable, the intensity distribution would vary during time. Therefore, if the feedback system is employed, the beam profiler will sense the change of incident beam and modulate the gray level mask automatically, and the stability of beam shaping system would be improved.

References

[1] A. Einstein, "Zur Quantentheorie der Strahlung," *Physikalische Zeitschrift,* vol. 18, pp. 121-128, 1917.

[2] T. Maiman, "Stimulated optical radiation in ruby," *Nature,* vol. 187, no. 4736, pp. 496-494, 1960.

[3] F.M.Dickey, Laser Beam Shaping:Theory and Techniques, New York: CRC press, 2014.

[4] G.W.Gruhlke, L.Giammona, C.Langhorn, K.J.Kanzler and J.Kedmi, "Medical and industrial laser beam shaping by diffractive optical elements," *Proceedings of SPIE,* no. 1, pp. 120-129,10, 1993.

[5] K.Jain, "Lithography and photoablation systems for microelectronics and optoelectronics: Importance of laser beam shaping in system design," *Proceeding of SPIE4770,* pp. 1-12, 2002.

[6] E.P.Walker and T.D.Milster, "Beam shaping for a high-power vertical cavity surface emitting laser," *Proceeding of SPIE4443,* pp. 105-114, 2001.

[7] Z.Kuang, W.Perrie, D.Liu, S.P.Edwardson, J.Cheng, G.Dearden and K.Watkins, "Diffractive multi-beam surface micro-processing using 10ps laser pulses," *Applied Surface Science 255,* pp. 9040-9044, 2009.

[8] B. Frieden, "Lossless conversion of a plane laser wave to a plane wave of uniform irradiance," *Appl.Opt.,* vol. 4, no. 11, pp. 1400-1403, 1965.

[9] "Coherent light optical system yielding an output beam of desired intensity distribution at a desired equiphase surface". U.S. Patent 3476463, Nov. 1969.

[10] J. Curtis, B. Koss and D. Grier, "Dynamic holographic optical tweezers," *Optics Communications,* vol. 207, pp. 169-175, 2002.

[11] G. Dearden, Z. Kuang, D. Liu, W. Perrie, S. Edwardson and K. Watkins, "Advances in ultra short pulse laser based parallel processing using a spatial light modulator," *Physic Procedia,* vol. 39, pp. 650-660, 2012.

[12] S. Hasegawa and Y. Hayasaki, "Holographic Femtosecond Laser Processing with Multiplexed Phase Fresnel Lenses Displayed on a Liquid Crystal Spatial Light Modulator," *Optical review,* vol. 14, p. 208, 2007.

[13] F. Dickey and S. Holswade, "Laser Beam Shaping: Theory and Techniques.," New York, Marce Dekker, 2000.

[14] W. M. Steen and M. Jyotirmoy, in *Laser Materials Processing*, Springer, 2010, p. 11.

[15] "Stimulated emission," Widipedia, [Online]. Available: https://en.wikipedia.org/wiki/Stimulated_emission. [Accessed 1 6 2018].

[16] X. Liu, D. Du and G. Mourou, "Laser Ablation and Micromachining with," *IEEE Journal of Quantum Electronics,* vol. 33, pp. 1706-1716, 1997.

[17] W. Lamb, "Theory of an Optical Maser," *Phys. Rev,* vol. 134, no. 6A, pp. A1429-A1450, 1964.

[18] L. Hargrove, R. Fork and M. Pollack, "Locking of HeNe Laser Modes Induced by Synchronous Intracavity Modulation," *Appl. Phys. Lett,* vol. 5, no. 1, p. 4, 1964.

[19] R. Paschotta, "RP Photonics Encyclopedia - mode locking," [Online]. Available: https://www.rp-photonics.com/mode_locking.html.

[20] C. Rulliere, Femtosecond Laser Pulses - Principles and Experiments, New York: Springer-Verlag, 2005.

[21] M. Ueaska, Femtosecond Beam Science, London: Emperial College Press, 2005 .

[22] U. Keller, "Recent developments in compact ultrafast laser," *Nature,* vol. 424, pp. 831-838, 2003.

[23] "Encyclopedia of Laser Physics and Technology," [Online]. Available: https://www.rp-photonics.com/chirped_pulse_amplification.html. [Accessed 1 6 2018].

[24] D. Strickland and G. Mourou, "Compression of amplified chirped optcial pulses," *Optics Communications,* vol. 56, pp. 217-221, 1985.

[25] M. Perry, B. Shore, R. Boyd and J. Britten, "Multrilayer dielectric gratings: Increasing the power of light," *Science and Technology Review,* vol. 9, pp. 25-33, 1995.

[26] E. Treacy, "Optical pulse compression with diffraction gratings," *IEEE Journal of Quantum Electronics,* vol. 5, pp. 454-458, 1969.

[27] O. Martinez, "Design of high-power ultrashort pulse amplifiers by expansion and recompression," *IEEE Journal of Quantum Electronics,* vol. 23, pp. 1385-1387, 1987.

[28] P. Pronko, S. Dutta, J. Squier, J. Rudd, D. Du and G. Mourou, "Machining of sub-micron holes using a femtosecond laser at 800 nm," *Optics Communications,* vol. 114, pp. 106-110, 1996.

[29] C. Lee, N. Koumvakalis and M. Bass, "Spot-size dependence of laser-induced damage to diamond-turned Cu mirrors," *Apply Physics Letter,* vol. 41, no. 7, pp. 625-627, 1982.

[30] S. Hendow and S. Shakir, "Structuring materials with nanosecond laser pulses," *Optics Express,* vol. 18, no. 10, p. 10188, 2010.

[31] P. Bado, W. Clark and A. Said, "Ultrafast laser micromaching hand book," Official Webpage of Clark-MXR, [Online]. Available: http://www.cmxr.com/Education/Introduction.htm. [Accessed May 2017].

[32] C. Phipps, Laser Ablation and its Applications, Springer Science+ Business Media LLC, 2007.

[33] B. Chichkov, C. Momma, S. Nolte, F. v. Alsvenleben and A. Tunnermann, "Femtosecond, picosecond and nanosecond laser ablation of solids," *Applied Physic A,* vol. 63, pp. 109-115, 1996.

[34] M. Fermann, A. Galvanauskas and G. Sucha, Ultrafast lasers technology and applications, Marcel Dekker, Inc., 2001.

[35] F. Dausinger, "Femtosecond technology for precision manufacturing: Fundamental and technical aspects," *RIKEN Review 50, Focused on Laser Precision Microfabrication (LPM 2002),* pp. 77-82, 2003.

[36] C. Föhl and F. Dausinger, "High precision laser drilling with ultra short pulses - fundamental aspects and technical applications," *Proc. PICALO,* vol. 2, pp. 281-286, 2006.

[37] D. Breitling, C. Föhl, F. Dausinger, T. Konoenko and V. Konov, "Drilling of Metals," *Topics in Applied Physics,* pp. 131-156.

[38] D. O'Shea, Elements of Morden Optical Design, New York: A Wiley-Interscience Publication, 1984.

[39] "Linear, Circular and Elliptical Polarization Animation in a Single Shot," 3 2011. [Online]. Available: https://www.youtube.com/watch?v=Q0qrU4nprB0. [Accessed 1 6 2018].

[40] A. Gerrard and J. Burch, Introduction to matrix methods in optics, New York: Dover Publications, 1994.

[41] U. Efron, "Spatial light modulators for optical computing and imformation processing," *System Sciences,* vol. 1, p. 416, 1989.

[42] N. Huot, N. Sanner and E. Audouard, "Programmable focal spot shaping of amplified femtosecond laser pulses and their application to micromachining," *Proceedings SPIE,* vol. 6400, p. 6400K, 2006.

[43] N. Scanner, N. Huot, E. Audouard, C. Larat and J. Huignard, "Spatial beam shaping of femtosecond laser pulses application to micromachining and photowriting," in *CLEO*, 2005.

[44] N. Scanner, N. Huot, E. Audouard, C. Larat and J. Huignard, "Direct ultrafast laser micro-structuring of materials using programmable beam shaping," *Optics and Lasers Engineering,* vol. 45, no. 6, pp. 737-741, 2007.

[45] A. Jesacher and M. Booth, "Parallel direct laser writing in three dimensions with spatially dependent aberration correction," *Optics Express,* vol. 18, p. 21090, 2010.

[46] C. Mauclair, A. Mermillod-Blondin, N. Huot, E. Audouard and R. Stoian, "Ultrafast laser writing of homogeneous longitudinal waveguides in glasses using dynamic wavefront correction," *Optics Express,* vol. 16, p. 5481, 2008.

[47] Z. Kuang, W. Perrie, D. Liu, P. Fitzsimons, S. Edwardson, E. Fearon, G. Dearden and K. Watkins, "Ultrashort pulse laser patterning of indium tin oxide thin films on glass by uniform diffractive beam patterns," *Applied Surface Science,* vol. 258, pp. 7601-7606, 2012.

[48] Z. Kuang, W. Perrie, J. Leach, M. Sharp, S. Edwardson, M. Padgett, G. Dearden and K. Watkins, "High throughput diffractive multi-beam femtosecond laser processing using a spatial light modulator," *Apply Surface Science,* vol. 255, no. 2284, 2008.

[49] Z. Kuang, D. Liu, W. Perrie, S. Edwardson, M. Sharp, E. Fearon, G. Dearden and K. Watkins, "Fast parallel diffractive multi-beam femtosecond laser surface micro-structuring," *Apply Surface Science,* vol. 255, p. 6582, 2009.

[50] "LCOS-SLM (Optical Phase Modulator) X10468-03," Hamamatsu, [Online]. Available: http://www.hamamatsu.com/jp/en/community/lcos/product/search/X10468-03/index.html?_ga=2.91389016.359586229.1514349033-2024356223.1514349033. [Accessed 20 12 2017].

[51] "Spatial Light Modulators - Discontinued Devices," Holoeye, [Online]. Available: https://holoeye.com/spatial-light-modulators/discontinued-devices/. [Accessed 20 12 2017].

[52] Z. Kuang, "Parallel diffractive multi-beam ultrafast laser," *PhD Thesis,* 2010.

[53] J. Goodman, Introduction to Fourier optics, 2nd ed., New York: McGraw-Hill, 1996.

[54] R. Gerchberg and O. Saxton, "A practical algorithm for the determination of the phase from image and diffraction plane pictures," *Optik,* vol. 35, p. 237, 1972.

[55] J. Liesener, M. Reicherter, T. Haist and H. Tiziani, "Multi-functional optical tweezers using computer-generated holograms," *Optics Communication,* vol.

185, p. 77, 2000.

[56] R. Di Leonardo, F. Ianmi and G. Ruocco, "Computer generation of optimal holograms for optical trap arrays," *Optics Express,* vol. 15, p. 1913, 2007.

[57] T. Haist, M. Schönleber and H. Tiziani, "Computer-generated holograms from 3D-objects written on twisted-nematic liquid crystal displays," *Optics Communications,* vol. 140, pp. 299-308, 1997.

[58] M. Pasienski and B. Demarco, "A high-accuracy algorithm for designing arbitrary holographic atom traps," *Optics Express,* vol. 16, p. 2176, 2008.

[59] Wikipedia, "GS-diagram," [Online]. Available: https://en.wikipedia.org/wiki/File:GS-diagram.png#filelinks. [Accessed 1 6 2018].

[60] Y. Kozawa and S. Sato, "Optical trapping of micrometer-sized dielectric particles by cylindrical vector beams," *Optics Express,* vol. 18, p. 10828, 2010.

[61] M. Duocastella and C. Arnold, "Bessel and annular beam for materials processing," *Laser & Photonics Reviews,* vol. 6, no. 5, pp. 607-621, 2012.

[62] O. Homburg and T. Mitra, "Gaussian-to-top-hat beam shaping: an overview of parameters, methods, and applications," *Proceeding of SPIE,* vol. 8236, p. 7412, 2012.

[63] S. Rung, M. Rexhepi, R. Hellmann and C. Bischoff, "Laserscribing of thin films using top-hat laser beam profiles," *Journal of laser micro nanoengineering,* vol. 8, pp. 309-314, 2013.

[64] M. Miyasaka and J. Stoemenos, "Excimer laser annealing of amorphous and solid-phase-crystrallized silicon films," *Journal of Applied Physics,* vol. 86, no. 10, p. 5556, 1999.

[65] D. Chrisey and G. Hubler, Pulsed laser deposition of thin films, New York: J.Wiley, 1994.

[66] K. Washio, Laser precision microfabrication, Berlin: Springer-Verlag, 2010.

[67] J. Wilson and J. Hawkes, Laser principles and applications, Hertfortshire: Prentice Hall International, 1987.

[68] V. Garcés-Chávez, D. McGloin, H. Melville, W. Sibbett and K. Dholakia, "Simultaneous micromanipulation in multiple planes using a self-reconstructing light beam," *Nature,* vol. 419, no. 6903, pp. 145-147, 2002.

[69] V. Shvedov, A. Rode, Y. Izdebskaya, A. Desyatnikov, W. Krolikowski and Y. Kivshar, "Giant optical manipulation," *Physical Review Letters,* vol. 105, p. 118103, 2010.

[70] D. Zeng, W. Latham and A. Kar, "Optical trepanning with a refractive axicon lens system," *Proceedings of SPIE,* vol. 6290, 2006.

[71] C. Hnatovsky, V. Shvedov, W. Krolikowski and A. Rode , "Materials processing with a tightly focused femtosecond laser vortex pulse," *Optic Letters,* vol. 35, no. 20, pp. 3417-3419, 2010.

[72] Y. Jin, O. Allegre, W. Perrie, K. Abrams, J. Ouyang, E. Fearon, S. Edwardson and G. Dearden, "Wavefront and polarization structuring for shaping the focal fields of ultrashort-puse laser beams," *Optical Express,* vol. 21, no. 21, pp. 25333-25343, 2013.

[73] J. Ouyang, W. Perrie, O. Allegre, T. Heil, Y. Jin, E. Fearon, D. Eckford, S. Edwardson and G. Dearden, "Tailored optical vector fields for ultrashort-pulse laser induced complex surface plasmon structuring," *Optical Express,* vol. 23, no. 10, pp. 12562-12572, 2015.

[74] D. Shealy, "Geometric optics-based design of laser beam shapers," *Optical Engineering,* vol. 42, pp. 3123-3138, 2003.

[75] B. Friden, "Lossless conversion of a plane laser wave to a plane wave of uniform irradiance," *Applied Optics,* vol. 4, no. 11, pp. 1400-1403, 1965.

[76] J. Kreuzer, "Coherent light optical system yielding an output beam of desired intensity distribution at a desired equiphase surface". U.S. Patent 3476463, Nov. 1969.

[77] P. Rhodes and D. Shealy, "Refractive optical systems for irradiance redistribution of collimated radiation: their design and analysis," *Applied Optics,* vol. 19, pp. 3545-3553, 1980.

[78] W. Jiang, D. Shealy and J. Martin, "Design and testing of a refractive reshaping system," *Proceeding of SPIE,* vol. 2000, pp. 64-75, 1993.

[79] W. Jiang, D. Shealy and K. Baker, "Optical design and testing of a holographic projection system," *Proceedings of SPIE,* vol. 2152, pp. 244-252, 1994.

[80] D. Shafer, "Gaussian to flat-top intensity distributing lens," *Optics & Laser Technology.*

[81] S. Jahan and M. Karim, "Refracting systems for Gaussian-to-uniform beam transformations," *Optics & Laser Technology,* vol. 21, pp. 27-30, 1989.

[82] M. Karim, A. Cherri, A. Awwal and A. Basit, "Refracting system for annular laser beam transformation," *Applied Optics,* vol. 26, no. 12, pp. 2446-2449, 1987.

[83] Y. Yamamota, "Anamorphic single lens". U.S. Patent 4915484, 1990.

[84] J. McDermit and T. Horton, "Reflective optics for obtaining prescribed

irradiative distributions from collimated sources," *Applied Optics,* vol. 13, pp. 1444-1450, 1974.

[85] S. Solimeno, B. Crosignani and P. DiPorto, "Guiding, Diffraction, and Confinement of Optical Radiation," *Academic Press,* p. 49, 1984.

[86] P. Mouroulis and J. Macdonald, Geometrical Optics and Optical Design, New York: Oxford University Press, 1997.

[87] D. Koch, "Simplified irradiance/illuminance calculations in optical systems," *Proceedings of SPIE,* vol. 1780, pp. 226-240, 1992.

[88] D. Burkhard and D. Shealy, "Simplified formula for the illuminance in an optical system," *Applied Optics,* vol. 20, pp. 897-909, 1981.

[89] D. Burkhard and D. Shealy, "A different approach to lighting and imaging: Formulas for flux density, exact lens and mirror equations," *Proceedings of SPIE,* vol. 692, pp. 248-272, 1986.

[90] D. Cornwell, "Non-projective transformations in optics," *Proceedings of SPIE,* vol. 294, pp. 62-72, 1981.

[91] J. Curtis, C. Schmitz and J. Spatz, "Symmetry dependence of holograms for optical trapping," *Optics letters,* vol. 30, pp. 2086-2088, 2005.

[92] D. Carberry, G. Whyte, J. Leach, J. Courtial, J. Jackson, D. Robert, M. Miles and M. Padgett, "Holographic assembly workstation for optical manipulation," *Journal of Optics A: Pure and Applied Optics,* vol. 10, p. 044009, 2008.

[93] S. Hasegawa, Y. Hayasaki and N. Nishida, "Holographic femtosecond laser processing with multiplexed phase Fresnel lenses," *Optics Letter,* vol. 31, pp. 1705-1707, 2006.

[94] H. Takahashi, S. Hasegawa and Y. Hayasaki, "Holographic femtosecond laser processing using optimal-rotation-angle method with compensation of spatial frequency response of liquid crystal spatial light modulator," *Applied Optics,* vol. 46, pp. 5917-5923, 2007.

[95] K. Chaen, H. Takahashi, S. Hasegawa and Y. Hayasaki, "Display method with compensation of the spatial frequency response of a liquid crystal spatial light modulator for holographic femtosecond laser processing," *Optics Communications,* vol. 280, pp. 165-172, 2007.

[96] O. Yavas and M. Takai, "Effect of substrate absorption on the efficiency of laser patterning of indium tin oxide thin films," *Journal of Applied Physics,* vol. 85, pp. 4207-4212, 1999.

[97] W. Woerdemann, C. Alpmann, M. Esseling and C. Denz, "Advanced optical trapping by complex beam shaping," *Laser Photonics Review,* vol. 7, pp. 839-854, 2013.

[98] C. Maurer, A. Jesacher, S. Bernet and M. Ritsch-Marte, "What spatial light modulators can do for optical microscopy," *Laser Photonics Review,* vol. 5, pp. 81-101, 2011.

[99] A. Jeascher, C. Maurer, A. Schwaighofer, S. Bernet and M. Ritsch-Marte, "Full phase and amplitude control of holographic optical tweezers with high efficiency," *Optics Express,* vol. 16, pp. 4479-4486, 2008.

[100] D. Bowman, T. Harte, V. Chardonnet, C. Groot, S. Denny, G. Goc, M. Aderson, P. Ireland, D. Cassettari and G. Bruce, "High-fidelity phase and amplitude control of phase-only computer generated holograms," *Optics Express,* vol. 25, no. 10, pp. 11692-11700, 2017.

[101] J. Shewchuk, An introduction to the conjugate gradient method without the agonizing pain, Carnegie Mellon University, 1994.

[102] Q. Zhan, "Cylindrical vector beams: from mathematical concepts to applications," *Advances in Optics and Photonics,* vol. 1, no. 1, pp. 1-57, 2009.

[103] A. Tovar, "Production and propagation of cylindrically polarized Laguerre–Gaussian laser beams," *Journal of the Optical Society of America A,* vol. 15, no. 10, pp. 2705-2711, 1998.

[104] Y. Jin, O. Allegre, W. Perrie, K. Abrams, J. Ouyang, E. Fearon, S. Edwardson and G. Dearden, "Dynamic modulation of spatially structured polarization fields for real-time control of ultrafast laser-material interactions," *Optics Express,* vol. 21, no. 21, pp. 25333-25343, 2013.

[105] M. Beresna, M. Gecevičius, P. Kazansky and T. Gertus, "Radially polarized optical vortex converter created by femtosecond laser nanostructuring of glass," *Apply Physics Letter,* vol. 98, no. 20, p. 201101, 2011.

[106] L. Novotny, M. Beversluis, K. Youngworth and T. Brown, "Longitudinal field modes probed by single molecules," *Physical Review Letters,* vol. 86, no. 23, pp. 5251-5254, 2001.

[107] Q. Zhan, "Trapping metallic Rayleigh particles with radial polarization," *Optics Express,* vol. 12, no. 15, pp. 3377-3382, 2004.

[108] C. Varin and M. Piché, "“Acceleration of ultra-relativistic electrons using high-intensity TM01 laser beams," *Applied Physics B,* vol. 74, no. S1, pp. s83-s88, 2002.

[109] K. Anoop, A. Rubano, R. Fittipaldi, X. Wang, D. Paparo, A. Vecchione, L. Marrucci, R. Bruzzese and S. Amoruso, "Femtosecond laser surface structuring of silicon using optical vortex beams generated by a q-plate," *Applied Physics Letters,* vol. 104, no. 24, p. 241604, 2014.

[110] F. Gori, "Polarization basis for vortex beams," *Journal of the Optical Society of*

America A, vol. 18, no. 7, pp. 1612-1617, 2001.

[111] "Nd:VAN regenerative laser amplifier, Manual of High-Q IC-355-800ps," *Photonics Solustions Laser,* 2007.

[112] "Holoeye LC-R 2500 spatial light modulator (SLM)," Official Webpage of Holoeye Company, [Online]. Available: https://holoeye.com/spatial-light-modulators/discontinued-devices/. [Accessed 20 12 2017].

[113] "A3200 Software-Based Machine Controller," AEROTECH, [Online]. Available: https://www.aerotech.com/product-catalog/motion-controller/a3200.aspx?search-auto-complete=true. [Accessed 1 6 2018].

[114] "AVS100/AVSI100 Series Mechanical-Bearing Screw-Driven Lift Stage," AEROTECH, [Online]. Available: https://www.aerotech.com/product-catalog/stages/lift-and-z-axis-stages/avs100avsi100-series.aspx. [Accessed 1 6 2018].

[115] "Goniometers," AEROTECH, [Online]. Available: https://www.aerotech.com/product-catalog/goniometer.aspx. [Accessed 1 6 2018].

[116] "Thorlabs Beam - Beam Analyzing software BC106-VIS BC106-UV Operation Manual," Thorlabs, 2011.

[117] "SP620U-USB-CCD-Kameras," OPHIR PHOTONICS beam profilers, [Online]. Available: http://www.ophiropt.com/de/laser-measurement-instruments/beam-profilers/products/camera-based-profilers/the-camera/SP620U. [Accessed 1 6 2018].

[118] P. Bizi-bandoki, S. Valette, E. Audouard and S. Benayoun, "Time dependency of the hydrophilicity and hydrophobicity of metallic alloys subjected to femtosecond laser irradiations," *Applied Surface Sciences,* vol. 273, no. 399-407, 2013.

[119] X. Yu, Y. Liao, F. He, B. Zeng, Y. Cheng, Z. Xu, K. Sugioka and K. Midorikawa, "Tuning etch selectivity of fused silica irradiated by femtosecond laser pulses by controlling polarization of the writing pulses," *Journal of Applied Physics,* vol. 109, pp. 053114-053116, 2011.

[120] J. Bonse, R. Koter, M. Hartelt, D. Spaltmann, S. Pentzien, S. Höhm, A. Rosenfeld and J. Krüger, "Femtosecond laser-induced periodic surface structures on steel and titanium alloy for tribological applications," *Applied Physics A,* vol. 117, pp. 103-110, 2014.

[121] R. Buividas, N. Fahim, J. Juodkazytė and S. Juodkazis, "Novel method to determine the actual surface area of a laser-nanotextured sensor," *Applied Physics A,* vol. 114, pp. 169-175, 2014.